ABGAIL PAULA PINHEIRO

LAGRANGIAN MODELING OF DROPLET EVAPORATION

UNIVERSIDADE FEDERAL DE UBERLÂNDIA
FACULDADE DE ENGENHARIA MECÂNICA
2018

ABGAIL PAULA PINHEIRO

LAGRANGIAN MODELING OF DROPLET EVAPORATION

Dissertação apresentada ao Programa de Pós-graduação em Engenharia Mecânica da Universidade Federal de Uberlândia, como parte dos requisitos para a obtenção do título de **MESTRE EM ENGENHARIA MECÂNICA**.

Área de concentração: Transferência de Calor e Mecânica dos Fluidos.

Orientador: Prof. Dr. Aristeu da Silveira Neto
Coorientador: Prof. Dr. João Marcelo Vedovoto

Uberlândia - MG
2018

Dados Internacionais de Catalogação na Publicação (CIP)
Sistema de Bibliotecas da UFU, MG, Brasil.

P654L 2018

Pinheiro, Abgail Paula, 1992-
Lagrangian modeling of droplet evaporation [recurso eletrônico] / Abgail Paula Pinheiro. - 2018.

Orientador: Aristeu da Silveira Neto.
Coorientador: João Marcelo Vedovoto.
Dissertação (mestrado) - Universidade Federal de Uberlândia, Programa de Pós-Graduação em Engenharia Mecânica.
Modo de acesso: Internet.
Disponível em: http://dx.doi.org/10.14393/ufu.di.2018.1180
Inclui bibliografia.
Inclui ilustrações.

1. Engenharia mecânica. 2. Evaporação - Modelos matemáticos. I. Silveira Neto, Aristeu da, 1955- (Orient.). II. Vedovoto, João Marcelo, 1981- (Coorient.). III. Universidade Federal de Uberlândia. Programa de Pós-Graduação em Engenharia Mecânica. IV. Título.

CDU: 621

Maria Salete de Freitas Pinheiro - CRB6/1262

UNIVERSIDADE FEDERAL DE UBERLÂNDIA
Coordenação do Programa de Pós-Graduação em Engenharia Mecânica
Av. João Naves de Ávila, nº 2121, Bloco 1M, Sala 212 - Bairro Santa Mônica, Uberlândia-MG, CEP 38400-902
Telefone: (34) 3239-4282 - www.posgrad.mecanica.ufu.br - secposmec@mecanica.ufu.br

TERMO

ALUNA: Abgail Paula Pinheiro **MATRÍCULA:** 11622EMC001

ÁREA DE CONCENTRAÇÃO: Transferência de Calor e Mecânica dos Fluidos

LINHA DE PESQUISA: Dinâmica dos Fluidos e Transferência de Calor

PÓS-GRADUAÇÃO EM ENGENHARIA MECÂNICA: NÍVEL MESTRADO

TÍTULO DA DISSERTAÇÃO: *"Lagrangian Modeling of Droplet Evaporation"*

ORIENTADOR: Prof. Dr. Aristeu da Silveira Neto **CO-ORIENTADOR:** Prof. Dr. João Marcelo Vedovoto

A Dissertação foi **APROVADA** em reunião pública, realizada no Auditório do Laboratório de Mecânica dos Fluidos - Bloco 5P, Campus Santa Mônica, em 10 de agosto de 2018, às 08:00 horas, com a seguinte Banca Examinadora:

Prof. Dr. Aristeu da Silveira Neto (orientador) - UFU

Prof. Dr. João Marcelo Vedovoto (coorientador) - UFU

Prof. Dr. Francisco José de Souza - UFU

Prof. Dr. João Luiz Filgueiras de Azevedo - IAE

Dr. Ricardo Serfaty - Petrobras

Uberlândia, 10 de agosto de 2018

Documento assinado eletronicamente por **Aristeu da Silveira Neto**, **Professor(a) do Magistério Superior**, em 10/08/2018, às 10:36, conforme horário oficial de Brasília, com fundamento no art. 6º, § 1º, do Decreto nº 8.539, de 8 de outubro de 2015.

Documento assinado eletronicamente por **ricardo serfaty**, **Usuário Externo**, em 10/08/2018, às 10:39, conforme horário oficial de Brasília, com fundamento no art. 6º, § 1º, do Decreto nº 8.539, de 8 de outubro de 2015.

Documento assinado eletronicamente por **Francisco José de Souza**, **Professor(a) do Magistério Superior**, em 10/08/2018, às 10:39, conforme horário oficial de Brasília, com fundamento no art. 6º, § 1º, do Decreto nº 8.539, de 8 de outubro de 2015.

Documento assinado eletronicamente por **João Marcelo Vedovoto**, **Professor(a) do Magistério Superior**, em 10/08/2018, às 10:42, conforme horário oficial de Brasília, com fundamento no art. 6º, § 1º, do Decreto nº 8.539, de 8 de outubro de 2015.

Documento assinado eletronicamente por **João Luiz Filgueiras de Azevedo**, **Usuário Externo**, em 10/08/2018, às 10:46, conforme horário oficial de Brasília, com fundamento no art. 6º, § 1º, do Decreto nº 8.539, de 8 de outubro de 2015.

A autenticidade deste documento pode ser conferida no site https://www.sei.ufu.br/sei/controlador_externo.php?acao=documento_conferir&id_orgao_acesso_externo=0, informando o código verificador **0635193** e o código CRC **38073E4E**.

"We do not receive wisdom, we must discover it for ourselves, after a journey through the wilderness which no one else can make for us, which no one can spare us."

Marcel Proust

To my family, for their love and support.

ACKNOWLEDGEMENTS

I would like to express my sincerest gratitute to Prof. Dr. João Marcelo Vedovoto and Prof. Dr. Aristeu da Silveira Neto for their constant support during these two years. Under their guidance, with kindness and examples, they both taught me to be a better researcher. Prof. João Marcelo, thank you for the inumerous encouragement words during tough moments and for the inspiring discussions about droplet evaporation. Prof. Aristeu, thank you for the wise and phylosophical talks about turbulence and life itself. I could not be happier with the opportunity you have given me.

I would like to acknowledge the financial and technical support from Petróleo Brasileiro S.A. (Petrobras), National Counsel of Technological and Scientific Development (CNPq), Minas Gerais State Agency for Research and Development (FAPEMIG) and Coordination for the Improvement of Higher Education Personnel (CAPES).

I am grateful to all friends and colleagues from MFLab for the many moments of fun and learning. I specially thank Hélio, Bernardo, Alessandra, Marcelo, Lucas, Alex, Ricardo, Gabriel, Jéssica, Millena and Pedro for the jokes, hugs and helps. I would also like to thank Luismar, Ana Luisa and Bruno for the technical support.

My beautiful family, Francisco, Joseilda, André, Ablail, Ana Luiza, Argélia e João Vitor, thank you for always being by my side, no matter the distance, giving me all the support and love I need to continue. You are my best!

My dearest Danilo, I am truthfully thankful for your everyday patience and love. Thank you for always making me laugh.

Letícia, Simone, Felipe, Marcela, Carol, Teresa Cristina, and Karina, my beloved friends, thank you for the care, affection and constant presence during this challenging moment.

PINHEIRO, A. P., **Lagrangian modeling of droplet evaporation.** 2018. 101 p. Master Dissertation, Federal University of Uberlândia, Uberlândia.

ABSTRACT

Evaporation of liquid droplets in high temperature gas environment is of great importance in many engineering applications. Accurate droplet evaporation predictions are crucial in modeling spray combustion, since it is considered a rate limiting process. For this reason, the present dissertation aims are, first, to implement and validate Lagrangian droplet evaporation models that are usually used in spray calculations, including equilibrium and non-equilibrium formulations, and, second, to use these models to pursue a deeper insight on the physical phenomena that may be involved in droplet evaporation processes. In order to validate and assess these theoretical model predictions, an in-house code was developed and diameter evolution results from the numerical simulations are compared to experimental data. First, the model performance is evaluated for water in a case of low evaporation rate and, then, it is evaluated for n-heptane in moderate and high evaporation rates using recent experimental data acquired with a new technique. The Abramzon-Sirignano model is the only one which does not overestimate the evaporation rate for any ambient condition tested, when compared with experimental rate. From the results, it is also revealed that, when a correction factor for energy transfer reduction due to evaporation is incorporated in the classical evaporation model, the predictions from this model and the non-equilibrium one cannot be differentiated, even if the initial droplet diameter is small. Furthermore, the incorporation of natural and forced convection effects on the droplet evaporation rate, by using an empirical correlation, is investigated, showing that including the Grashof number into the Ranz-Marshall correlation actually overestimates the evaporation rate for atmospheric pressure. Finally, the effects of ambient conditions on ethanol evaporation are investigated. Under ambient temperatures higher than the threshold temperature, the evaporation rate is enhanced with the increase of ambient pressure, contrary to what happens for cases when the ambient temperature is lower than the threshold temperature.

Keywords: Droplet evaporation, Spray, Numerical simulation, Lagrangian approach.

PINHEIRO, A. P., **Modelagem lagrangiana de evaporação de gotas.** 2018. 101 f. Dissertação de Mestrado, Universidade Federal de Uberlândia, Uberlândia.

RESUMO

A evaporação de gotas líquidas em ambientes gasosos com alta temperatura é de grande relevância em muitas aplicações de engenharia. Previsões precisas da evaporação de gotas são cruciais na modelagem de sprays reativos, uma vez que este é considerado um processo limitante. Portanto, os objetivos da presente dissertação são, primeiro, implementar e validar modelos lagrangianos de evaporação de gotas que são geralmente utilizados em estudos de spray, incluindo as formulações de equilíbrio e não equilíbrio, e, segundo, usar esses modelos para buscar uma visão mais profunda dos fenômenos físicos que podem estar envolvidos no processo de evaporação de gotas. Para validar e avaliar as previsões destes modelos teóricos, foi desenvolvido um código e a evolução do diâmetro da gota obtida por simulação numérica é comparada com dados experimentais. Primeiro, o desempenho dos modelos é avaliado para água em um caso de baixa taxa de evaporação e, em seguida, para n-heptano com taxa de evaporação moderada e alta usando dados experimentais obtidos recentemente por meio de uma nova técnica. O modelo de Abramzon-Sirignano é o único que não superestima a taxa de evaporação para quaisquer condições ambiente testadas, quando comparada com a taxa experimental. A partir dos resultados, também é revelado que, quando um fator de correção para a redução da transferência de energia devido à evaporação é incorporado ao modelo clássico de evaporação, as previsões deste modelo e do modelo de não equilíbrio não podem ser diferenciadas, mesmo quando o diâmetro inicial da gota é pequeno. Além disso, a incorporação de efeitos de convecção natural e forçada na taxa de evaporação, usando uma correlação empírica, é investigada, mostrando que a inclusão do número de Grashof na correlação de Ranz-Marshall na verdade superestima a taxa de evaporação para pressão atmosférica. Finalmente, os efeitos das condições ambientes na evaporação de etanol são investigados. Sob temperaturas ambientes superiores à temperatura limite, a taxa de evaporação aumenta com o aumento da pressão ambiente, contrariamente ao que acontece nos casos em que a temperatura ambiente é menor que a temperatura limite.

Palavras-chave: Evaporação de gotas, Spray, Simulação numérica, Abordagem lagrangiana.

List of Figures

1.1 Evaporating droplet with relative gas-droplet motion and internal circulation (SIRIGNANO, 1983). 5

1.2 Hill's spherical vortex sketch, in which the vortex lines are complete circles at three different times and the kidney-shaped lines are streamlines (PANTON, 2013). . . . 6

1.3 Two-phase flow DNS classification into three different approaches with examples of methods for each approach. 6

1.4 Schematic illustration of ocean spray (a) formation and (b) evaporation (VERON, 2015). 8

1.5 Simulation of a gas turbine combustor in which the fuel droplets are shown in green (PITSCH, 2006). 8

1.6 Droplet suspending techniques (CHAUVEAU *et al.*, 2008). 9

1.7 Global fuel ethanol production by country in 2017 in million liters with share of global production (RFA - Renewable Fuels Association, 2017). 11

2.1 Schematic representation of droplet temperature evolution during its evaporation in absence of radiation. 16

2.2 Schematic representation of squared droplet diameter evolution during the evaporation of a single-component droplet, showing the linear behavior after the heat-up period. 17

2.3 Schematic representation of an evaporating droplet surrounded by gas with vapor mass fraction and temperature distributions along the radial direction. 19

2.4 Schematic representation of thermal energy and mass transfers in the evaporation of a single droplet. 20

4.1 Illustration of the time lines for a Eulerian-Lagrangian simulation with $\Delta t_{eul} > \Delta t_{lag}$. 33
4.2 Schematic representation of the barycentric interpolation, in which the distance between droplet and each control volume node is expressed by D. 36

5.1 General structure of the Lagrangian solver. 40
5.2 General structure of the Lagrangian evaporation function. 41
5.3 General structure of the Lagrangian map where **c** and **d** stand for cell and droplet, respectively. (a) Bidimensional block-structured mesh with each ID, where the black points represent the visible cells; (b) Droplets locations in the domain; (c) Multi-level hash table; and (d) Particles hash table. 42
5.4 Domain partition into 8 subdomains, where each subdomain is directed to a different processor. 44

6.1 Droplet evaporation rate temporal evolution. 48
6.2 Non-dimensional droplet diameter temporal evolution. 49
6.3 Droplet temperature temporal evolution. 49
6.4 Temporal variation of normalized squared droplet diameter for water. 51
6.5 Temporal variation of droplet temperature for water. 52
6.6 Variations of normalized squared droplet diameter with the time divided by squared initial droplet diameter for n-heptane. 53
6.7 Variations of droplet temperature with the time divided by squared initial droplet diameter for n-heptane. 54
6.8 Comparison of the area evaporation rate, according to the ambient temperature, for various models and experimental measurements for n-heptane. 55
6.9 Temporal evolution of some evaporation parameters for equilibrium and non-equilibrium conditions with T_g = 748 K and p_g = 0.1 MPa for n-heptane. 57
6.10 Temporal evolution of (a) the non-equilibrium contribution and (b) the ration between equilibrium and non-equilibrium vapor molar fraction for various initial droplet diameters with T_g = 748 K and p_g = 0.1 MPa for n-heptane. 58
6.11 Temporal evolution of the surface vapor mass fraction for various initial droplet diameters with T_g = 748 K and p_g = 0.1 MPa for n-heptane. 59

6.12 Variations of normalized squared droplet diameter with the time divided by squared initial droplet diameter, with and without taking natural convection effects into account for n-heptane. 61

6.13 Temporal evolutions of droplet Grashof number for the ASM* predictions presented in Fig. 6.12 for n-heptane. 62

6.14 Comparison of the area evaporation rate, according to the ambient temperature, with and without taking natural convection effects into account for n-heptane. . 62

6.15 Temporal variation of normalized squared droplet diameter for n-decane. 63

6.16 Temporal variation of droplet temperature for n-decane. 64

6.17 Variations of normalized squared droplet diameter with the time divided by squared initial droplet diameter. 66

6.18 Experimental, numerical and theoretical average area evaporation rates at various ambient temperatures. 67

6.19 Variations of normalized squared droplet diameter with the time divided by squared initial droplet diameter at low temperature and various ambient pressures. 68

6.20 Variations of normalized squared droplet diameter with the time divided by squared initial droplet diameter at high temperature and various ambient pressures. . . . 69

6.21 Variations of droplet temperature with the time divided by squared initial droplet diameter at low temperature and various ambient pressures. 70

6.22 Variations of droplet temperature with the time divided by squared initial droplet diameter at high temperature and various ambient pressures. 71

6.23 Average area evaporation rates at various ambient pressures. 72

6.24 Droplet final equilibrium temperature at various ambient pressures. 72

6.25 Schematic representation of the computational domain for the evaporation of a single droplet. 73

6.26 Temporal variation of (a) normalized squared droplet diameter and (b) temperature for CEM comparing Python and MFSim predictions. 73

6.27 Temporal variation of (a) normalized squared droplet diameter and (b) temperature for ASM comparing Python and MFSim predictions. 74

6.28 Temporal variation of (a) normalized squared droplet diameter and (b) temperature for NEQ comparing Python and MFSim predictions. 74
6.29 Droplet evaporation for CEM simulation, in which it is colored by temperature and its diameter reduces. 76
6.30 Computational domain and initial droplet diameter distribution. 77
6.31 Vortex flow with droplet evaporation. 78
6.32 Serial *versus* parallel computation, where the vertical lines represent the droplet passing between processors. 79

List of Tables

6.1 B-values for n-heptane numerical simulations 53

6.2 Simulation conditions for evaporation models verification in MFSim 71

List of Symbols

Abbreviations

ASM	Abramzon-Sirignano Model
ASM*	Abramzon-Sirignano Model with natural convection effects
CEM	Classical Evaporation Model
CEM*	Classical Evaporation Model without the evaporation correction factor
CFD	Computational Fluid Dynamics
CFL	Courant Friedrichs Lewy
DNS	Direct Numerical Simulation
ECM	Effective Conductivity Model
FTM	Front Tracking Method
ICM	Infinite Conductivity Model
ID	Identifier
LES	Large Eddy Simulation
MPI	Message Passing Interface
NEQ	Non-Equilibrium Model
URANS	Unsteady Reynolds-Averaged Navier-Stokes
VOF	Volume Of Fluid

Non-dimensional numbers

B_M	Spalding mass transfer number
B_T	Spalding thermal energy transfer number
Le	Lewis number
Nu	Nusselt number
Pr	Prandtl number
Sc	Schmidt number
Sh	Sherwood number
Re_d	Droplet Reynolds number

Subscripts

atm	Atmospheric
d	Droplet
eq	Equilibrium
ev	Evaporation
g	Ambient gas properties
h	Heat-up
l	Liquid properties
m	Gas-vapor film properties
o	Initial
s	Properties at the droplet surface
sat	Saturation

v	Vapor properties

Superscripts

eq	Equilibrium
neq	Non-equilibrium

Greek letters

α_e	Molecular accommodation coefficient
α_w	Weighting parameter for gas-vapor mixture properties evaluation
β	Non-dimensional evaporation parameter
Δx	Grid size in the x direction
Δy	Grid size in the y direction
Δz	Grid size in the z direction
δ_M	Mass film thickness
δ_T	Thermal film thickness
μ	Dynamic viscosity
ϕ_d	General droplet scalar quantity
ψ	General Eulerian property
ρ	Density
τ_d	Droplet relaxation time
χ_v	Vapor molar fraction
Δl	Control volume characteristic length
Δm_d	Droplet mass variation

Δt_{eul}	Eulerian time step
Δt_{lag}	Lagrangian time step

Latin letters

$\dot{m}_d$	Droplet evaporation rate
c_p	Specific heat capacity
D_d	Droplet diameter
F_M	Correction factor for diffusional film thickness
F_T	Correction factor for thermal film thickness
G	Correction factor for energy transfer reduction due to evaporation
K	Area reduction rate
k	Thermal conductivity
L_K	Knudsen layer thickness
L_v	Specific latent heat of evaporation
m_d	Droplet mass
p	Pressure
Q_d	Energy effectively received at the droplet surface
Q_L	Latent heat of evaporation
Q_S	Sensible heat
Q_{g-d}	Total energy transferred from the gas to the droplet
Q_{g-v}	Energy carried away from droplet by diffusing vapor
R_d	Droplet radius

R_u	Universal gas constant
T_b	Boiling temperature
T_d	Droplet temperature
T_{wb}	Wet-bulb temperature
W	Molecular weight
Y_v	Vapor mass fraction
$\mathbf{g}$	Gravitational acceleration
C_D	Drag coefficient
D_v	Vapor diffusion coefficient
$\mathbf{u}_d$	Droplet velocity
$\mathbf{u}_g$	Gas velocity
$\mathbf{x}_d$	Droplet position

Contents

LIST OF FIGURES ix

LIST OF TABLES x

LIST OF SYMBOLS xi

1 INTRODUCTION 1

1.1 Background theory . . . 2

1.1.1 Evaporating droplets . . . 2

1.1.2 Computational simulations . . . 3

1.2 Motivation . . . 7

1.2.1 Applications . . . 7

1.2.2 Validation database . . . 8

1.2.3 Alternative fuels . . . 10

1.3 Objectives . . . 11

1.4 Methodology . . . 12

1.5 Dissertation outline . . . 13

2 PHYSICAL MODEL AND SIMPLIFYING ASSUMPTIONS 15

3 MATHEMATICAL MODEL 21

3.1 Displacement model . . . 21

3.2 Evaporation models . . . 23

3.2.1 Classical evaporation model . . . 24

3.2.2 Abramzon-Sirignano model . . . 28

3.2.3 Non-equilibrium model . . . 29
3.2.4 Gas-vapor mixture properties . . . 30

4 NUMERICAL MODEL 32

4.1 Time step calculation . . . 32
4.2 Time integration . . . 34
4.3 Vanishing droplets . . . 35
4.4 Interpolation method . . . 36

5 COMPUTATIONAL MODEL 38

5.1 Lagrangian solver structure . . . 39
5.2 Data structure . . . 39
5.2.1 Lagrangian map . . . 42
5.2.2 Lagrangian variables . . . 42
5.3 Search algorithm . . . 43
5.4 Parallelization . . . 44
5.5 Cantera . . . 45
5.6 Fortran/C/C++ languages linking . . . 45

6 RESULTS AND DISCUSSION 47

6.1 Abramzon-Sirignano model verification . . . 48
6.2 Evaporation models validation . . . 50
6.2.1 Water droplet with low evaporation rate . . . 50
6.2.2 N-heptane droplet with moderate to high evaporation rate . . . 51
6.3 NEQ: Langmuir-Knudsen law *versus* Evaporation correction factor . . . 56
6.4 Natural convection effects . . . 59
6.5 Forced convection effects . . . 63
6.6 Ambient conditions effects on ethanol evaporation . . . 64
6.6.1 Validation . . . 65
6.6.2 Effects of ambient pressure and temperature . . . 67
6.7 MFSim simulations . . . 70

6.7.1 Python *versus* MFSim: implementation verification 70
6.7.2 Vortex flow: parallelization verification 72

7 CONCLUSIONS AND RECOMMENDATIONS 80

7.1 Model development 80
7.2 Validation and investigations 81
7.3 Main conclusions 82
7.4 Recommendations 83

BIBLIOGRAPHY 85

APPENDIX 96

CHAPTER I

INTRODUCTION

Droplet evaporation is a complex two-phase flow phenomenon, whose modeling should take into account the effects of transient liquid heating, gas phase convection and variable physical properties. As a multidisciplinary issue, it can involve energy and mass transport, fluid dynamics, and chemical kinetics. It is of primary importance in many natural physical processes and in a host of industrial and man-related activities. This phenomenon can be found in several engineering application fields such as, for instance, automotive and aeronautic engineering, fire suppression, painting and medical aerosol.

Since the early work of Maxwell on this subject more than 140 years ago (MAXWELL, 2011), a relatively vast literature has become available. From these works, many valuable findings have been reported, which helped us to increase our awareness of the key processes involved and how devices operating conditions may impact these processes. However, this problem still remains one of the fundamental aspects of spray investigation, to predict and improve those systems. Thus, this area indeed requires more scientific research looking for in depth physical insight and mathematical, numerical and computational models able to balance results accuracy and computational efficiency.

Throughout this chapter, the purpose of the present research is elucidated and its relevance to technical and academic demands is explained.

1.1 Background theory

The background theory required to understand the role of evaporating droplets in spray studies and the Computational Fluid Dynamics (CFD) techniques employed to simulate them are presented in this section.

1.1.1 Evaporating droplets

Spray evaporation has been widely studied throughout the last decades, theoretically (FAETH, 1983; SIRIGNANO, 1983), experimentally (SOMMERFELD; QIU, 1998; CHEN; STÅRNER; MASRI, 2006; LI; NISHIDA; HIROYASU, 2011), and numerically (SADIKI *et al.*, 2005; JONES; LYRA; MARQUIS, 2010; DE; LAKSHMISHA; BILGER, 2011; AZAMI; SAVILL, 2016; ABDEL-SAMIE; THÉVENIN, 2017). However, considering the complexity of such theme, an isolated droplet evaporating in gas medium, which represents an ideal model of the physical phenomena involved in the diluted regions of a spray, seems to be a first step towards better understanding the evaporation dynamics. Even though the case of a single isolated droplet might seem just as an idealization, in most technical applications where the spray can be considered dilute, this assumption is actually reasonable (JENNY; ROEKAERTS; BEISHUIZEN, 2012). Dense dispersed two-phase flows are not in the scope of the present work, since the isolated droplet assumption is no longer valid.

Evaporating sprays can be classified as dispersed two-phase flow, containing a liquid as the dispersed phase in the form of droplets and a gas as the continuous carrier phase. The volume fraction of the dispersed phase, α_d, is the volume occupied by the droplets in a unit volume of the continuous phase, V. Hence, this property is given by:

$$\alpha_d = \frac{\sum_1^{N_i} V_{di}}{V}, \tag{1.1}$$

where N_i is the number of all droplets in the control volume, having each droplet volume as $V_{di} = \pi {D_{di}}^3/6$. According to Sommerfeld (2017), a dispersed two-phase flow may be considered in a dilute regime when the volume fraction is lower than $5\text{x}10^{-4}$ or the mean inter-droplet spacing is larger than approximately ten droplet diameters.

As defined by Ashgriz (2011), evaporation is a process of phase transition in which molecules in a liquid overcome the intermolecular attraction forces and escape into the surrounding gaseous medium. When energy is supplied to a liquid, its temperature and, hence, the kinetic energy of the liquid molecules, are augmented, resulting in an increase of the evaporation rate. When the ambient pressure diminishes, the chances of the liquid molecules near the surface to overcome their intermolecular attraction potential increases, also resulting in an increase of the evaporation rate.

Therefore, droplet evaporation process basically consists in two main stages. First, vapor molecules detach from the droplet surface into the surrounding gas in the immediate vicinity of the droplet. Then, these vapor molecules diffuse away from the droplet surface into the ambient gas due to the concentration gradient.

Sazhin (2006) states that, as the mathematical modeling of the first stage is extremely complex, in most practical applications the first stage is neglected and the assumption that vapor in the vicinity of the droplet surface is always saturated is adopted. Thus, the evaporation rate is actually equals to the vapor diffusion rate. The evaporation models that follow this vapor saturation assumption are called dynamic models.

Sazhin (2006) also presents evaporation models that consider the vapor molecules detachment, such as the kinetic models, which are based on Boltzmann transport equation, and the molecular dynamics models, that model the dynamics of each individual molecule.

Even though the description of the evaporation process is based on a molecular viewpoint, the present work is based on the continuum hypothesis by using the fundamental balance equations for mass, energy and linear momentum for liquid and gas phases, together with the appropriate interfacial conditions, i.e., droplet surface boundary conditions, initial conditions, and relevant thermodynamic relations, as presented in Chapter 3. As a consequence, only dynamical models are studied and implemented in the present research, since for practical applications computational cost and accuracy should be balanced. The simplifying assumptions made for the derivation of the dynamical evaporation models will be discussed in Chapter 2.

1.1.2 Computational simulations

In the past decades, CFD has become a very powerful tool, both in academic research and industrial applications, and it has been increasingly employed to analyze processes and to support engineering decisions. However, application of CFD in two-phase flow simulations is pretty young, probably having started only around 40 years ago, due to the complexity of the physical phenomena involved in them (SOMMERFELD, 2017). Evaporating sprays, which are an example of two-phase flows, may involve several phenomena, such as: jet breakup and atomization; droplet collision and coalescence by droplet-wall and droplet-droplet interactions; mass, energy and linear momentum transfers by droplet-gas interaction (SCHWARZKOPF *et al.*, 2011).

Even though there exist various challenges to model those problems, computational simulations are often preferred over material experiments because of the following reasons: (i) they can overcome some of the difficulties related to control external perturbations in order to maintain the conditions assumed by theoretical models throughout the whole test; (ii) since parameter imposition is easier in computational simulations, they can be used to study a much wider range of conditions, which allows to study the influence of individual operating parameters on industrial device performances; (iii) the submillimeter scales associated with the evaporating-spray problem have made detailed experimental measurements very difficult in terms of catching the fluid-dynamical characteristics of this flow; and (iv) computational simulations may be carried out faster due to a shorter lead-time, and with less expenses, depending on the studied problem (LIU, 1999).

A Direct Numerical Simulation (DNS) of single-phase flows may be defined as solving the Navier-Stokes equations, coupled with the continuity equation, for all the turbulent scales in the flow field. For two-phase flows, on the other hand, it implies on the resolution of the gas phase around each droplet and the whole field of droplets. In this context, three distinct approaches can be adopted in order to perform a two-phase flow DNS: Eulerian-Eulerian (E-E), Eulerian-Lagrangian (E-L) with resolved droplet and Eulerian-Lagrangian with point droplet approximation (JENNY; ROEKAERTS; BEISHUIZEN, 2012).

The Eulerian-Eulerian approach is based on interface capturing methods to describe the two fluid phases by a marker function for which a transport equation is solved. This marker function

may be the volume fraction, which represents the amount of each phase in each computational cell of the domain. The interface position is inferred by the value of the marker function. The most used interface capturing methods are the volume of fluid (VOF) and the level set methods. The VOF method, for instance, treats the multiphase flow using the "one-fluid" approach, with fully Eulerian formulation, only using a marker function to represent the existence of multiple phases. Some examples of DNS studies using the Eulerian-Eulerian approach are Schlottke and Weigand (2008), Lee, Riaz and Aute (2017) and Deising, Bothe and Marschall (2018).

The Eulerian-Lagrangian approach with resolved droplet applies interface tracking methods, such as front tracking methods (FTM). These methods represent the interface between phases with a set of Lagrangian marker points and this interface is advected in a Lagrangian fashion, while the flow equations for both phases are solved on a Eulerian grid. The extra forces, calculated on the marker points, are added to the right hand side of the flow equations in order to mimic the boundary conditions at the interface. The fluid dynamic forces and gravitational forces on the droplet are used to calculate its motion and rotation. It is crucial that no approximation of these forces and torques be made. The boundary conditions corresponding to each and every droplet surface should also be included. Thus, good resolution of the velocity, pressure, temperature and concentration gradients in the droplet vicinity is required to precisely determine the coupling terms, which express the linear momentum, thermal energy and mass transfer rates between phases. Some examples of DNS studies using the Eulerian-Lagrangian approach with resolved droplet are Irfan and Muradoglu (2017) and Fang *et al.* (2018).

The Eulerian-Lagrangian approach with point droplet approximation also applies continuum equations for the gaseous phase, but droplet evaporation rate, temperature change and acceleration are actually modeled. The point droplet approximation approach may be a good choice when droplet sizes are below the Kolmogorov length scale, since the droplets will not interfere with the resolved spectrum. Some examples of DNS studies using the Eulerian-Lagrangian approach with point droplet approximation are Xia and Luo (2009), Wang, Luo and Fan (2014) and Abdelsamie and Thévenin (2017). Sirignano (2010) presents some evaporation models that differ from each other in the treatment of the liquid phase heating, which is usually the rate-controlling phenomenon in droplet evaporation, particularly in high-temperature gas environment. The differences between these models are mostly whether the liquid thermal conductivity and the

internal liquid circulation driven by surface-shear forces, as displayed in Fig. 1.1, are considered or not.

Figure 1.1: Evaporating droplet with relative gas-droplet motion and internal circulation (SIRIGNANO, 1983).

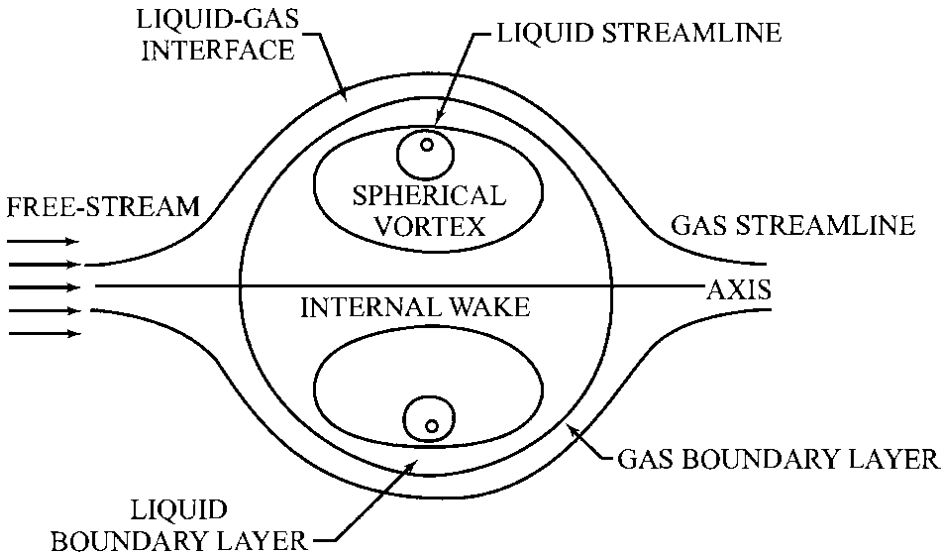

The infinite-liquid-conductivity model (ICM), with uniform but time-varying droplet temperature, assumes that the thermal conductivity of the liquid phase is infinitely large and that there is no temperature gradient inside the droplets. The effective conductivity model (ECM) takes into account both finite liquid thermal conductivity and the re-circulation inside droplets via the introduction of a correction factor to the liquid thermal conductivity, that is determined as a function of the liquid phase Péclet dimensionless number and varies from about 1 to 2.72 (ABRAMZON; SIRIGNANO, 1989). Moreover, there are vortex models for droplet heating, which describe the re-circulation inside droplets in terms of vortex dynamics to represent the physical situation of advective heating. The well-known Hill's spherical vortex, which is illustrated in Fig. 1.2, is usually used as a vortex model (HILL, 1894; BATCHELOR, 2000). In Figure 1.3, a chart summarizing all the possible approaches for computing a two-phase flow DNS, as described above, is displayed.

Considering that, in real-world problems, evaporating droplets are typically of the order of a few tens of micrometers to a few hundreds of micrometers in diameter, very fine computational grids are required to properly capture the whole detailed physics of these problems. Moreover, resolution of internal droplet gradients can imply resolution on a submicrometer scale, which can differ, by several orders of magnitude, from the Kolmogorov length scale, resulting in subgrid

Figure 1.2: Hill's spherical vortex sketch, in which the vortex lines are complete circles at three different times and the kidney-shaped lines are streamlines (PANTON, 2013).

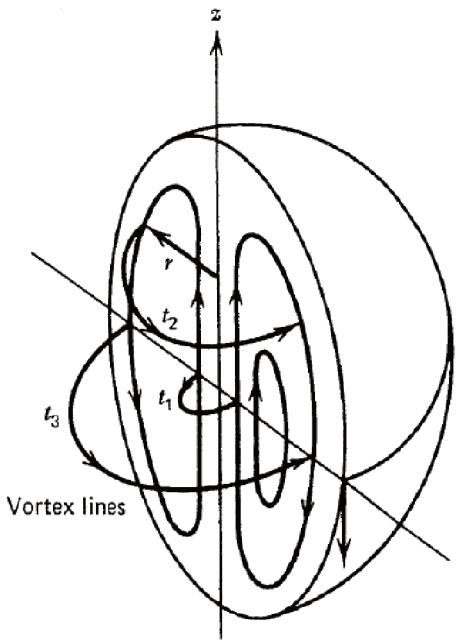

Figure 1.3: Two-phase flow DNS classification into three different approaches with examples of methods for each approach.

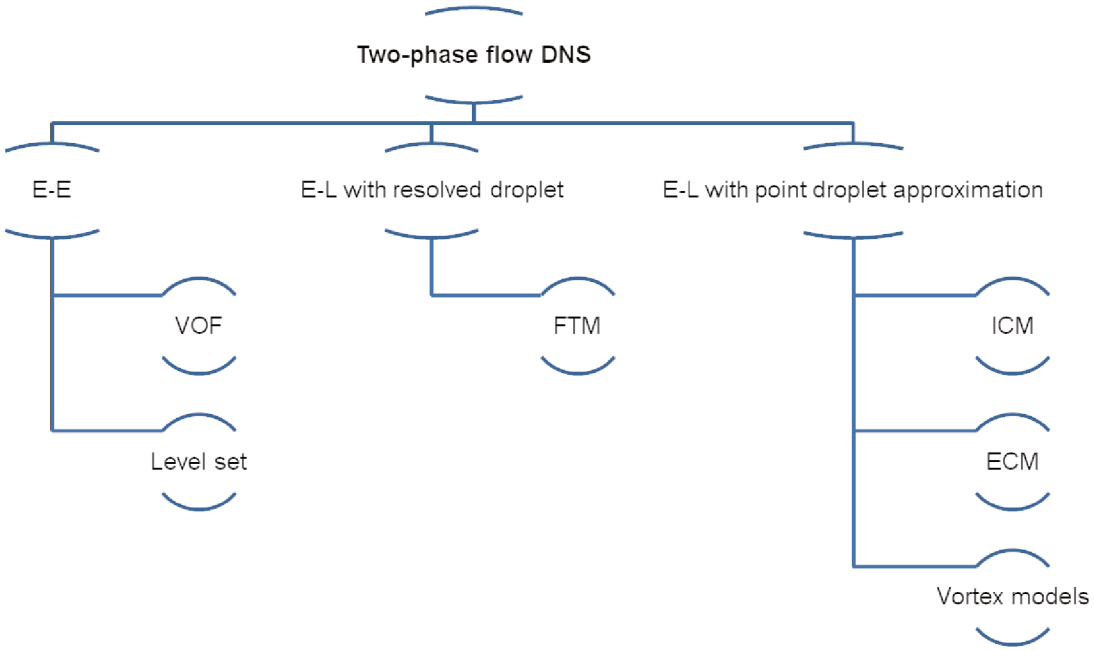

modeling problems.

Therefore, there are only few DNS studies with droplet internal flow detailed resolved because of the huge computational cost related, both in time and memory requirements, even without accounting for evaporation (JENNY; ROEKAERTS; BEISHUIZEN, 2012). For evaporat-

ing problems, species and thermal energy balance equations would also have to be contemplated, together with the continuity and Navier-Stokes equations. Consequently, DNS of two-phase flows using the Eulerian-Eulerian approach is limited to canonical test cases in academic research to be available as references and to gain physical insight. Meanwhile, DNS studies applying the Eulerian-Lagrangian approach with resolved droplets accounting for a large number of droplets is also not within current computational feasibility.

Several Lagrangian models for describing the dispersed phase evolution exist, for droplet dynamics and evaporation itself. These models are usually coupled with Large Eddy Simulation (LES) or Unsteady Reynolds-Averaged Navier-Stokes (URANS) methodologies for the gaseous continuous phase by means of sources terms. The focus of the present dissertation is the Lagrangian evaporation models, more specifically infinite-liquid-conductivity models, presenting their mathematical formulation in Chapter 3 and evaluating their predictions in Chapter 6.

1.2 Motivation

This section is dedicated to present the motivation that justifies the dissertation theme relevance. First, the main applications in which droplet evaporation can be found are illustrated. Second, the need of validating theoretical models with recent experimental data is explained. Third, the concern over greenhouse-gas emissions and the search for renewable fuels as an alternative to the petroleum sources are addressed.

1.2.1 Applications

Liquid droplet evaporation process can be observed in both nature and technological applications. In the environment, for example, such phenomenon occurs in ocean sprays (see Fig. 1.4) and rainfalls. In industry, it is mainly noticed in energy systems, such as furnaces, chemical reactors, gas turbines, internal combustion engines, among others (LEFEBVRE; MCDONELL, 2017). More specifically, evaporation of liquid droplets in high temperature gas environment plays an important role in technical applications involving combustion of liquid fuels. Due to improper handling, most of these devices are not operated under optimal conditions. Therefore, understanding the fundamental mechanisms that govern the dynamics of droplet evaporation

could improve industrial processes.

Figure 1.4: Schematic illustration of ocean spray (a) formation and (b) evaporation (VERON, 2015).

(a)

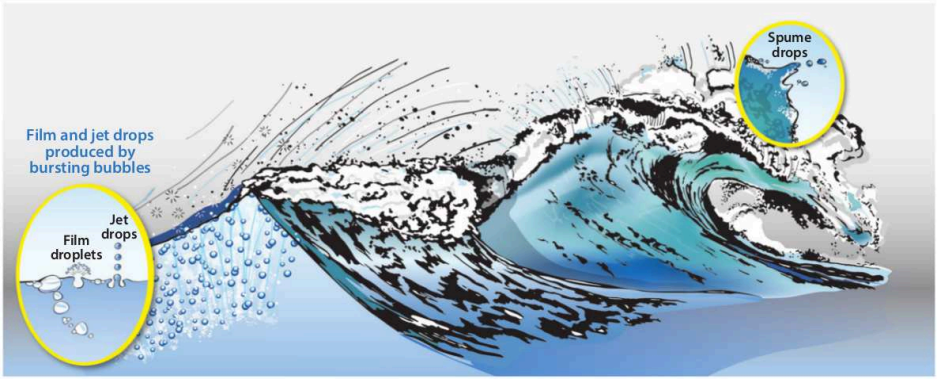

(b)

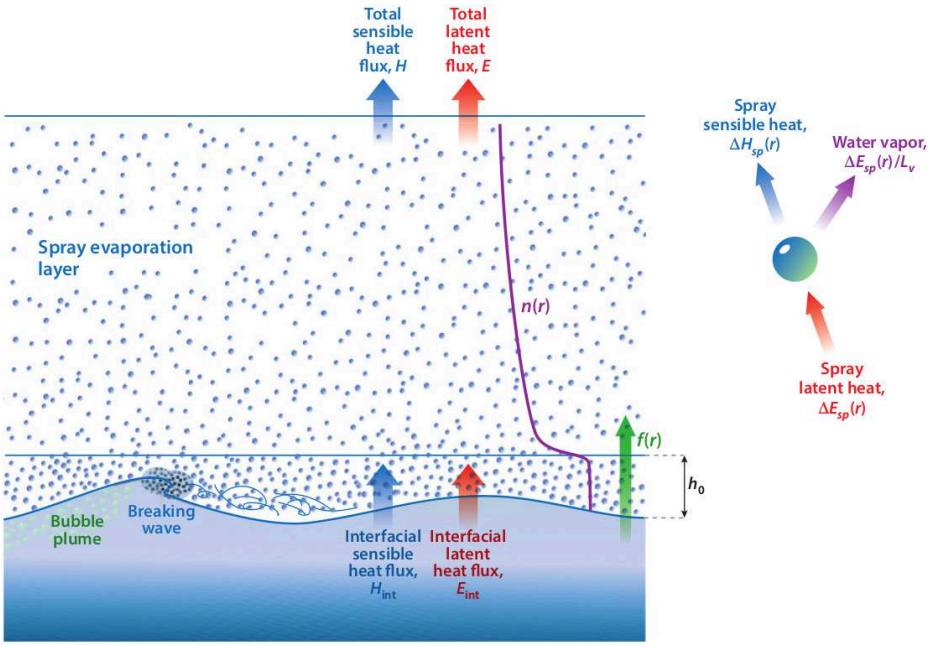

In a gas turbine combustor, as represented in Fig. 1.5, basically, the liquid fuel jet is injected and atomizes into several droplets to generate a polydisperse spray with multiple droplets of different sizes, which evaporate in the hot gaseous medium. Then, the vapor fuel mixes with the oxidant and, finally, burns. In this context, accurate prediction of vapor fuel concentration is essential to correctly model the whole spray combustion process. Some parameters, as droplet evaporation rate and lifetime, are critical for design and operation of those devices (TURNS, 2000). As a conclusion, droplet evaporation modeling is crucial to increase efficiency and reduce environmental impact of liquid-fueled systems.

Figure 1.5: Simulation of a gas turbine combustor in which the fuel droplets are shown in green (PITSCH, 2006).

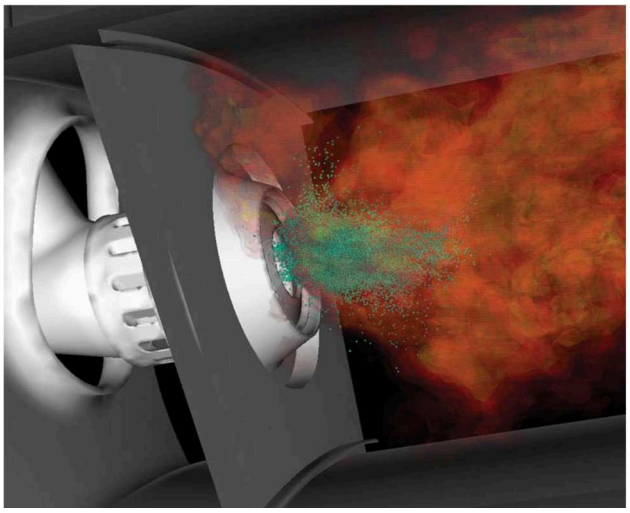

1.2.2 Validation database

Since spray simulations results are strongly influenced by the droplet evaporation model adopted, validation of theoretical models is indispensable. Miller, Harstad and Bellan (1998), for instance, already reviewed most of the well-established droplet evaporation models that are usually used in spray simulations to examine their validity. By means of an extensive model comparison accounting for eight different models and considering five different liquids for cases of low to high evaporation rates, they have concluded that, in general, the non-equilibrium formulation agrees most favorably with a wide range of experimental measurements. Nevertheless, their conclusions were based on experimental measurements whose accuracy may have been deteriorated by extra energy sources, which are not part of the physical model considered to develop the droplet evaporation models.

To begin with, the majority of experiments performed to study the evaporation of a single droplet, specially the elder ones, have used the classical single fiber technique, in which the droplet is suspended by a fiber. However, some studies (YANG; WONG, 2002; GHATA; SHAW, 2014) have already shown that the single fiber technique actually increases the droplet evaporation rate significantly, since there is an energy transfer from the fiber to the droplet through conduction. For smaller droplets, the presence of positioning fibers or thermocouples influences even more the evaporation rate, considering that those devices have a non-negligible diameter compared to the droplet size.

Secondly, some experiments, as, for instance, the one presented in Nomura *et al.* (1996) for a single n-heptane droplet at a wide range of ambient conditions, also have a contribution of the radiation emitted by the internal walls of the furnace where tests were conducted (YANG; WONG, 2001).

In order to assure experimental data reliability, recent experiments have been more mindful to avoid those extra energy sources by using new techniques. Therefore, there is a need to better investigate the validity of theoretical droplet evaporation models by comparing their predictions against experimental measurements performed applying those new techniques.

Chauveau *et al.* (2008), for example, used the cross-fiber technique in order to avoid conduction effects. For this new experimental approach for the characterization of evaporating droplets, the fiber diameter is 14 μm, whereas, for the single fiber technique, traditional fiber diameters are larger than 120 μm. Chauveau *et al.* (2008) have concluded that the droplet evaporation rate increases linearly with the fiber cross-sectional area, corroborating the use of the cross-fiber technique. The cross-fiber technique also ensures droplet spherical shape (VERWEY; BIROUK, 2017), which is an assumption usually adopted in theoretical models, without microgravity condition, as showed in Fig. 1.6. Moreover, while the experimental data using suspended technique are limited to rather large droplets, the cross-fiber technique enables more realistic experiments, considering that spray Sauter mean diameters tends to be below 100 μm for practical purposes in the combustion area (LEFEBVRE, 2010).

Figure 1.6: Droplet suspending techniques (CHAUVEAU *et al.*, 2008).

(a) Classical single fiber

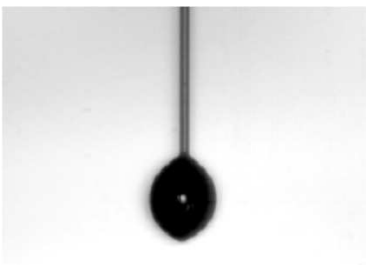

(b) Cross-fiber

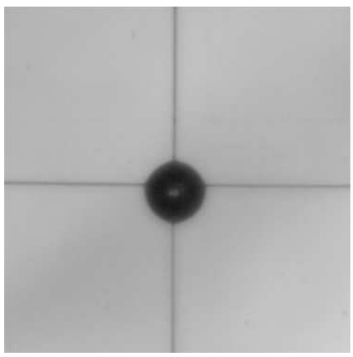

Finally, it is important to highlight that for validation of theoretical models choosing experiments performed under conditions closer to the assumptions adopted for their derivation is a cautious decision. Another possibility to study droplet evaporation is letting it fall down by

gravity, but this technique actually introduces convective effects due to the slip velocity and a certain degree of asymmetrical evaporation, which violates the spherical symmetry assumption usually adopted. In order to eliminate these convective and buoyancy effects, experiments have to be performed in drop towers or parabolic flights to achieve microgravity condition, increasing the experimental set-up complexity and cost.

1.2.3 Alternative fuels

In 2012, fossil fuels accounted for 84% of worldwide energy consumption. In 2040, even with the increase in renewable and nuclear energy, predictions have shown that fossil fuels will still account for 78% of energy use (IEA - International Energy Agency, 2016). As a consequence, the majority of the work that has already studied effects of ambient pressure and temperature on droplet evaporation focused on fossil fuel components evaporation. However, as stated by Bergthorson and Thomson (2015), there is a huge concern over greenhouse-gas emissions and petroleum scarcity that motivates a search for alternative fuels. In this context, ethanol is considered a clean, efficient, and affordable energy source solution.

Ethanol is considered a promising alternative fuel because it is derived from biomass via established and new processes, as proved by the evolution from first to third-generation biofuels; it seems to be easy merging its production and use with the existing infrastructure; and it has advantages when compared with conventional fuels. If compared with gasoline, to illustrate, ethanol has a significantly higher octane number and latent heat of evaporation, which improves thermal and volumetric efficiencies and may reduce emissions of pollutants, such as carbon monoxide, exhaust hydrocarbons and fine particulates (AGARWAL, 2007; WESTBROOK, 2013; QUIROGA; BALESTIERI; ÁVILA, 2017).

Ethanol may be considered the most widely used biofuel in the world (SARATHY *et al.*, 2014), concentrating its largest production in the United States, followed by Brazil. In 2017, these two countries accounted for about 84% of the total global fuel ethanol production, which was approximately 87 billion liters (RFA - Renewable Fuels Association, 2017), as presented in Fig. 1.7. The use of pure ethanol as automotive fuel is mainly limited to Brazil, while blends with gasoline are mostly used as fuels in Europe, United States, China and Canada (CORSETTI *et al.*, 2015). As a result, recently, several authors have been interested in studying ethanol

blends (SAZHIN *et al.*, 2010; CAMPOS-FERNÁNDEZ *et al.*, 2012; BADER; KELLER; HASSE, 2013; MA *et al.*, 2015; QUBEISSI; SAZHIN; ELWARDANY, 2017; YI *et al.*, 2017; KUSZEWSKI, 2018) as an alternative to pure fossil fuels that would not drastically change evaporation and combustion characteristics in the already existing engines.

Figure 1.7: Global fuel ethanol production by country in 2017 in million liters with share of global production (RFA - Renewable Fuels Association, 2017).

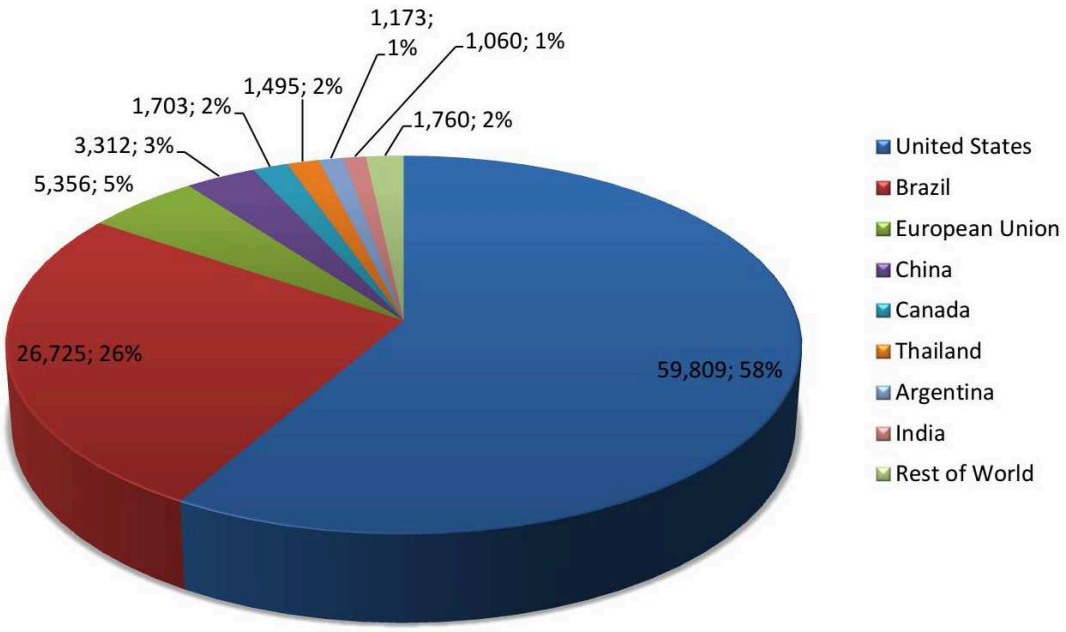

Many experiments have been performed to study droplet evaporation for different fuels and under several ambient conditions (WONG; LIN, 1992; NOMURA *et al.*, 1996; GHASSEMI; BAEK; KHAN, 2006; CHAUVEAU *et al.*, 2008; HASHIMOTO *et al.*, 2015; HAN *et al.*, 2016; BORODULIN *et al.*, 2017). The effects of ambient pressure on n-heptane and kerosene droplet evaporation have been experimentally examined by Nomura *et al.* (1996) and Ghassemi, Baek and Khan (2006), respectively. Both of them stated that droplet lifetime decreases monotonically when gas temperature increases. Nonetheless, as pressure increases, evaporation rate increases at low gas temperature and decreases at high temperature. Similarly, Harstad and Bellan (2000) and Kitano *et al.* (2014) numerically studied those effects on n-heptane and n-decane droplets and arrived to the same conclusions. Although some of these authors have studied the evaporation dynamics under technical system typical conditions, none of them analyzed the effects of ambient conditions on evaporation of pure ethanol droplets.

In the present work, an in-depth investigation of ambient pressure and temperature im-

pacts in the ethanol evaporability is performed aiming to make feasible the development of new technologies for ethanol-fueled internal combustion engines, resulting in more functional and economical devices. This motivation is specially important in what concerns Brazilian interests.

1.3 Objectives

The main objectives of the present dissertation are, first, to implement and validate Lagrangian droplet evaporation models, and second, to use these models to pursue a deeper insight on the physical phenomena that may be involved in the droplet evaporation process. Therefore, the specific objectives are:

- To review some existing models for droplet evaporation under the Lagrangian approach that are usually used for academic research and industrial applications;
- To develop the physical and mathematical models of the studied problem proposed taking into account the key processes involved, such as mass, energy and momentum transfers between phases;
- To evaluate and compare different evaporation models;
- To implement those evaporation models in the in-house code MFSim, which is under development in the Fluid Mechanics Laboratory of the Federal University of Uberlândia;
- To validate evaporation model predictions by comparison with experimental measurements reported in literature;
- To investigate ambient condition influences on droplet evaporation rate.

1.4 Methodology

The Eulerian-Lagrangian approach, has been widely employed for dilute spray simulations, where the droplets are represented as point sources. Thus, each individual droplet is tracked in its own frame of reference and ordinary differential equations are considered to determine position, velocity, diameter and temperature temporal evolution of each droplet. These equations are derived considering linear momentum, mass and energy exchange by droplet-gas interaction.

Point droplet approximations are well justified for droplet sizes below the Kolmogorov length scale, as in the cases studied in the present research. However, this approach can be problematic for larger droplets, demanding an additional modeling to properly account for the interference of the dispersed phase in the flow field.

To study any physical phenomenon, the coming steps should be considered:

- Description of the physical model that represents the problem of interest and the simplifying assumptions;
- Derivation of the mathematical model based on the assumptions;
- Definition of the numerical schemes used to solve the equations proposed in the mathematical model;
- Implementation of the computational model;
- Verification and validation of the code to assure its reliability;
- Simulations to investigate new configurations;
- Discussion of the obtained results.

The focus of the present dissertation is not only on the physical modeling of droplet evaporation, but also on the further development of an existing CFD software, the in-house code MFSim that is presented in Chapter 5. Therefore, a massive amount of knowledge and effort is required to translate differential and algebraic mathematical equations into algorithms and code lines.

1.5 Dissertation outline

The present dissertation consists of 7 chapters and 1 appendix. In Chapter 1, which was already presented, the authors present some background information of the present work, clarify the motivation and objectives, and draw an overall picture of the studies that are conducted, including the methodology followed.

Problem modeling was divided into four topics: physical, mathematical, numerical and computational models. In Chapter 2, the authors propose the problem studied, briefly describe

the physical model and state the main simplifying assumptions adopted. In Chapter 3, the mathematical models used to represent the droplet evaporation process treated with the Lagrangian approach are reviewed. In Chapters 4 and 5 some aspects of the numerical and computational models are explained, such as time integration schemes, interpolation algorithm, parallel implementation and the Lagrangian solver.

In Chapter 6, the authors show the results and discussions. The results comparing two time integration schemes are presented in the first section. Droplet evaporation model validation for water and n-heptane is presented in the second section. Once the models are verified, validated and evaluated, non-equilibrium effects are studied in the third section. Natural convection effects are investigated for n-heptane and forced convection effects are analyzed for n-decane in the fourth and fifth sections, respectively. Ambient condition effects are studied for ethanol in the sixth section and, finally, the seventh section presents some simulations performed with the in-house code MFSim.

In Chapter 7, the authors summarize the major findings, present the conclusions and give the recommendations for future work. The last part, Appendix A, has been dedicated to display some implementation details of the evaporation routines added into MFSim, more specifically, the functions calling the open source package Cantera to access vapor and gas physical properties.

CHAPTER II

PHYSICAL MODEL AND SIMPLIFYING ASSUMPTIONS

Knowing that the evaporation process is quite complex and depends on many factors, it becomes necessary to adopt some hypotheses to simplify the models that represent it. As long as the point droplet approximation is adopted, as stated in Section 1.4, the description of the dispersed phase reduces to modeling the phenomena acting on the droplets. Considering the restrictions imposed by computational requirements and the purposes of the present research, some simplifying assumptions are considered when modeling droplet evaporation. The main simplifications employed to the description of the dispersed phase are given in the next paragraphs.

Droplets are treated as spherical non-deformable liquid structures, meaning that breakup mechanisms are not modeled. For droplets larger than the Kolmogorov scale, transient deformation occurs and the evaporation behavior becomes more complex. Since for high liquid-gas specific mass ratio the droplet equation of motion is governed mainly by drag and gravity forces, the other forces acting on the droplet will be neglected, as presented in Section 3.1. Droplet-droplet interactions, such as collisions and coalescence, are assumed negligible.

Energy transfer between liquid and gaseous phases is assumed to occur only through convection, neglecting radiation. During the initial stage of the droplet lifetime, a transient heat-up period, the energy received by the droplet is utilized to heat-up the liquid to its equilibrium temperature. Once this temperature is achieved, all the energy transferred into the droplet is exclusively employed to gasify the liquid. In other words, the net energy flux penetrating the

droplet surface is zero, so the droplet temperature, T_d, remains constant.

Due to the balance between heating and cooling, liquid droplets usually do not reach the boiling point, T_b, when they are heated. Instead, in absence of radiation, the temperature evolves towards the wet-bulb temperature, T_{wb}, approaching it asymptotically (ABRAMZON; SAZHIN, 2005; ABRAMZON; SAZHIN, 2006), as displayed in Fig. 2.1. Subscripts o and eq refer to initial and equilibrium droplet temperatures, while subscripts h and ev refer to heat-up and total evaporation times. The droplet temperature evolution is determined by a balance between conductive heating and evaporative cooling, and the droplet equilibrium temperature value reached depends on the ambient conditions.

Figure 2.1: Schematic representation of droplet temperature evolution during its evaporation in absence of radiation.

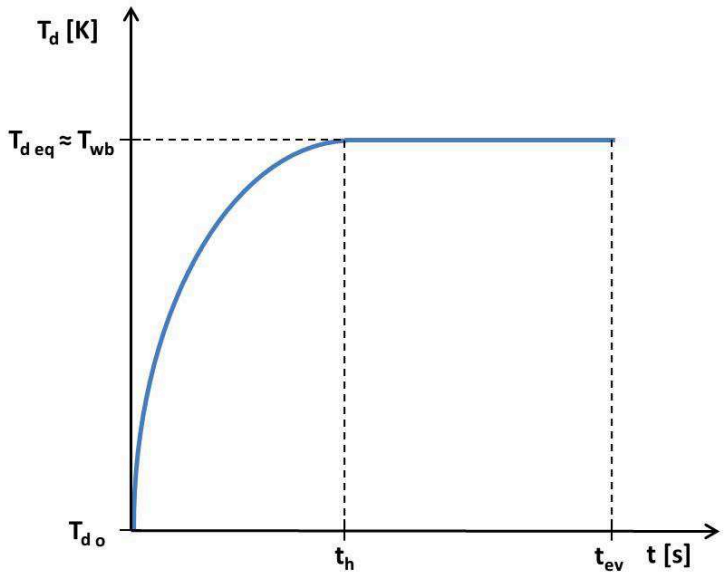

After the initial heat-up period, the well-known D^2 law is obeyed, which means that the square of the droplet diameter, D_d, decreases linearly with time. This behavior occurs because energy and mass diffusion in the surrounding gaseous film are the rate-controlling processes. Therefore, an area reduction rate, K, can be estimated as the negative slope of the variation of the squared droplet diameter in the steady-state evaporation period, as represented in Fig 2.2.

The liquid is composed of a single chemical specie, so no multicomponent aspects are considered. For multicomponent cases, a deviation from the D^2 law is expected, since the more volatile substances evaporate faster, and mass diffusion in the liquid phase becomes important.

Following the heating models classification proposed by Sirignano (2010), the infinite con-

Figure 2.2: Schematic representation of squared droplet diameter evolution during the evaporation of a single-component droplet, showing the linear behavior after the heat-up period.

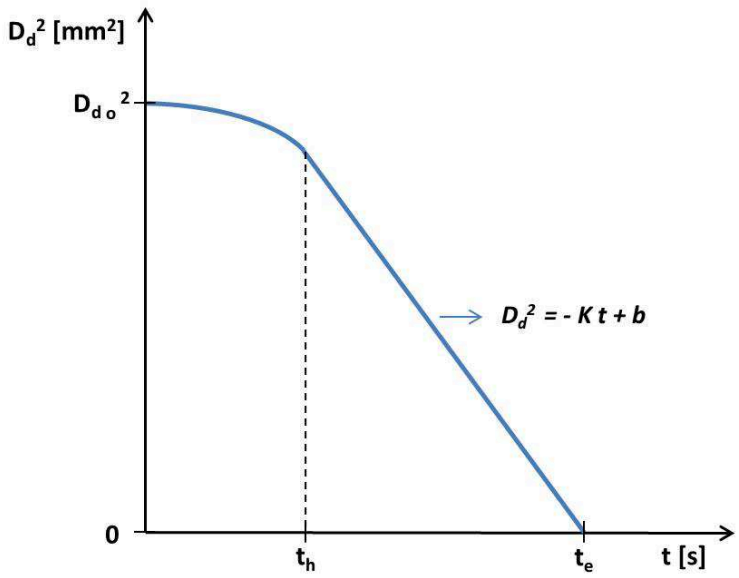

ductivity model is adopted, which is also called in the literature as the rapid mixing model. The thermal conductivity in the liquid phase is assumed infinite, which results in a homogeneous temperature distribution over the droplet volume. Even though the droplet temperature is considered as uniform, it still varies with time. According to Ma (2016) and Sazhin (2017), the infinite conductivity model is usually used for academic research and industrial applications CFD simulations due to its computational efficiency and easy implementation.

Droplet inner flow is not computed and the effects of temperature gradient inside droplets are ignored. Resolving the internal droplet recirculation flow increases the computational cost significantly because a differential equation needs to be solved for the liquid temperature. However, this does not lead to better predictions of droplet diameter or temperature for cases with small droplet initial diameter (BEISHUIZEN, 2008).

The evaporation rate of the single droplet is calculated under the assumption that the variations of the gas temperature and vapor mass fraction caused by the droplet evaporation are negligibly small. In other words, the isolated droplet evaporation does not affect the infinite gaseous medium conditions. This assumption is in fact reasonable for a dispersed two-phase flow case. However, for dense two-phase flows, it was proved that increasing the number of droplets per unit volume reduces the evaporation rate (VOLKOV; KUZNETSOV; STRIZHAK, 2016; CASTANET *et al.*, 2016).

For ambient pressure and temperature below the critical condition, the droplet remains in the liquid state throughout its whole lifetime. The liquid specific mass is much larger than that of the surrounding gas, while the thermal diffusivity in the gas phase is much larger than the liquid-phase thermal diffusivity. The large ratio between the phases properties implies that the liquid phase has higher thermal and mass inertia as compared to the gas phase. Therefore, the processes that occur in the gas phase can be assumed to be quasi-steady. This assumption indicates that the gas-phase immediately adjusts itself to the local boundary conditions and droplet size at each instant of time.

A quasi-steady assumption is often made for the gas-phase because energy and mass diffusion is usually relatively fast compared with that of the liquid. This assumption weakens as the critical condition is approached. According to Sirignano and Law (1978), for near-critical or supercritical evaporation occurring typically in rocket motors and diesel engines, for instance, unsteady gas-phase analysis are required, meaning that the gas-phase time derivatives should be retained for the evaporation model derivation. Only droplet evaporation in subcritical conditions is evaluated in the present research; however, further discussions of models validity and droplet evaporation behavior in near-critical and supercritical conditions can be found in Sirignano (2010), Kontogeorgis and Folas (2010), Bellan (2000) and Givler and Abraham (1996).

Spherical symmetry is also assumed, meaning that convection is absent and, hence, droplet remains spherical during its whole lifetime. The effects of natural and forced convection are taken into account using empirically established laws, since convective effects generate a certain degree of asymmetrical evaporation. These effects are usually expressed introducing correlations to Nusselt and Sherwood numbers by incorporating Reynolds and Grashof numbers into their calculations. Different empirical correlations are available in the scientific literature (FRÖSSLING, 1938; RANZ; MARSHALL, 1952a; CLIFT; GRACE; WEBER, 1978; RENKSIZBULUT; YUEN, 1983; KULMALA *et al.*, 1995), and they have been implemented either in single droplet or spray calculations.

Thermal energy flux can be generated not only by the existence of temperature gradients, but also by concentration gradients. Similarly, mass flux, which is provided by concentration gradients, can also be promoted by temperature gradients. The energy flux caused by concentration gradients is known as Dufour effect, while the mass flux caused by temperature gradients is

known as Soret effect. These two effects occur simultaneously and they are secondary diffusion processes. In the present research, Soret and Dufour effects are not considered, since their order of magnitude is much smaller than that of Fick and Fourier laws (SAZHIN, 2006).

In Figure 2.3, the authors illustrate the described physical model, in which Y_v represents vapor mass fraction, R_d represents droplet radius, and subscripts s and g, refer to droplet surface and far from the droplet or out of the gas-vapor film, respectively. In Figures 2.4a and 2.4b, the authors show the mass and energy transfers involved in the evaporation of a single droplet, where δ_M and δ_T represent the thicknesses of the mass and thermal films, respectively. These surrounding gaseous films are always treated as a mixture of vapor and ambient gas.

From Fig. 2.4b, one can see that the energy effectively received at the droplet surface, Q_d, is equal to the sum of the latent heat of evaporation, Q_L, and the sensible heat, Q_S, and it is also equal to the difference between the total energy transferred from the gas to the droplet, Q_{g-d}, and the energy transferred from gas to vapor that is carried away from droplet by diffusing vapor in form of superheat, Q_{g-v}.

Figure 2.3: Schematic representation of an evaporating droplet surrounded by gas with vapor mass fraction and temperature distributions along the radial direction.

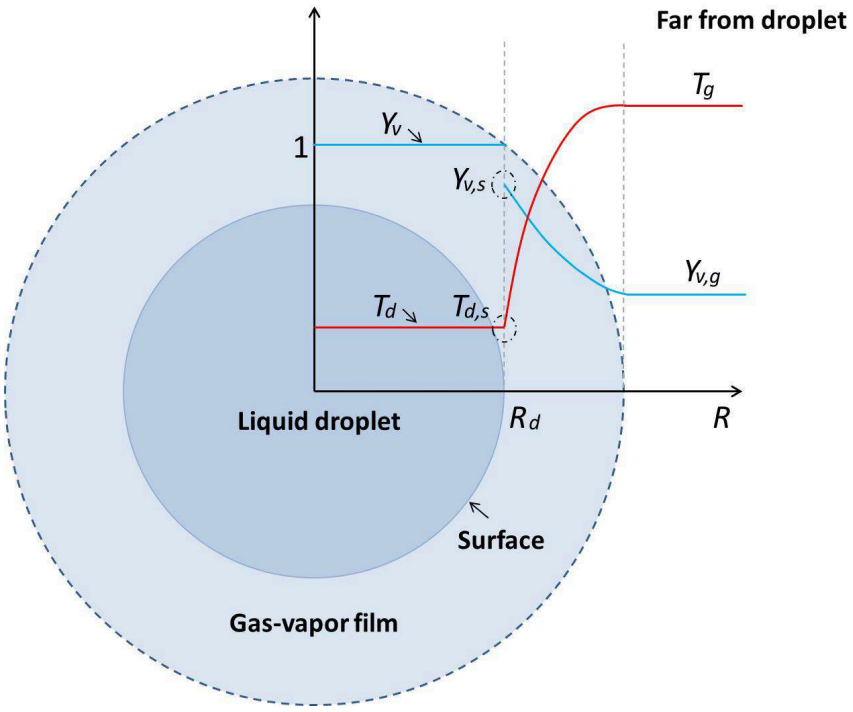

Figure 2.4: Schematic representation of thermal energy and mass transfers in the evaporation of a single droplet.

(a) Sketch of the mass transfer in the evaporation of a single droplet, in which vapor A advective transport represents the well-known Stefan's flow, which is explained in Section 3.2.

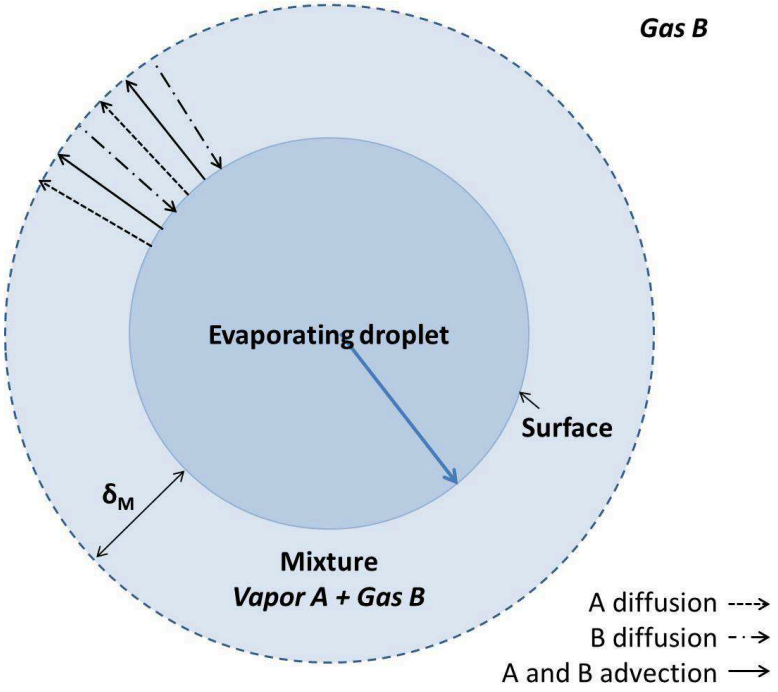

(b) Sketch of the thermal energy transfer in the evaporation of a single droplet.

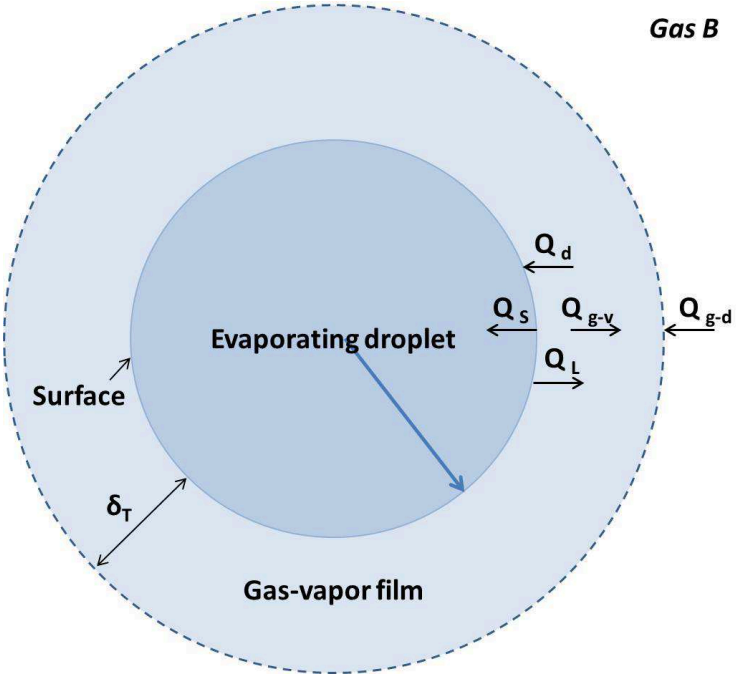

CHAPTER III

MATHEMATICAL MODEL

Accurate droplet displacement and evaporation predictions are crucial in modeling dilute spray evaporation, since they are considered rate limiting processes (JENNY; ROEKAERTS; BEISHUIZEN, 2012). Some parameters, as vapor concentration and droplet lifetime, are specially important for design and operation of energy systems. With this in mind, the purpose of this chapter is to present the mathematical formulation used to represent those processes.

3.1 Displacement model

For engineering applications involving spray evaporation, the droplet drag force and the gravitational force, also known as body force, are predominant compared to other forces, as Basset history, added mass, Magnus, Saffman, buoyancy and pressure gradient terms (SHIROLKAR; COIMBRA; MCQUAY, 1996). Under these conditions and considering the Lagrangian approach, droplet motion and momentum equations are:

$$\frac{d\mathbf{x}_d}{dt} = \mathbf{u}_d, \tag{3.1}$$

$$\frac{d\mathbf{u}_d}{dt} = \frac{\mathbf{u}_g - \mathbf{u}_d}{\tau_d} + \mathbf{g}, \tag{3.2}$$

where $\mathbf{x}_d$ and $\mathbf{u}_d$ are droplet position and velocity, respectively, $\mathbf{u}_g$ is the carrier gas velocity, and $\mathbf{g}$ is the gravitational acceleration. The droplet relaxation time, τ_d, is determined by:

$$\tau_d = \frac{4}{3}\frac{\rho_l}{\rho_g}\frac{D_d}{C_D|\mathbf{u}_g - \mathbf{u}_d|}, \tag{3.3}$$

where ρ_l and ρ_g respectively refer to liquid droplet and gas phase densities. The drag coefficient, C_D, is given by semi-empirical correlations. A frequently used one is the Schiller-Naumann correlation for solid non-evaporating spheres, which is given by (CLIFT; GRACE; WEBER, 1978):

$$C_D = \begin{cases} \frac{24}{Re_d}, & \text{if} \quad Re_d < 0.1 \\ \frac{24}{Re_d}(1 + 0.15Re_d)^{0.687}, & \text{if} \quad 0.1 < Re_d \leq 1000 \\ 0.44, & \text{if} \quad Re_d > 1000 \end{cases}, \tag{3.4}$$

in which the droplet Reynolds number, Re_d, is defined as:

$$Re_d = \frac{\rho_g D_d |\mathbf{u}_g - \mathbf{u}_d|}{\mu_g}, \tag{3.5}$$

where μ is the dynamic viscosity.

Since the Stefan's flow reduces the drag coefficient (ABRAMZON; SIRIGNANO, 1989), Sazhin *et al.* (2005) have suggested a modification of C_D for evaporating droplet:

$$C_{Dev} = \frac{C_D}{(1 + B_M)^{\alpha_M}}, \tag{3.6}$$

where B_M is the Spalding mass transfer number given by:

$$B_M = \frac{Y_{vs} - Y_{vg}}{1 - Y_{vs}}, \tag{3.7}$$

recalling that Y_{vs} and Y_{vg} are the vapor mass fraction at the droplet surface and far away,

respectively, and α_M is:

$$\alpha_M = \begin{cases} 1, & \text{if} \quad B_M < 0.78 \\ 0.75, & \text{if} \quad B_M \geq 0.78 \end{cases}. \tag{3.8}$$

3.2 Evaporation models

Introductory descriptions of evaporating droplet behavior can be found in the work of Williams (1985), Kuo (2005) and Turns (2000), while a comprehensive and in-depth discussion of droplet evaporation under a variety of conditions can be found in the classical textbook of Sirignano (2010). Furthermore, useful research reviews are given by Sazhin (2006) and Sazhin (2017) summarizing various droplet evaporation and heating models, with different levels of complexity. In these reviews, it is also pointed out that detailed models based on single droplet analysis have to be simplified to simulate evaporating spray using CFD methodologies aiming at computational efficiency.

In this chapter, some standard single droplet evaporation models are presented taking into account the two key processes involved in the evaporating phenomenon, mass and energy transfer. These processes are described by differential equations, which express the temporal changes of droplet size and temperature. Considering the assumptions presented in Chapter 2, these equations are:

$$\frac{dm_d}{dt} = -\dot{m}_d, \tag{3.9}$$

where m_d is the droplet mass and $\dot{m}_d$ is the droplet evaporation rate that leads directly to droplet size reduction:

$$\frac{dD_d}{dt} = -\frac{2\dot{m}_d}{\pi \rho_l {D_d}^2}, \tag{3.10}$$

and

$$\frac{dT_d}{dt} = \frac{Q_S}{m_d c_{pl}}, \tag{3.11}$$

where c_{pl} is the liquid droplet specific heat capacity and recalling that Q_S is the power transferred to promote the droplet thermal energy variation per unit of time, which is transferred as heat.

3.2.1 Classical evaporation model

The basis of the theory on droplet evaporation in gaseous medium was laid by Maxwell. Back in 1877 (MAXWELL, 2011), he proposed the simplest evaporation model, considering the stationary evaporation rate for a spherical droplet, motionless relative to an infinite and uniform gaseous medium. In addition, the concentration of the vapor at the droplet surface was assumed to be equal to its equilibrium concentration, or, in other words, the saturated vapor concentration at a given droplet temperature (BRADLEY; FUCHS, 1959). In this simple case of steady evaporation, without advection, the rate of evaporation, or mass flow, is given by the equation known as the Maxwell equation. Its main limitation is to assume that the driving force for liquid evaporation is the difference in vapor concentration between the droplet surface and the free stream, suggesting that the process is exclusively controlled by the diffusion mechanism and neglecting the mass flow resulting from Stefan's flow.

The Classical Evaporation Model (CEM), also known as Stefan-Maxwell model or rapid mixing model, was first reported by Spalding (1953) and Godsave (1953). Its major advance compared with the simplest evaporation model proposed by Maxwell was incorporating the Stefan's flow, which is depicted in Fig. 2.4a. This advective or bulk motion of the vapor directed away from the evaporating surface was first noted by Stefan in 1881 during his research on free surface evaporation (STEFAN, 1881; BRADLEY; FUCHS, 1959).

In Figure 2.4a, the authors show a diagram of the processes involved in the evaporation of a droplet in quasi-steady gaseous medium with constant pressure and temperature. Thermodynamic equilibrium between the liquid and vapor phases at the droplet interface is assumed. Therefore, the vapor pressure at the droplet interface should be equal to the saturation pressure of the evaporated substance at the droplet surface temperature. As the ambient gas is not saturated,

there will be a concentration gradient between the droplet surface and the environment due to the droplet evaporation process, resulting in diffusion of the vapor A away from the droplet. Such mass flow, which is sustained by the droplet evaporation itself over time, induces an overall movement of both vapor A and gas B by advection. Likewise, the gas is diffused from the environment to the droplet surface as a function of a concentration gradient. As the gas is insoluble in the liquid, making the gas-liquid interface impermeable, the net mass flow of gas through the interface will be null. Thus, under permanent conditions and considering that the droplet interface retreats so slowly that it can be considered stationary, the advection of the gas is counterbalanced by its own diffusion (SOM, 2008).

Vapor transport by advection is usually referred in literature as Stefan's flow. Its effect is specially important for evaporation processes in which high evaporation rate is observed or the vapor partial pressure in the ambient is not small compared with the total pressure (DAVIS; SCHWEIGER, 2012). Hence, the instantaneous droplet evaporation rate considering both diffusion and advection, which results in the Stefan-Maxwell equation, is:

$$\dot{m}_d = \pi D_d D_{vm} \rho_m Sh_m ln\left(1 + B_M\right), \tag{3.12}$$

where D_v is the vapor diffusion coefficient, subscript m represents that the physical property is evaluated at the gas-vapor mixture conditions in the film around the droplet, as will be explained in Section 3.2.4, and Sh is the Sherwood number, which is incorporated in order to consider the extra mass transfer due to gas motion around the droplet, represented by the droplet slip velocity, $|\mathbf{u}_g - \mathbf{u}_d|$.

The vapor mass fraction at the droplet surface may be calculated using Raoult's law, which states that the surface vapor molar fraction, χ_{vs}, is equal to the ratio between the vapor partial pressure, p_{vs}, and the ambient gas total pressure, p_g, as shown by:

$$\chi_{vs} = \frac{p_{vs}}{p_g}. \tag{3.13}$$

Therefore, once χ_{vs} is determined, Y_{vs} may be established based on the mean molecular

weight of the mixture definition as:

$$Y_{vs} = \frac{\chi_{vs} W_v}{\chi_{vs} W_v + \chi_{g_s} W_g}, \tag{3.14}$$

where W is the molecular weight; and subscripts v and g refer to vapor and ambient gas, respectively.

There are several empirical and theoretical correlations to determine vapor partial pressure (STEPHAN *et al.*, 2010). If liquid-vapor thermodynamic equilibrium at the droplet surface, which infers that the vapor concentration is always at saturated condition, constant latent heat of evaporation, and ideal gas hypothesis are assumed, the surface vapor molar fraction may be estimated using Clausius-Clapeyron law:

$${\chi_{v_s}}^{eq} = \frac{p_{sat}}{p_g} = \frac{p_{atm}}{p_g} exp\left[\frac{L_v(T_b) W_v}{R_u}\left(\frac{1}{T_b} - \frac{1}{T_d}\right)\right], \tag{3.15}$$

where p_{sat} is the saturation pressure; p_{atm} is the atmospheric pressure; L_v the vapor specific latent heat of evaporation; R_u is the universal gas constant; and T_b is the liquid phase normal boiling temperature, which should be calculated at p_{atm}.

The well-known Ranz-Marshall empirical correlation (RANZ; MARSHALL, 1952a) is used for estimating Sh_m:

$$Sh_m = 2 + 0.6 {Re_d}^{1/2} {Sc_m}^{1/3}, \tag{3.16}$$

where Sc is the Schmidt number given by:

$$Sc_m = \frac{\mu_m}{\rho_m D_{vm}}, \tag{3.17}$$

In the CEM original model reported by Spalding (1953) and Godsave (1953), here denoted as CEM*, the existence of a gas-vapor film around the droplet, where mass and energy transfer between liquid and gas phases happens, was not taken into account. A correction factor, G, for energy transfer reduction due to evaporation, that follows from considering evaporation effects by means of boundary conditions at the droplet surface, was then proposed by Wakil, Uyehara

and Myers (1954). This consideration represents that a fraction of the total energy received at the droplet surface, Q_d, supplies the latent energy of evaporation for the vapor diffusing out, Q_L, while the other part is used as sensible energy to increase the liquid droplet temperature itself, Q_S, during the heat-up period.

As a result, the energy balance equation for the surrounding gas, coupled to the droplet surface boundary conditions, yields the following expression for the thermal energy penetrating into the liquid phase:

$$Q_S = G\pi D_d Nu_m k_m \left(T_g - T_d\right) - L_v \dot{m}_d, \tag{3.18}$$

where k is the thermal conductivity and Nu is the Nusselt number, which is calculated using Eq. (3.16) with Pr_m instead of Sc_m. Pr refers to the Prandtl number given by:

$$Pr_m = \frac{\mu_m c_{p_m}}{k_m}. \tag{3.19}$$

In addition, the correction factor is:

$$G = \frac{\beta}{e^{\beta} - 1}, \tag{3.20}$$

where β is a non-dimensional evaporation parameter:

$$\beta = -\frac{\dot{m}_d c_{p_m}}{2\pi k_m D_d}, \tag{3.21}$$

and B_T is the Spalding thermal energy transfer number:

$$B_T = (1 + B_M)^{\varphi} - 1, \tag{3.22}$$

with,

$$\varphi = \left(\frac{c_{p_v}}{c_{p_g}}\right)\left(\frac{Sh}{Nu}\right)\frac{1}{Le_m}, \tag{3.23}$$

where Le is the Lewis number:

$$Le_m = \frac{k_m}{c_{p_m} D_{vm} \rho_m}. \tag{3.24}$$

It is worth mentioning that in the absence of evaporation, β tends to 0 and, as a consequence, G tends to 1, implying that no evaporation effect is considered.

3.2.2 Abramzon-Sirignano model

The CEM was improved by Abramzon and Sirignano (1989) in order to contemplate the advective mass and energy transport more precisely. The vapor advective transport is caused by two factors: the Stefan's flow and the droplet relative motion to the gas. Based on the film theory (BIRD; STEWART; LIGHTFOOT, 2002), the mass and energy exchange between the droplet surface and the carrier gas flow may be modeled by employing finite and stagnant gas films of thicknesses δ_M and δ_T (see Fig. 2.4). From the boundary layer theory, it is known that the Stefan's flow presence, which is a blowing effect, in evaporating droplets results in the thickening of these films (SCHLICHTING; GERSTEN, 2017). Thus, for the sake of considering the effect explained above, the correction factors for the thicknesses of the diffusional and thermal films, F_M and F_T, should be added in Sh and Nu calculations:

$$F_M = (1 + B_M)^{0.7} \frac{ln\,(1 + B_M)}{B_M}; F_T = (1 + B_T)^{0.7} \frac{ln\,(1 + B_T)}{B_T}, \tag{3.25}$$

where B_M and B_T are given by Eqs. 3.7 and 3.22, respectively, while φ should be computed using Sh^* and Nu^* instead of Sh_m and Nu_m.

The parameters Sh^* and Nu^* are called modified Sherwood and Nusselt numbers, and tend to Sh_m and Nu_m, respectively, as F_M and F_T tend to the unity.

$$Sh^* = 2 + \frac{Sh_m - 2}{F_M}; Nu^* = 2 + \frac{Nu_m - 2}{F_T}, \tag{3.26}$$

recalling that Sh_m and Nu_m are calculated using Eq. (3.16).

Since F_M and F_T physically represent the relative change of the film thicknesses due to Stefan's flow, their values are always higher than 1, implying that mass and thermal energy

transfer are actually reduced by these correction factors in comparison with CEM. Furthermore, it can also be noticed by Eq. 3.26 that as F_M and F_T tend to 1, Sh^* and Nu^* tend to Sh_m and Nu_m, meaning that the Stefan's flow blowing effect is not taken into account.

Finally, the Abramzon-Sirignano Model (ASM) uses the same expressions for droplet evaporation rate and sensible heat than those of the CEM (Eqs. 3.12 and 3.18), but with Sh_m and Nu_m substituted by Sh^* and Nu^*. Moreover, its correction factor is given by:

$$G = \frac{ln\,(1 + B_T)}{B_T}. \tag{3.27}$$

3.2.3 Non-equilibrium model

A model based on the Langmuir-Knudsen evaporation law, which considers non-equilibrium thermodynamic effects, is comprehensively described by Miller, Harstad and Bellan (1998). Bellan and Summerfield (1978) first introduced this treatment for use in droplet combustion models and found non-equilibrium effects to be important for incorporating the realistic non-equilibrium evaporation behavior prevailing in many practical situations, i.e., when the evaporation rate is high. Miller, Harstad and Bellan (1998) also showed that droplet sizes usually found in practical spray calculations present significant non-equilibrium effects. Moreover, Sadiki, Chrigui and Dreizler (2013) state that, for gas turbine combustion spray applications, non-equilibrium models should be used to obtain a thermodynamically consistent formulation.

To take into consideration the non-equilibrium effects, a deviation term must be added in order to correct the equilibrium vapor molar fraction at the droplet surface estimated by the Clausius-Clapeyron law (Eq. 3.15):

$$\chi_{v_s}{}^{neq} = \chi_{v_s}{}^{eq} - \frac{2L_K\beta}{D_d}, \tag{3.28}$$

where L_K is the Knudsen layer thickness given by:

$$L_K = \frac{\mu_m\sqrt{2\pi T_d R_u/W_v}}{\alpha_e Sc_m Pr_m}, \tag{3.29}$$

where α_e is the molecular accommodation coefficient, assumed equal to unity. Hence, the Non-

Equilibrium Model (NEQ) is composed by Eq. (3.12), incorporating the proposed ${\chi_{vs}}^{neq}$ into B_T calculation, and Eq. (3.18).

3.2.4 Gas-vapor mixture properties

As shown in Fig. 2.3, temperature and vapor concentration conditions, as well as physical properties, abruptly change from the droplet surface to the film limit. Due to those large normal gradients near the droplet surface, which are created by droplet evaporation, an averaging procedure may be used in order to determine reference conditions to be used in thermodynamic and transport properties estimation. These reference conditions are given by:

$$T_m = T_s + \alpha_w \left(T_g - T_s\right), \tag{3.30}$$

and

$$Y_{vm} = Y_{vs} + \alpha_w \left(Y_{vg} - Y_{vs}\right), \tag{3.31}$$

where α_w is a weighting parameter for gas-vapor mixture properties evaluation.

Once the physical properties are estimated based on the reference conditions, the mixture properties, denoted with subscript m, are evaluated from the combination of the pure substance properties. In the present study, the Wilke's rule is applied for the dynamic viscosity and thermal conductivity, and the standard additive rules for an ideal gas are used for the mixture density and specific heat capacity.

Hubbard, Denny and Mills (1975) and Yuen and Chen (1976) advise using $\alpha_w = 1/3$, which is the empirical rule typically selected for spray combustion simulations. More recently, Ma, Naud and Roekaerts (2016) appraised the influence of the $1/3$ averaging rule by comparing computational and experimental results. They have concluded that droplet dispersion behavior strongly depends on the criterion used to determine the reference conditions, specially when the difference between droplet and ambient temperature is high. Additionally, they suggested that using directly the carrier gas properties, that is, $\alpha_w = 1$, leads to too fast decay of droplet velocity, and that accurate estimation of Pr_m and Sc_m, and, consequently, Le_m, have a considerable

impact in thermal and mass fluxes predictions.

CHAPTER IV

NUMERICAL MODEL

In this chapter, the numerical methods retained to solve the equations presented in Chapter 3 are explained. Some relevant aspects for the developments carried out in the present work are also discussed in detail.

4.1 Time step calculation

The time step of both continuous and dispersed phases is dependent on the characteristic time scales of the flow field and the numerical methods used to find the solution (PERSSON, 2013). As pointed out by Sommerfeld (2017), there are many unsteady situations where the required Eulerian time step, Δt_{eul}, is much larger than the expected Lagrangian time step, Δt_{lag}.

Using a common time step for both Eulerian and Lagrangian computations would imply that the time step is dictated by the droplet response time, which is usually the smaller time scale. A typical Eulerian time step for URANS or LES simulations may be found of order of Δl or Δl^2, where Δl is the control volume characteristic length (see Fig. 4.2); while Lagrangian time steps may have a smaller order of magnitude, in the range of $\Delta t_{lag} = [10^{-8}s, 10^{-3}s]$ (SOMMERFELD, 2017), depending on the type of dispersed phase and physical phenomena considered. For very small droplets, for instance, their response time is rather low and, hence, limits the Lagrangian time step.

If the Eulerian time step is larger than the Lagrangian one, subiterations should be done

for the Lagrangian calculations. While the numerical scheme of the liquid phase has several time steps, the gas phase remains in a frozen state, meaning that its properties are only updated by the end of all Lagrangian subiterations, as represented by Fig. 4.1.

Figure 4.1: Illustration of the time lines for a Eulerian-Lagrangian simulation with $\Delta t_{eul} > \Delta t_{lag}$.

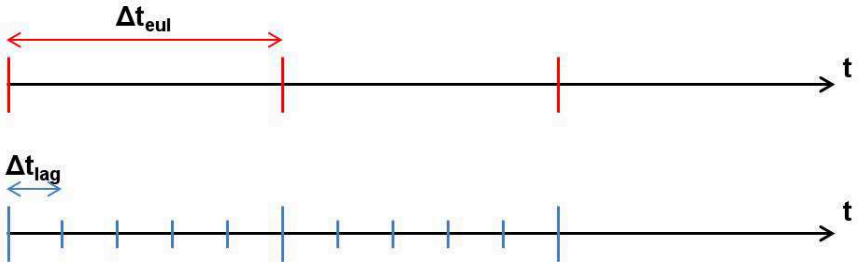

For solving differential equations with different characteristic time scales, variable time step size schemes are often essential to obtain computationally efficient and accurate results. The Eulerian adaptive time step size is determined by a Courant-Friedrichs-Lewy (CFL) condition. However, in the present research, the time step is not only based on gaseous variables; liquid phase effects, like droplet evaporation or displacement, are also taken into account for determining the Lagrangian adaptive time step size.

The time step for the droplet displacement calculation should be automatically adjusted along time by considering all the local relevant time scales, which are also changing throughout the flow field. The characteristic time scales that should be considered are:

- The time required for a droplet to cross a control volume, t_{CV};
- The droplet relaxation time, τ_d;
- The integral time scale of turbulence, t_L.

Hence, the Lagrangian time step must be a fraction of the minimum of these characteristic time scales for accurate calculations, for example 10% as suggested by Sadiki *et al.* (2005):

$$\Delta t_{lag} = 0.1\ min\{t_{CV}, \tau_d, t_L\}. \tag{4.1}$$

Moreover, when evaporation is considered, the evaporation time scale should be also taken into account (XIA *et al.*, 2013). Jaegle (2009) states that a common criterion related to accuracy

of evaporation processes is that during an iteration, the Lagrangian time step is limited so no more than 10% of the current droplet mass evaporates, $\Delta m_d/m_d < 0.1$. Teske, Thistle and Londergan (2009), on the other hand, suggest the Lagrangian time step size to be limited as $\Delta t_{lag} \leq 0.001\ t_{ev}$. It was verified that following the criterion proposed by Teske, Thistle and Londergan (2009) necessarily implies in also obeying the one proposed by Jaegle (2009).

4.2 Time integration

The droplet dynamics and evaporation is determined by a set of ordinary differential equations, which describe the temporal advancement of droplet position (Eq. 3.1), velocity (Eq. 3.2), size (Eq. 3.10) and temperature (Eq. 3.11). Using numerical integration schemes, this set of equations is transformed into algebraic equations, which are solved by an iterative process. In the present dissertation, two numerical methods are employed to perform this task: the first-order Euler method and the fourth-order Runge-Kutta method.

The general form of a first-order ordinary differential equation is:

$$\frac{d\phi_d}{dt} = f\left(\phi_d, t\right), \tag{4.2}$$

where ϕ_d is an arbitrary variable that is transported by a Lagrangian droplet, as $\mathbf{x}_d$, $\mathbf{u}_d$, D_d or T_d, and $f\left(\phi_d, t\right)$ is a given function.

Applying the first-order Euler method explicitly to Eq. 4.2, the value ϕ_d at the new time step $n+1$ reads:

$${\phi_d}^{n+1} = {\phi_d}^{n} + f\left(\phi_d, t\right)|^{n} \Delta t_{lag}, \tag{4.3}$$

where n is a given time step and Δt_{lag} is the Lagrangian time step.

Since the above time integration is a first-order method, its global error, at a given time, is proportional to the step size. Therefore, this method should be used with care in order to ensure that the Lagrangian time step is always low.

On the other hand, applying the fourth-order Runge-Kutta method, also explicitly, to Eq.

4.2 results in:

$$\phi_d{}^{n+1} = \phi_d{}^{n} + \frac{1}{6}(k_0 + 2k_1 + 2k_2 + k_3)\,|^n \Delta t_{lag}, \tag{4.4}$$

with,

$$k_0 = f\left(\phi_d, t\right),\ k_1 = f\left(\phi_d + k_0/2, t\right),\ k_2 = f\left(\phi_d + k_1/2, t\right),\ k_3 = f\left(\phi_d + k_2, t\right). \tag{4.5}$$

Preliminary studies carried out during ASM implementation and verification against Abramzon and Sirignano (1989) results showed that the Euler method was not able to achieve the expected predictions. As a consequence, the mathematical model is integrated with the fourth-order Runge-Kutta method for all cases presented.

4.3 Vanishing droplets

As mentioned by Jaegle (2009), if a droplet evaporates more than its current mass during a time step n, $(m_d - \dot{m}_d \Delta t_{lag} < 0)|^n$, the disappearance of the droplet has to be taken into account. However, in order to do it correctly, the mass decrement during the time step considered must be replaced by $\Delta m_d = -\dot{m}_d \Delta t_{lag}$ the remaining particle mass $\Delta m_d = -m_d$. Then, the droplet in question can be subsequently removed from the calculation.

Another issue when evaporating droplets become too small is that their masses are very close to zero, causing numerical problems in Eq. 3.11, since m_d is in the denominator. This $1/m_d$ term reflects the fact that a droplet with very little mass heats up rapidly when the surrounding gas temperature changes, and the resulting conductive heat up is not immediately equilibrated by the cooling effect of a higher evaporation rate.

In order to avoid this problem, a vanishing droplet criterion must be established. Following Luo *et al.* (2011), once the droplet diameter falls below 0.5 μm, it is removed from the calculation, and the remaining mass, momentum, and thermal energy should be transferred to the gas phase. Although there is no direct physical justification for this procedure, artificially limiting the droplet diameter to finite values is a numerical requirement.

4.4 Interpolation method

In Euler-Lagrangian computations, the location of a discrete droplet not necessarily coincide with the computational grid. Therefore, in order to account for coupling between gaseous and liquid phases, the properties of the carrier fluid, such as $\mathbf{u}_g$, T_g, Y_{vg}, ρ_g and μ_g, must be interpolated at the droplet location.

First, the Eulerian properties, here referred as ψ, should be interpolated from the control volume faces to the nodes of the finite-volume grid. Then, once the values at each node of a given control volume are known, an interpolation method is used to interpolate these properties from the nodes to the droplet position, $\mathbf{x}_d = (x_d, y_d, z_d)$. For a structured grid, consider a hexahedral control volume of dimensions Δx, Δy and Δz containing a droplet inside it, as represented in Fig. 4.2.

Figure 4.2: Schematic representation of the barycentric interpolation, in which the distance between droplet and each control volume node is expressed by D.

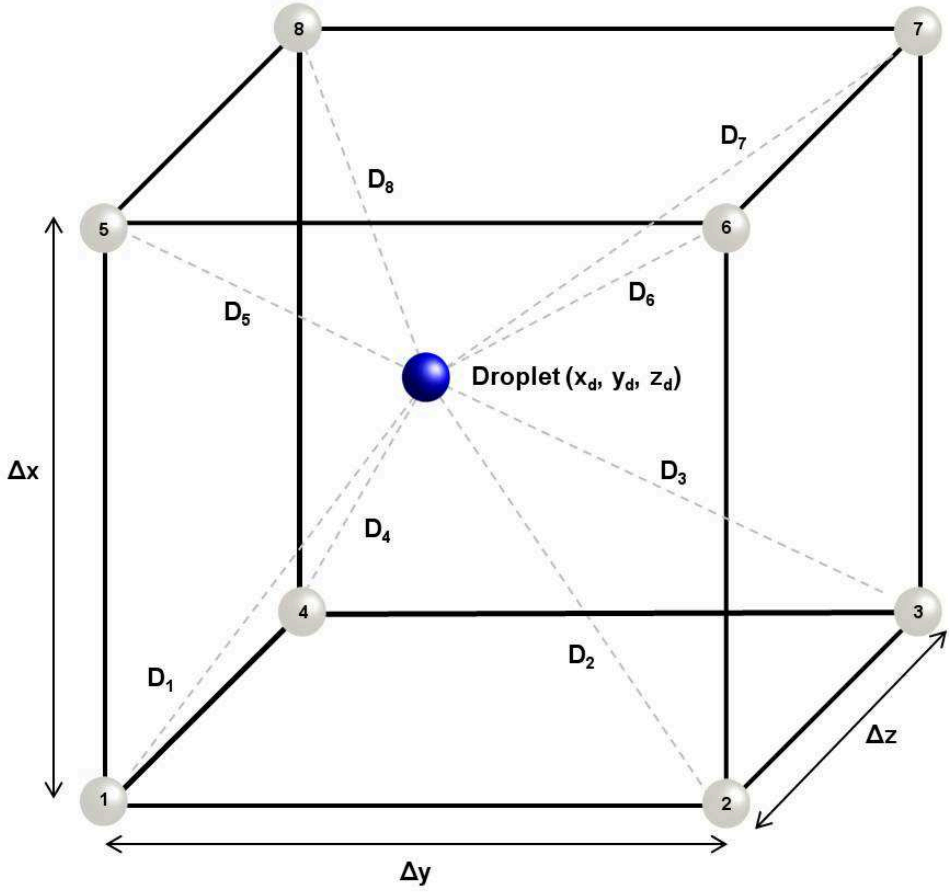

The barycentric interpolation method, which is also known as trilinear interpolation since

it applies the linear interpolation seven times, is based on distance weighting (SCHERER, 2013). In this interpolation method, the Eulerian properties values in each one of the 8 nodes is weighted by the inverse of the square of the distance between each node and the droplet to determine their values at the droplet position:

$$\psi_{\mathbf{x}_d} = \frac{\sum_{i=1}^{8} \left(\psi_{\mathbf{x}_i} / {D_i}^2\right)}{\sum_{i=1}^{8} \left(1/{D_i}^2\right)}, \tag{4.6}$$

where i stands for the node number and

$${D_i}^2 = (D_{xi})^2 + \left(D_{y_i}\right)^2 + (D_{zi})^2 = (x_d - x_i)^2 + (y_d - y_i)^2 + (z_d - z_i)^2. \tag{4.7}$$

More details on the barycentric interpolation method can be found in Silva (2016).

CHAPTER V

COMPUTATIONAL MODEL

The in-house CFD code MFSim has been developed in the Fluid Mechanics Laboratory of the Federal University of Uberlândia over the last 10 years in cooperation with a large research group. Physical problems involving turbulence modeling, fluid-structure interaction, and multi-phase flow with reactive and phase change approaches can already be simulated using this computational platform.

The finite volume method is applied for the Eulerian domain discretization with a staggered three-dimensional grid. The code uses multi-block structured meshes and a variable time step. The computational mesh may be adapted throughout the simulation according to some refinement criteria, e.g. vorticity, immersed boundary position and physical properties gradients. The partial differential equations that model the flow can be described by both divergent and non-divergent approaches. Velocity-pressure coupling can be accomplished using either a two-step projection method or the SIMPLE algorithm. There are several schemes for treatment of advection terms and two families of solvers available, PETSc and multigrid-multilevel. Some previous researches performed using MFSim have already been published, e.g. Ceniceros *et al.* (2009), Pivello *et al.* (2014), Denner *et al.* (2014), Jesus *et al.* (2015), Barbi *et al.* (2016), Damasceno, Santos and Vedovoto (2018), Duarte *et al.* (2018).

The present work development was divided into two main parts. First, a computational routine was implemented in Python to simulate the evaporation of a single droplet in order verify

and validate the evaporation models presented in Section 3.2. Then, the implementations were incorporated into MFSim code. This second stage allowed simulations with multiple droplets and the coupling between Eulerian and Lagrangian phases. In this chapter, the authors briefly describe the MFSim Lagrangian module and, for more details, the reader is referred to previous works. Additionally, some aspects the evaporation routine implemented and applied are elucidated.

5.1 Lagrangian solver structure

Before describing the main features of the MFSim Lagrangian module, the general structure of the Lagrangian solver, as it was specifically applied for the present work, is shown. The sequence of steps followed to simulate a Lagrangian droplet evaporation is summarized in the flow chart sketched in Fig. 5.1, where N_d denotes de number of droplets in the domain and t_{final} the final simulation time.

In order to provide a better visualization of the evaporation mathematical model presented in Section 3.2, the general structure of the Lagrangian evaporation function is presented as a flow chart in Fig 5.2, where the gray colored blocks represent the steps that differ from one model to another.

The physical properties for vapor and gas are obtained utilizing the open source package Cantera, as explained in Section 5.5; while the liquid droplet properties as well as the latent heat of evaporation are calculated based on the database found in Green and Perry (2007), in which ρ_l is expressed by a 4^{th} degree polynomial equation, c_{pl} is given by the Rackett equation and L_v is established by the extended Watson equation. Finally, all the thermodynamic and transport properties for liquid, vapor and gas phases are assumed constant during each time step, but they vary from one time step to another due to the corresponding changes in droplet temperature.

5.2 Data structure

All the data structure used to represent the Lagrangian droplets computationally and store their properties is based on a hash table. Hash table, or hash map, can be defined as a data structure used for looking up items using a unique key. The application of this table in the MFSim code is made through the Uthash package, developed by Hanson (2013) and implemented in C.

Figure 5.1: General structure of the Lagrangian solver.

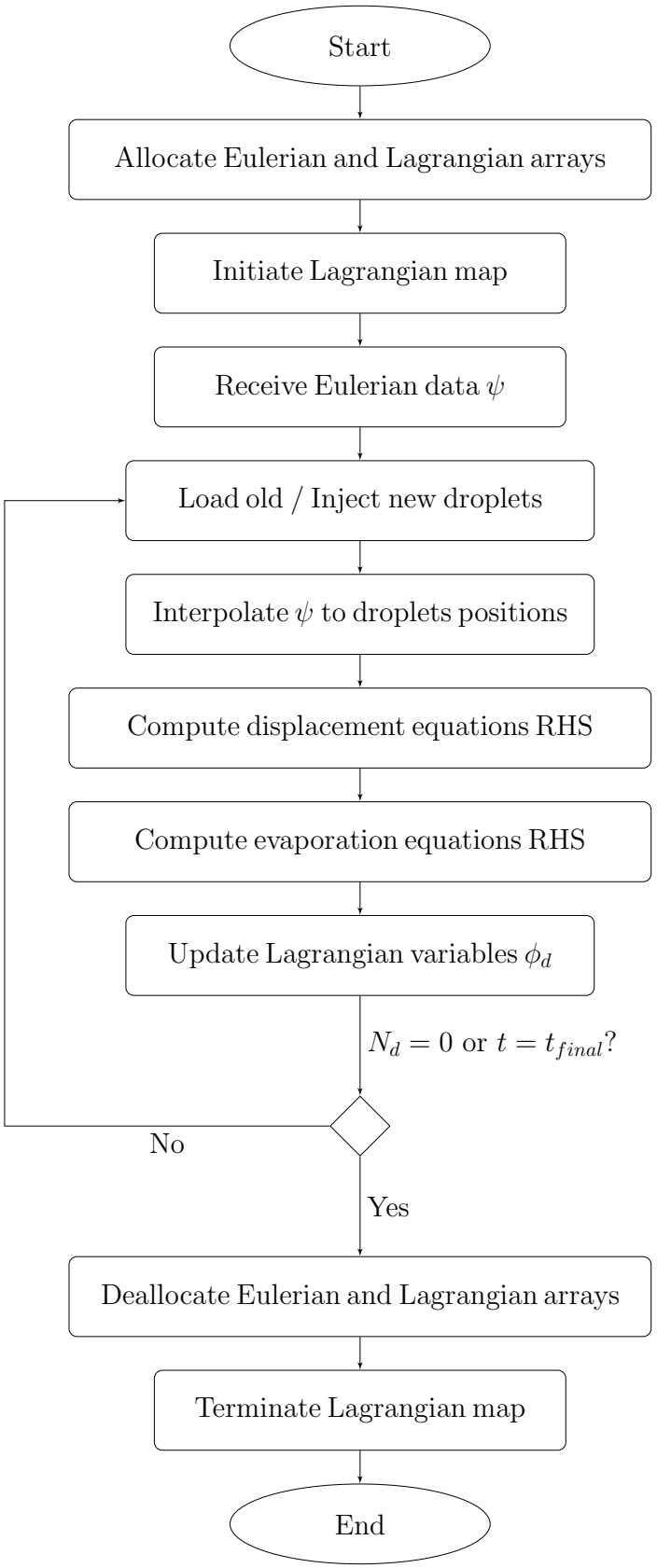

For this reason, much of the Lagrangian module is developed in this same language, even though the base structure of MFSim code and the Eulerian module are developed in Fortran. Therefore,

Figure 5.2: General structure of the Lagrangian evaporation function.

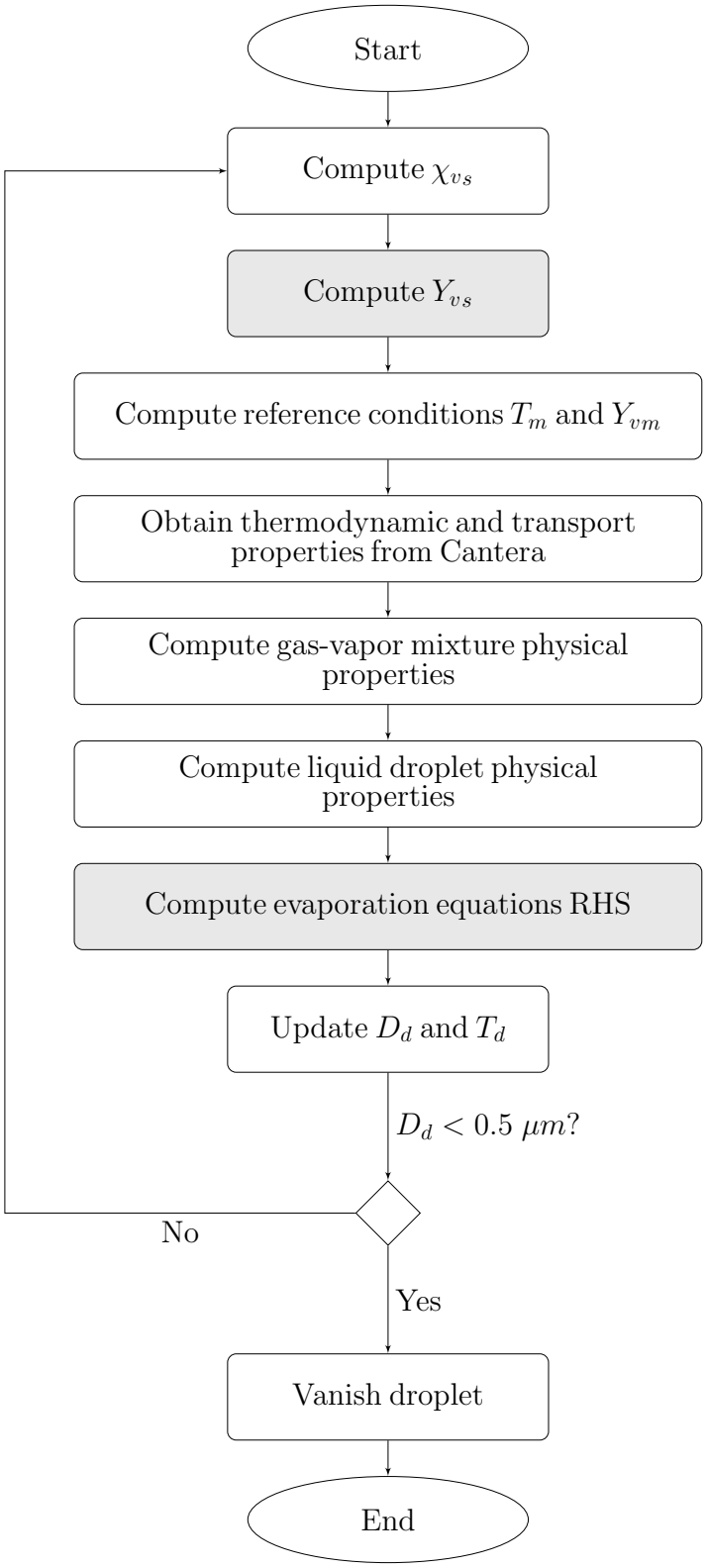

Fortran functions initialize the communicator and further transfer it to C environment. The Fortran/C language linking is better explained in Section 5.6.

In this section, first the Lagrangian map is explained and the hash table use is exemplified;

subsequently, the Lagrangian variables that are associated with each droplet are presented.

5.2.1 Lagrangian map

The Lagrangian map is composed by a multi-level hash table (see Fig. 5.3(c)) and by an independent hash table that saves droplets information (see Fig. 5.3(d)). These two structures, together, are able to determine which droplets dwell in a given cell and which is the host cell of a specific droplet.

The multi-level hash table is a replica of the Eulerian grid, as shown in Fig. 5.3(a), and, as a consequence, it contains the various levels of refinement. If a given cell contains droplets, the multi-level hash table also stores those droplets identifiers (ID), as in the example of Fig. 5.3(b). Each droplet must have an unique ID, since this ID is the table key to access each droplet hash table information.

From a specific droplet ID, or table key, it is possible to access, through the hash function, all other information that accompanies this same ID, without having to cross the entire table content. Thus, the table can contain several droplets and their respective n variables, ϕ_d, as represented in Fig. 5.3(d) for the 6 droplets displayed.

Notice that since the multi-level hash table depends on the Eulerian grid, its structure must be rebuilt at each mesh refinement, for adaptive meshes. Also, the independent hash table to store droplets information is updated during the simulation.

The Uthash package supports the following operations on items in a hash table: add/replace, find, delete and count.

5.2.2 Lagrangian variables

The n variables, ϕ_d, associated with each droplet, as represented in Fig. 5.3(d), are:

- Droplet identifier, id_d: this number is directly used during the simulation to access the hash table information and it can also be used as a label for the reconstruction of droplet trajectories with post-processing tools.

- Processor number, $proc_d$: this information is used during communications of particles that cross the interfaces between subdomains.

Figure 5.3: General structure of the Lagrangian map where **c** and **d** stand for cell and droplet, respectively. (a) Bidimensional block-structured mesh with each ID, where the black points represent the visible cells; (b) Droplets locations in the domain; (c) Multi-level hash table; and (d) Particles hash table.

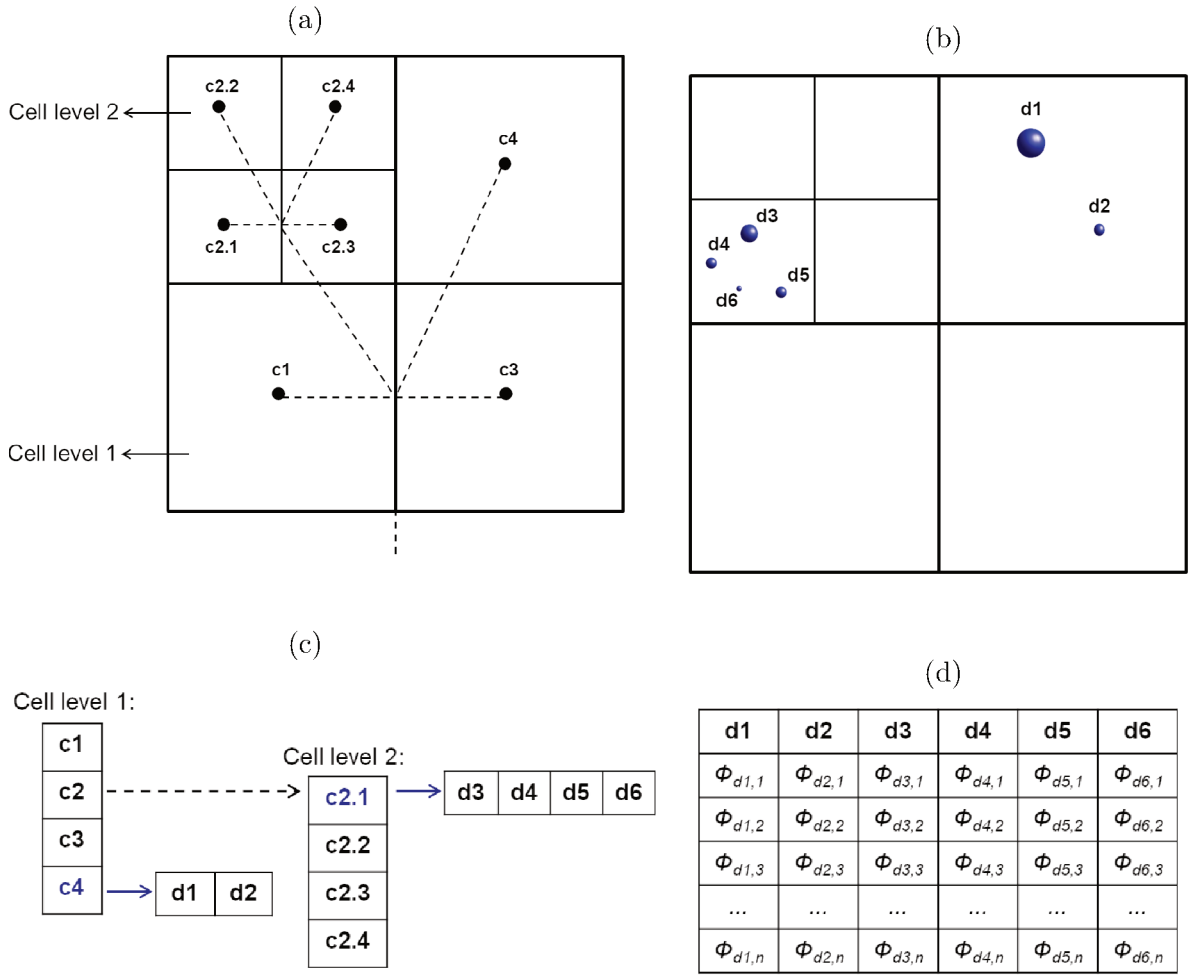

- Cell index, i_{cd}, j_{cd}, k_{cd}: this parameter enables the localization of a droplet inside the computational domain.

- Droplet position, x_d, y_d, z_d: the initial droplet position is an input parameter and the new droplet position is obtained by solving Eq. 3.1.

- Droplet velocity, u_d, v_d, w_d: the initial droplet position is an input parameter and the new droplet position is obtained by solving Eq. 3.2.

- Droplet diameter, D_d: the initial droplet diameter is also an input parameter and the its new value is obtained by solving Eq. 3.10.

- Droplet temperature, T_d: the initial droplet temperature is also an input parameter and the its new value is obtained by solving Eq. 3.11.

5.3 Search algorithm

Droplets may change their position at each time step of the simulation depending on the Eulerian field flow they are exposed to. However, before the field information is sampled for interpolation, the new host cell of each specific droplet must be identified. Therefore, they must be traced through the grid. In a multi-block structured mesh, as the one used in MFSim, the new host cell, whose index is (i_c, j_c, k_c), can be detected with:

$$i_c = int\left(\frac{x_d - x_0}{\Delta x}\right),\ j_c = int\left(\frac{y_d - y_0}{\Delta y}\right),\ k_c = int\left(\frac{z_d - z_0}{\Delta z}\right), \tag{5.1}$$

where the coordinates (x_0, y_0, z_0) refer to the Eulerian domain origin, Δx, Δy and Δz depend on the mesh level, and int denotes truncation to the lowest integer part.

5.4 Parallelization

The parallelization technique applied to Lagrangian module is based on the idea of running Lagrangian and Eulerian solvers simultaneously on each processor. The computational domain is divided into subdomains in such a way that the droplets that are spatially inside the partition associated to a given subdomain are computationally treated by the same processor, as exemplified by Fig 5.4.

The criteria retained to decide domain partition between processors are the load balance of grid cells and the communication demands. In order to achieve high performance, the load of each process must be equalized and the communication among process must be minimized. The Message Passing Interface (MPI) protocol is used for both Lagrangian and Eulerian modules communication. For more details about MPI commands and Lagrangian parallelization, Ferreira (2015) work should be consulted.

Figure 5.4: Domain partition into 8 subdomains, where each subdomain is directed to a different processor.

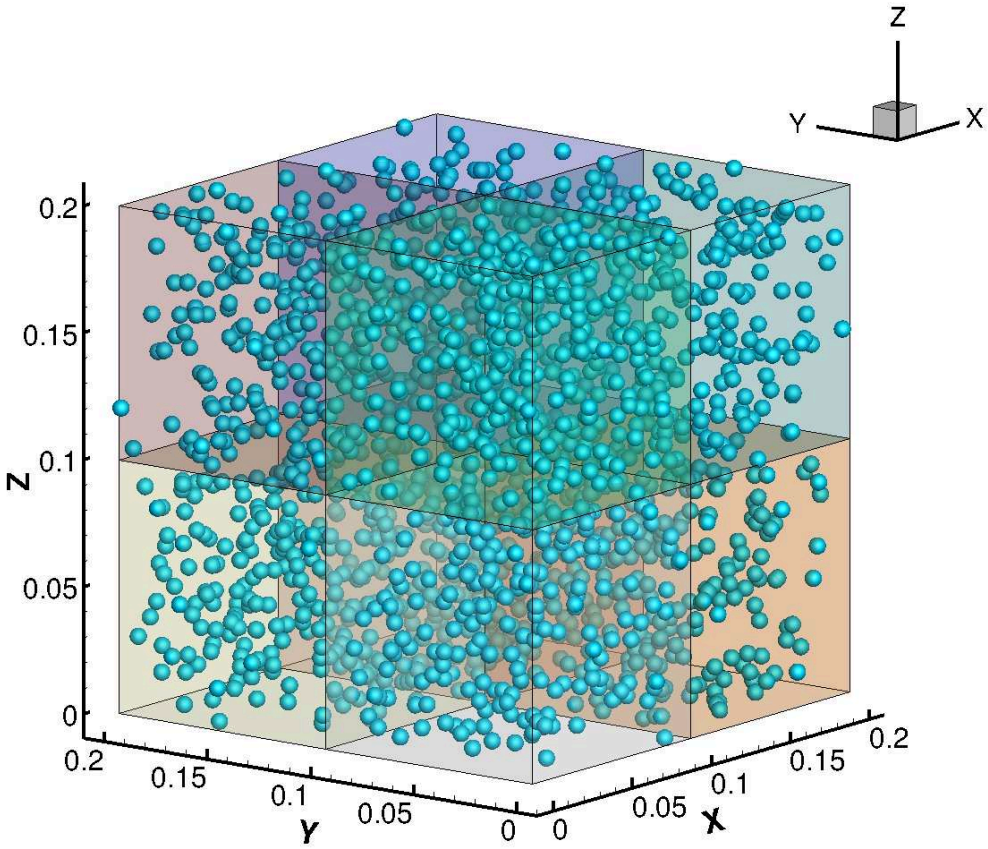

5.5 Cantera

Cantera is an open-source suite of software tools for problems involving chemical kinetics, thermodynamics and transport processes, and it can be used from Python and Matlab, or in applications written in C/C++ and Fortran 90 (GOODWIN; MOFFAT; SPETH, 2016). Currently, this tool is widely used for evaporation and combustion applications.

In the present work, the Cantera C++ routine library is used to compute the physical properties of the gaseous substances, given their temperature, pressure and chemical composition. More specifically, the physical properties for vapor and gas, identified with subscripts v and g in Chapter 3, as well as diffusivity of vapor in the ambient gas, D_{vm}, are obtained utilizing Cantera based on the gas-vapor mixture reference state.

Cantera estimates the thermodynamic and transport properties based on the kinetic gas theory and NASA database. This database is provided by means of a .cti input file from Cai

et al. (2016). For more information on how Cantera estimates those properties, Sanjosé (2009) exposes the formulas used to compute each one of them.

In MFSim code, a single header file, props_calculator.h, is included at the beginning of the the C file where the evaporation module from Fig. 5.2 was implemented. All Cantera functions used are called in a separate file, props_calculator.cpp, used exclusively for this purpose. This modular approach was chosen so the same structure can be used for future implementations out of the Lagrangian solver. Both props_calculator C++ and header files are presented in Appendix A.

5.6 Fortran/C/C++ languages linking

The entire Lagrangian data structure, which is presented in Section 5.3, is implemented in C language. In order to integrate the Lagrangian module with the base structure of MFSim code and the Eulerian module, which are implemented in Fortran language, there is interface between the operational languages for each function implemented in C. The general logical structure of this interface, performed by a Fortran wrapper file using the iso_c_bindig module, is:

```
1  interface
2    subroutine ex_name (vector_double , var_double , vector_int , var_int)bind(c,
         name ="ex_name")
3      use iso_c_binding
4      implicit none
5
6      real(c_double), dimension (*) :: vector_double
7      real(c_double) :: var_double
8      integer(c_int), dimension (*) :: vector_int
9      integer(c_int) :: var_int
10   end subroutine ex_name
11 end interface
```

Moreover, since Cantera C++ routine library is used, C and C++ languages should also be integrated. But this type of language integration is easier, only needing the following code to be included in the beginning of the C++ file, ex_name.cpp. Then, the header file ex_name.h can

be included in C files normally.

```
1 extern "C"{
2 #include "ex_name.h"
3 }
```

CHAPTER VI

RESULTS AND DISCUSSION

In the present chapter the authors present results and discussions on the numerical simulations performed. It is valid to highlight that evaporation models verification and validation as well as the several investigations conducted were performed using the Python code. Only the last section presents results from simulations performed with the MFSim computational platform. More specifically, this chapter is organized as follows.

In Section 6.1, the Abramzon-Sirignano model implementation is verified by comparing the simulations results obtained with first-order Euler and fourth-order Runge-Kutta methods against the Abramzon and Sirignano (1989) results. The three evaporation models described in Section 3.2, i.e. CEM, NEQ and ASM, are validated with experimental data available in literature for a low evaporation rate case with water droplet evaporation and then, with moderate and high evaporation rates cases for n-heptane droplet evaporation in Section 6.2. In Section 6.3, an in-depth investigation into the differences between CEM and NEQ formulation is carried out. In Sections 6.4 and 6.5 natural and forced convection effects incorporation is evaluated. After, the effects of ambient pressure and gas temperature on the evaporation of a single ethanol droplet is examined in Section 6.6.

Finally, Section 6.7 presents the simulations performed with the MFSim computational framework. First, one of the test cases used for models validation is employed to compare Python and MFSim predictions. Further on, a vortex flow is simulated to verify the evaporation module parallelization.

6.1 Abramzon-Sirignano model verification

When Abramzon and Sirignano (1989) first proposed ASM, they have presented a test case of n-decane droplet with initial diameter $D_{do} = 100$ μm and temperature $T_{do} = 300$ K evaporating in air at $T_g = 1500$ K and $p_g = 1.0$ MPa. The droplet with initial velocity $u_{do} = 15$ m/s is in a quiescent air environment. In order to verify the implementation of this evaporation model, the numerical results obtained by the present research where compared against those available in Abramzon and Sirignano (1989). Initially, the first-order Euler method was employed for time integration; however, since a considerable discrepancy between the evaporation rate predictions was observed (see Fig. 6.1), the fourth-order Runge-Kutta method was implemented and a new simulation was performed.

The temporal evolution of three droplet parameters, i.e. evaporation rate, non-dimensional diameter and temperature, are shown in Figs 6.1, 6.2 and 6.3, respectively. As it can be noticed in those figures, there is a good agreement between the fourth-order Runge-Kutta results and those presented by Abramzon and Sirignano (1989) for all the parameters analyzed.

Figure 6.1: Droplet evaporation rate temporal evolution.

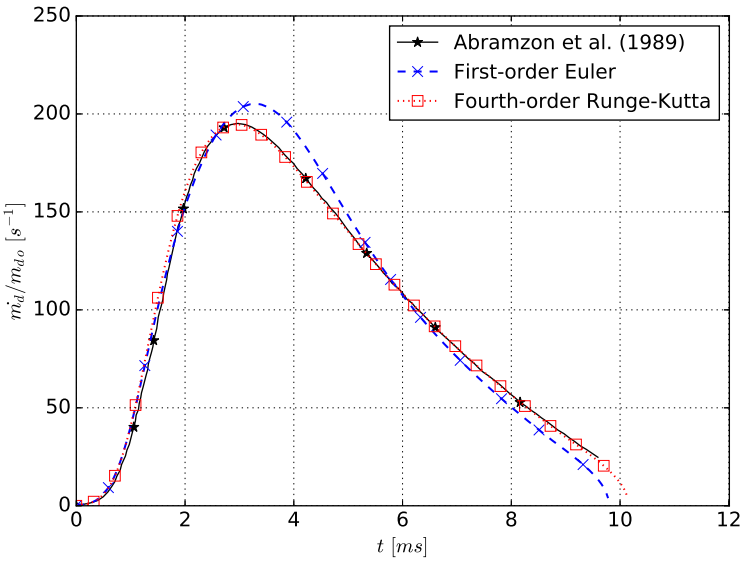

In Fig. 6.1 the most outstanding differences between the two time integration methods are found when the evaporation rate reaches its maximum value and at the end of the simulation. For $t = 4$ ms and $t = 9.6$ ms, the relative percentage difference between the first-order Euler and the Abramzon and Sirignano (1989) predictions is approximately 10% higher and 44% lower,

respectively; while for the fourth-order Runge-Kutta it is approximately 1% lower and 8% smaller, respectively. In Fig. 6.2 the maximum difference is found at the end of the simulation for both methods; however, while the fourth-order Runge-Kutta presents a difference of about 12%, the first-order Euler presents a difference of about 49%. In Fig. 6.3 both methods presented droplet temperature predictions approximately 1% higher than the Abramzon and Sirignano (1989) results throughout the simulation.

Figure 6.2: Non-dimensional droplet diameter temporal evolution.

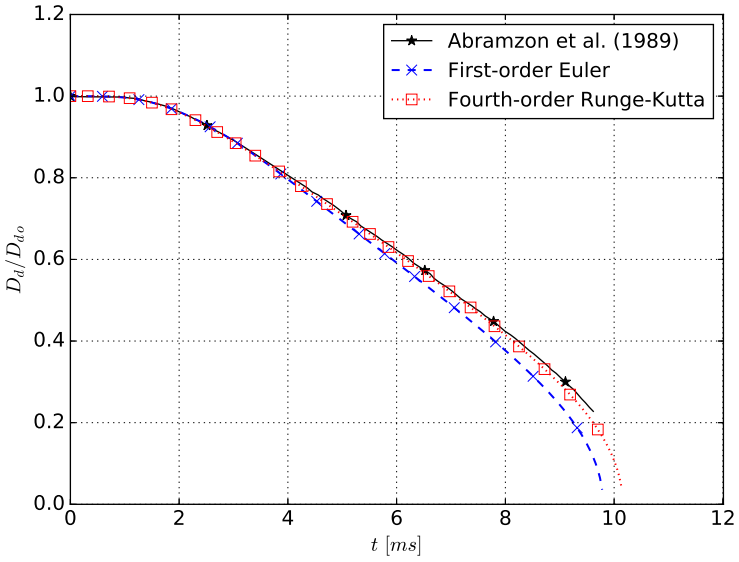

Figure 6.3: Droplet temperature temporal evolution.

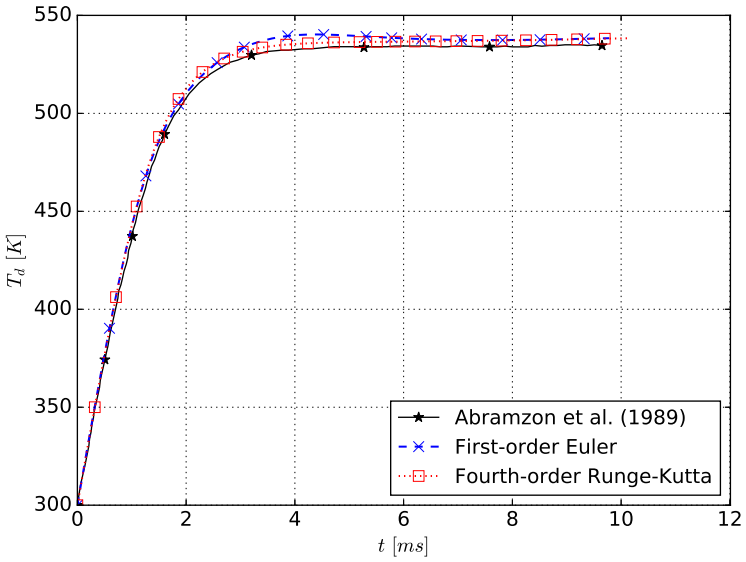

Therefore, considering the divergence between the predictions of the two time integration methods evaluated, from now on only the fourth-order Runge-Kutta will be employed. The

difference between the fourth-order Runge-Kutta results and those presented by Abramzon and Sirignano (1989) may have been caused by: (i) the vapor density, ρ_v, computation, because this physical property computation is the only one not given in Abramzon and Sirignano (1989); (ii) the inherent error in data acquisition by digitizing software for converting graphs into numbers.

6.2 Evaporation models validation

The primary purpose of this section is to analyze the evaporation characteristics of liquid droplets using the most consolidated evaporation models presented in literature for practical applications, taking into account the majority of the key processes involved. A comparative study is made on the performance of three different models: classical evaporation model (CEM), Abramzon-Sirignano model (ASM) and non-equilibrium model (NEQ). Even though those models are among the eight ones already evaluated by Miller, Harstad and Bellan (1998), some discrepancies are observed between conclusions.

The mathematical model described in Section 3.2 is validated by comparing each evaporation model prediction with experimental measurements. In order to evaluate the predictions of these evaporation models, first, a low evaporation rate case with water droplet is simulated and then, moderate and high evaporation rates cases for n-heptane are simulated. For the n-heptane cases, recent experimental data obtained with the cross-fiber technique are used for comparison.

6.2.1 Water droplet with low evaporation rate

Ranz and Marshall (1952b) experiment was performed for a water droplet with initial temperature and diameter equal to 282 K and 1.049 mm, respectively. The ambient conditions are atmospheric pressure and air temperature equals 298 K. Although this experiment was not performed using the cross-fiber technique, considering the small difference between droplet and ambient gas temperature, radiation absorption and fiber conduction are minimized.

The comparison of the droplet diameter evolution obtained with the numerical simulations and the experiment is shown in Fig. 6.4. For this case low evaporation rate, all of the tested models predict nearly identical evaporation behavior and they agree with the experimental data, as demonstrated. From the information presented in Fig. 6.4, the area reduction rate, K, can be

estimated as 0.0014 mm^2/s for the experiment, 0.0012 mm^2/s for CEM and NEQ, and 0.0011 mm^2/s for ASM. The area reduction rate measured in the experiment might be higher than the ones calculated from the simulation results due to the extra energy from fiber conduction, since the experiment was performed using the single fiber technique.

Figure 6.4: Temporal variation of normalized squared droplet diameter for water.

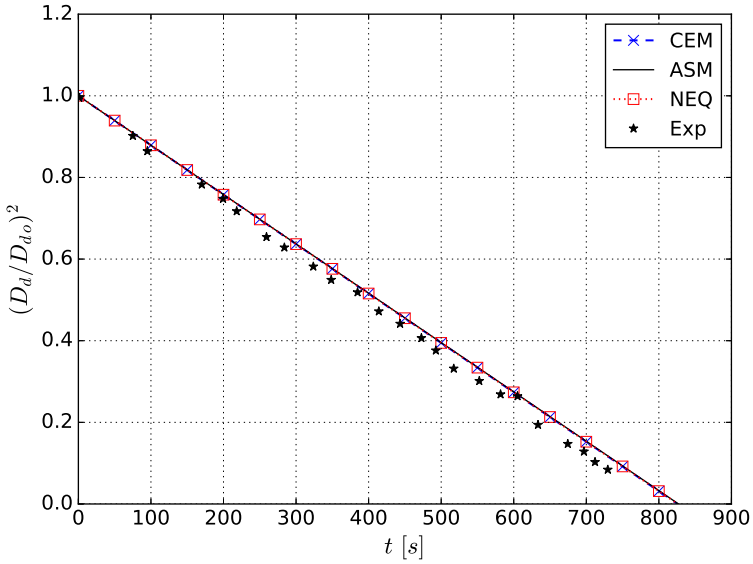

In addition, the droplet temperature temporal evolution, which is presented in Fig. 6.5, is very similar for all the tested models. Because of the low ambient gas temperature, the droplet actually cools down due to evaporation and, then, achieves a steady-state temperature. This same temperature behavior was also observed by Sacomano-Filho (2017), even though it differs from Miller, Harstad and Bellan (1998) results.

Water boiling temperature is 373.15 K; therefore, the ambient gas temperature is in fact lower than it. For cases in which the gas temperature much lower than the liquid boiling temperature, the evaporation rates are small, implying in nearly identical evaporation behavior for all models.

6.2.2 N-heptane droplet with moderate to high evaporation rate

Chauveau *et al.* (2008) experiments for n-heptane droplet were performed in a furnace with nitrogen as the ambient gas to prevent oxidation. The fuel droplets with initial temperature and diameter around 300 K and 500 μm, respectively, were supported in a cross-fiber system. In all experiments the ambient pressure was kept atmospheric and under normal gravity condition,

Figure 6.5: Temporal variation of droplet temperature for water.

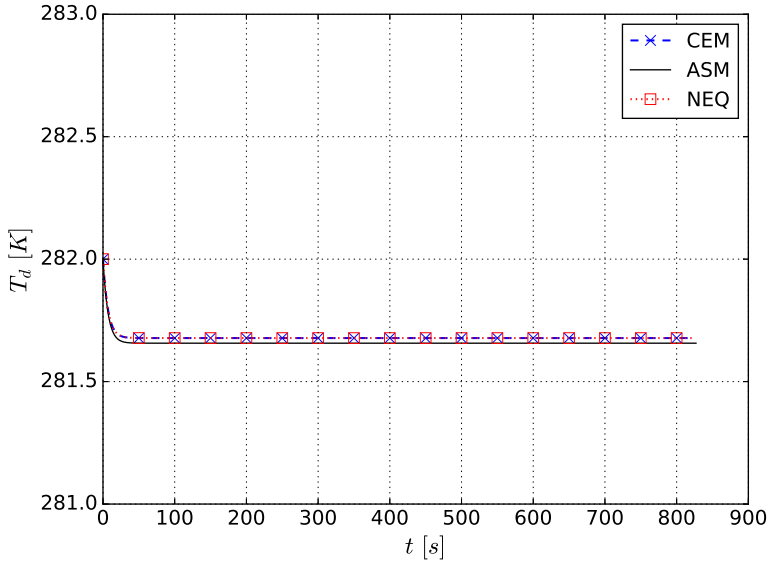

while the temperature varied from 473 to 748 K.

The authors show in Fig. 6.6 comparisons of the droplet size histories obtained with the three evaporation models presented here and the experimental data for a range of ambient gas temperature above mentioned. It can be observed that the numerical results are in good agreement with the measurements for the whole range of temperature studied.

In Figure 6.7, on the other hand, the authors present droplet temperature evolution and the wet-bulb temperature, T_{wb}, for each case, which was estimated based on Yuen and Chen (1976) experimental data. It can be observed that the ASM predicts a lower temperature when compared to the other two, and it also tends to the wet-bulb temperature when it reaches the plateau region, as expected, for the majority of the cases tested. This behavior explains why the ASM model predicts lower evaporation rate and, consequently, higher droplet lifetime. One should note that differences between each model predictions are only evident for the n-heptane simulations because ambient gas temperature is higher than the liquid boiling temperature, 371.6 K, resulting in moderate to high evaporation rate.

The differences observed in Figs. 6.6 and 6.7 between the ASM and CEM/NEQ performance are caused exclusively by the distinct correct factor, G, incorporated in each model, since the droplet Reynolds number is zero for all the cases. Analyzing the Spalding transfer numbers, B_M and B_T, may help one to better understand why their predictions differ. In Table 6.1, the authors present the B-values when the evaporation reached the steady-state condition for ambient

Figure 6.6: Variations of normalized squared droplet diameter with the time divided by squared initial droplet diameter for n-heptane.

(a) $T_g = 473$ K

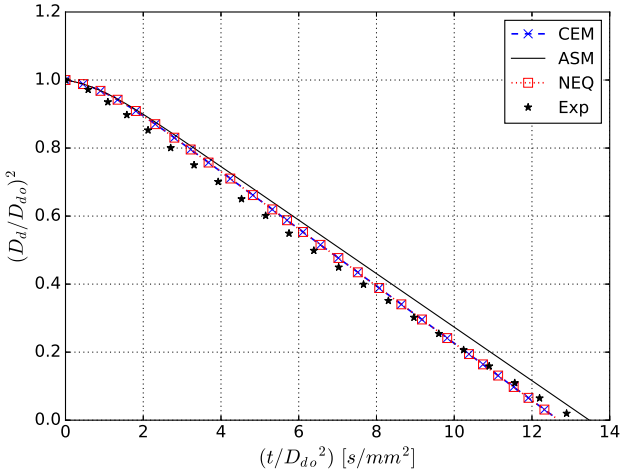

(b) $T_g = 548$ K

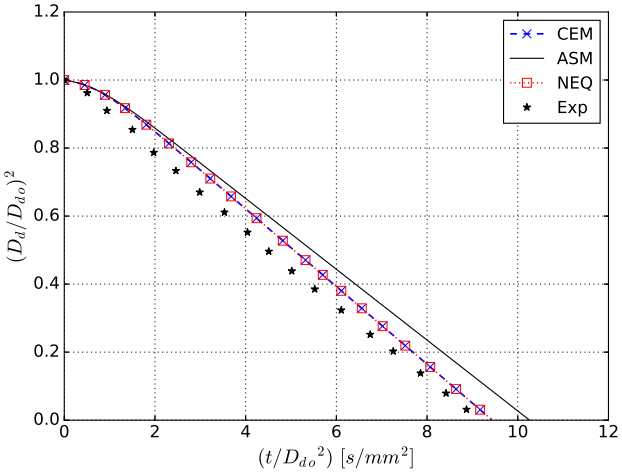

(c) $T_g = 623$ K

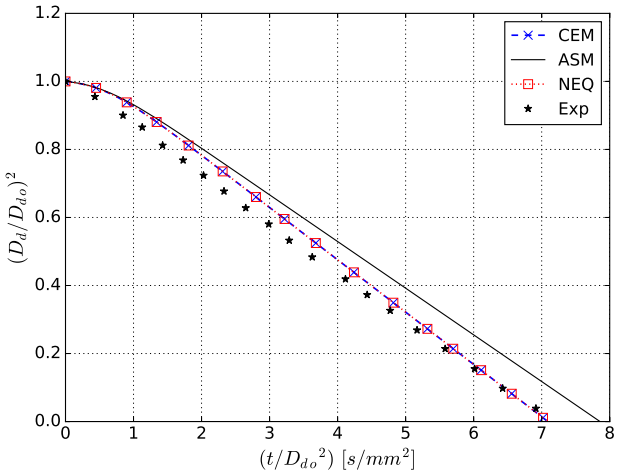

(d) $T_g = 748$ K

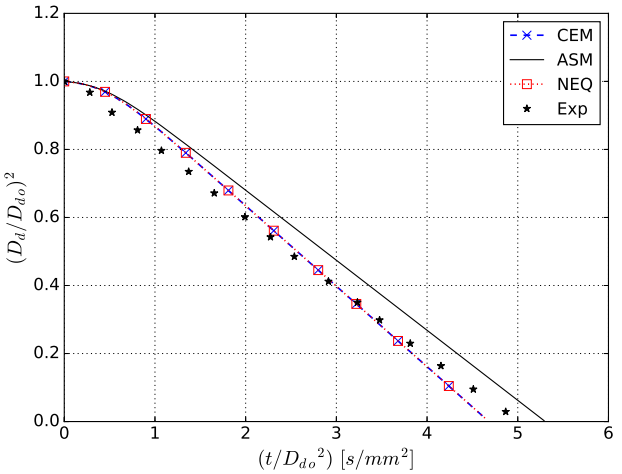

gas temperature equals to 473 and 748 K. As follows from this table, the B-values predicted by the ASM are always lower than those predicted by the other models, implying in lower evaporation rate and lower thermal energy transfer between droplet and gas.

Table 6.1: B-values for n-heptane numerical simulations

	$T_g = 473$ K		$T_g = 748$ K	
Parameter	CEM/NEQ	ASM	CEM/NEQ	ASM
B_T	0.95	0.85	3.87	2.95
B_M	1.07	1.00	3.29	2.71

After the initial heat-up period, the well-known D^2 law is obeyed, which means that the

Figure 6.7: Variations of droplet temperature with the time divided by squared initial droplet diameter for n-heptane.

(a) $T_g = 473$ K; $T_{wb} = 320$ K

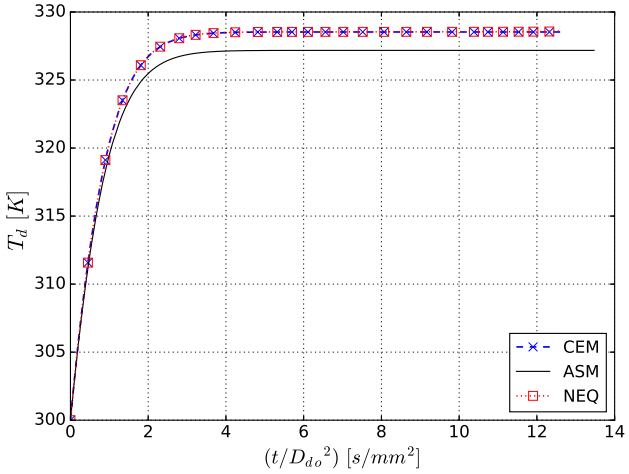

(b) $T_g = 548$ K; $T_{wb} = 329$ K

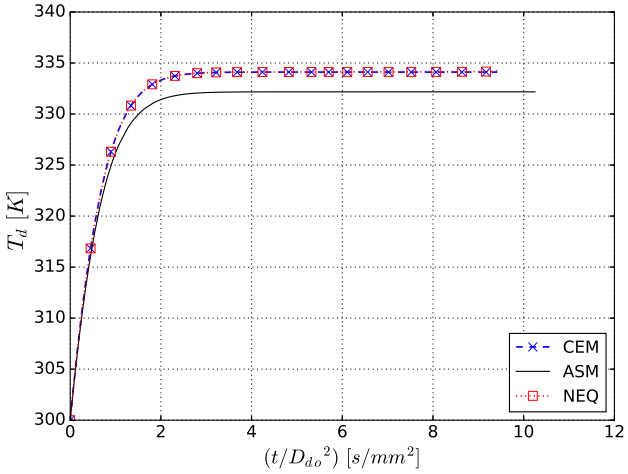

(c) $T_g = 623$ K; $T_{wb} = 337$ K

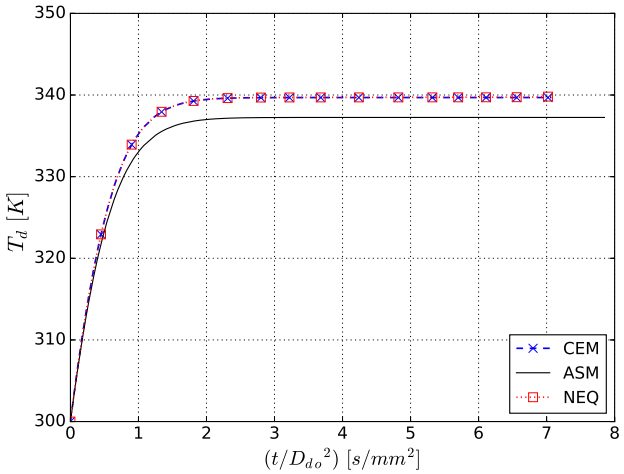

(d) $T_g = 748$ K; $T_{wb} = 348$ K

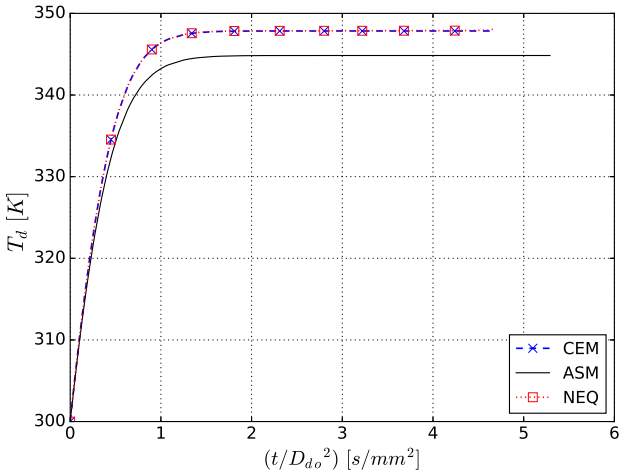

droplet surface area varies linearly with time. Therefore, the area reduction rate, K, can be estimated as the negative slope of the variation of the squared droplet diameter in the steady-state evaporation period. The best-fit straight line was calculated using the least square regression. This procedure was used for both numerical and experimental data analysis.

In Figure 6.8, the authors present the area reduction rate calculated from the numerical and experimental data presented in Fig. 6.6. The predictions obtained with CEM and NEQ are, in average, 5.91% higher than the experimental, while the ASM is 4.54% lower. There are several effects that could increase the experimental evaporation rates compared to theoretical model predictions; however, it is very difficult to justify the opposite. Radiation absorption and fiber

conduction were already mentioned in Section 1.2 as factors that could increase the experimental evaporation rates. Additionally, natural and forced convection effects could also increase them, i.e., when the experiment is performed under normal gravity condition or the ambient gas is not quiescent.

Figure 6.8: Comparison of the area evaporation rate, according to the ambient temperature, for various models and experimental measurements for n-heptane.

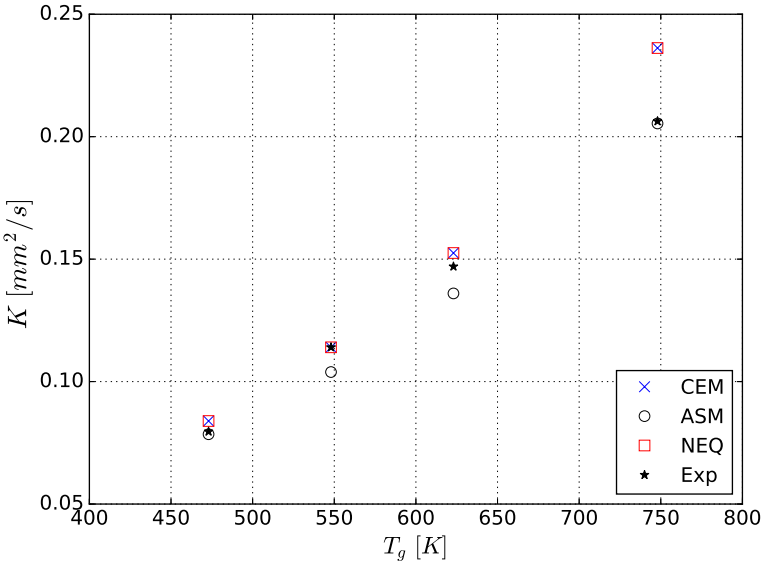

The ASM is the only model that does not overestimate the evaporation rate for any of the tested cases, which indicates that this model derivation might have more physical coherence or less restrictive assumptions. Since natural convection effects indeed increase the evaporation rate, only the ASM is used in the investigation of these effects. It is worth mentioning that even though ASM requires an iterative procedure to find the converged value of B_T, for practical industrial applications involving evaporation and combustion processes, as the one presented in Sánchez (2012), only a few number of iterations are required to reach the convergence, typically five iterations.

Moreover, the deviation between the ASM prediction and the experimental results might be justified by the uncertainty factors associated to the experimental data: (i) the calculation error in determining the droplet diameter, which is of the order of $\pm$ 3%; (ii) the droplet initial temperature is not clearly stated in Chauveau *et al.* (2008); (iii) although the effect of energy transfer from the fiber to the droplet through conduction is significantly minimized by the use of the cross-fiber technique, it might still have some extra energy transfer occurring; (iv) no

particular treatment was used to prevent radiation, as the one presented in Ghassemi, Baek and Khan (2006).

Miller, Harstad and Bellan (1998) suggested that the NEQ achieved better predictions than the other models. However, in investigations conducted in their research, the ASM predictions reached a steady-state droplet temperature that seems to be exceptionally low. A possible justification for this puzzling behavior is that their ASM formulation apparently switches c_{p_v} for c_{p_g}, when compared with the formulation presented in Abramzon and Sirignano (1989). They have also mainly contrasted CEM*[1], ASM and NEQ performances, while the only test in which CEM was actually considered, they applied $\alpha_w = 1$ to determine the gas-vapor mixture properties for NEQ, and $\alpha_w = 1/3$ for CEM. Thus, an in depth inspection of the differences between CEM and NEQ is required applying $\alpha_w = 1/3$ for all the simulations.

Furthermore, they noticed that thermodynamic non-equilibrium effects are only relevant when the initial droplet diameter is smaller than 50 μm. Hence, the next section is dedicated to investigate the real contribution of considering the Langmuir-Knudsen correction together with the Clausius-Clapeyron law, as showed in Eq. 3.28. The examination is conducted for droplets with different initial diameter, from 500 to 10 μm to stress NEQ as much as possible.

6.3 NEQ: Langmuir-Knudsen law versus Evaporation correction factor

The only difference between CEM and NEQ formulations is the approach used to determine the vapor molar fraction at the droplet surface. While the former assumes that the vapor concentration is always at saturated condition, the latter believe that non-equilibrium effects should be considered by introducing the Langmuir-Knudsen law as a deviation term. Therefore, this section aims to examine the improvement achieved by including this deviation term.

Chrigui *et al.* (2012) explains in details how including those non-equilibrium effects on droplet evaporation impacts NEQ performance in comparison with CEM. They affirmed that the deviation factor placed in the vapor molar fraction equation, given by the product of the non-dimensional evaporation parameter and the Knudsen thickness normalized by the droplet radius, decreases the surface vapor molar fraction, and, as a consequence, the surface vapor mass fraction

[1] The original model without the reduction coefficient is usually called classical rapid mixing model in literature and it is referred here as CEM*, as explained in Subsection 3.2.1.

and the Spalding mass transfer number are also reduced.

Figure 6.9 shows that the behavior described by Chrigui *et al.* (2012) is actually observed in NEQ predictions. However, this NEQ improvement is not noticed in comparison with CEM, but in reality in comparison with CEM*, suggesting that this tendency is indeed a consequence of incorporating the correction factor, G, for energy transfer reduction due to evaporation, since CEM and NEQ showed exactly alike predictions. In addition, vapor molar fraction, vapor mass fraction and Spalding mass transfer number reduction previously mentioned is also observed by contrasting the predictions from CEM and CEM*.

Figure 6.9: Temporal evolution of some evaporation parameters for equilibrium and non-equilibrium conditions with $T_g = 748$ K and $p_g = 0.1$ MPa for n-heptane.

(a) Vapor molar fraction at the surface

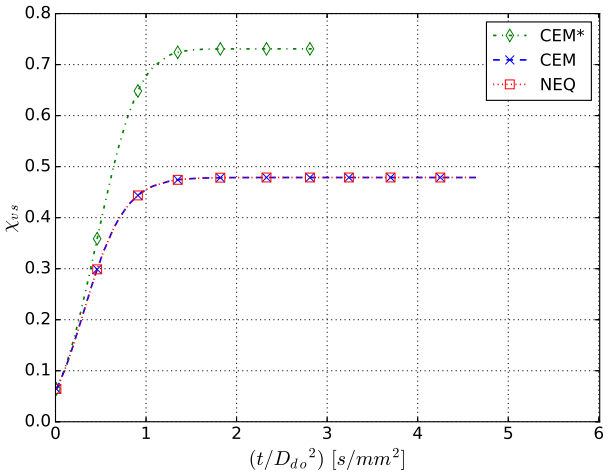

(b) Vapor mass fraction at the surface

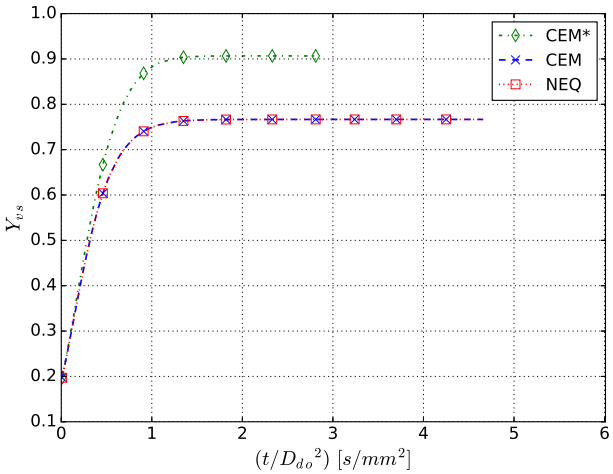

(c) Spalding mass transfer number

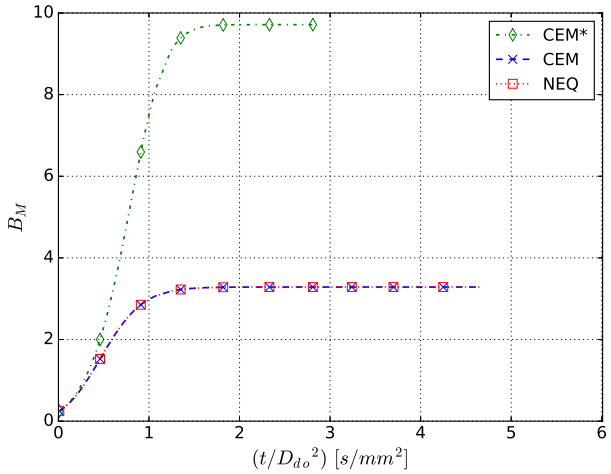

Miller, Harstad and Bellan (1998) have also warned that the smaller the droplet is, the

higher is the contribution of non-equilibrium effects, expressively increasing at the end of the droplet lifetime. This issue is checked in Fig. 6.10(a), which shows the percentage relative non-equilibrium contribution from the term $2L_K\beta/D_d$ to the surface molar fraction, $\chi_{v_s}^{neq}$, with the y axis in log-scale. As this figure clearly demonstrates, the behavior described by Miller, Harstad and Bellan (1998) undoubtedly happens. For an initial 10 μm diameter droplet the non-equilibrium contribution reaches up to 70% for n-heptane evaporation under atmospheric pressure and $T_g =$ 748 K.

In Figure 6.10(b), on the other hand, the authors show the percentile ratio between $\chi_{v_s}^{eq}$, calculated by Eq. 3.15, and $\chi_{v_s}^{neq}$, calculated by Eq. 3.28. This figure shows that the smaller the droplet is, the higher is the ratio between $\chi_{v_s}^{eq}$ and $\chi_{v_s}^{neq}$, growing as the droplet evaporates. Thus, even though $2L_K\beta/D_d$ increases, $\chi_{v_s}^{eq}$ also increases with the same intensity. As $\chi_{v_s}^{neq}$ is the difference between these two terms, no truly improvement is achieved by introducing the Langmuir-Knudsen law, not even for small droplets. For an initial 10 μm diameter droplet, for instance, the percentile ratio between $\chi_{v_s}^{eq}$ and $\chi_{v_s}^{neq}$ reaches up to 170% for n-heptane evaporation under atmospheric pressure and $T_g =$ 748 K, canceling the non-equilibrium contribution.

Figure 6.10: Temporal evolution of (a) the non-equilibrium contribution and (b) the ration between equilibrium and non-equilibrium vapor molar fraction for various initial droplet diameters with $T_g = 748$ K and $p_g = 0.1$ MPa for n-heptane.

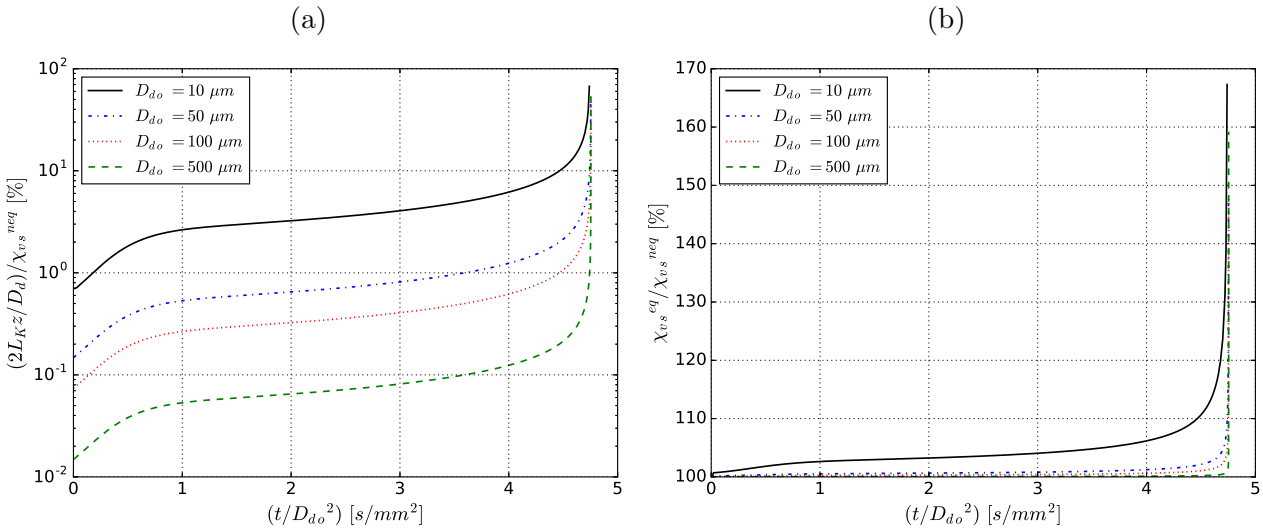

As a consequence, it can be observed from Fig. 6.11 that even for small initial droplet diameter the vapor mass fraction temporal evolution predicted with or without incorporating non-equilibrium effects is equal. Therefore, to the best understanding of the authors, the addition

of non-equilibrium effects has not presented any effect on n-heptane droplet evaporation, even in different gas temperatures. Such effects might be more prominent in the evaporation of multicomponent fuels or temperatures above the one evaluated in the present research. In either way, those conditions are not in the scope of the present work and may be object of further investigations.

Figure 6.11: Temporal evolution of the surface vapor mass fraction for various initial droplet diameters with $T_g = 748$ K and $p_g = 0.1$ MPa for n-heptane.

(a) $D_{do} = 500$ μm

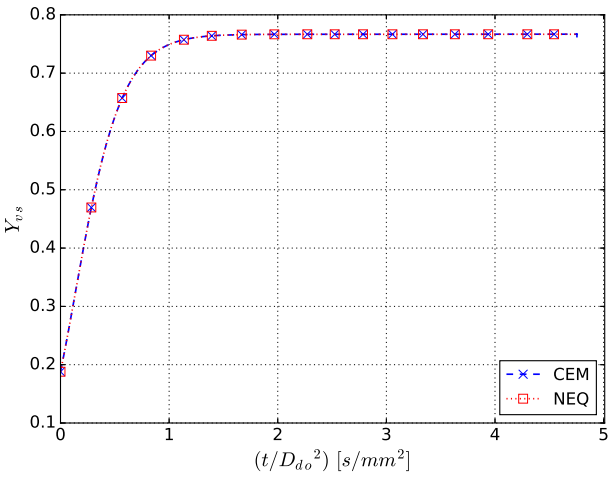

(b) $D_{do} = 100$ μm

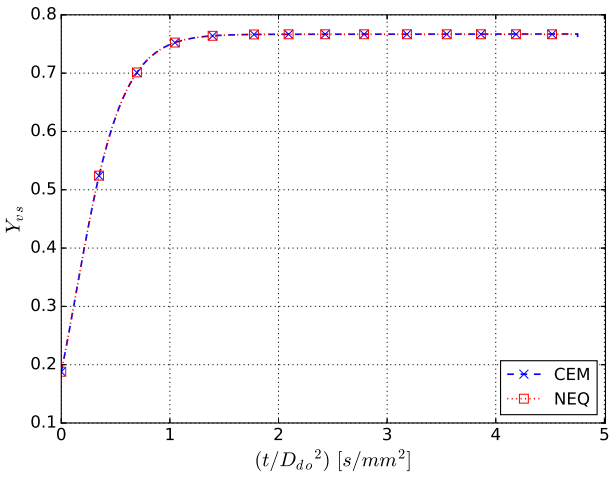

(c) $D_{do} = 50$ μm

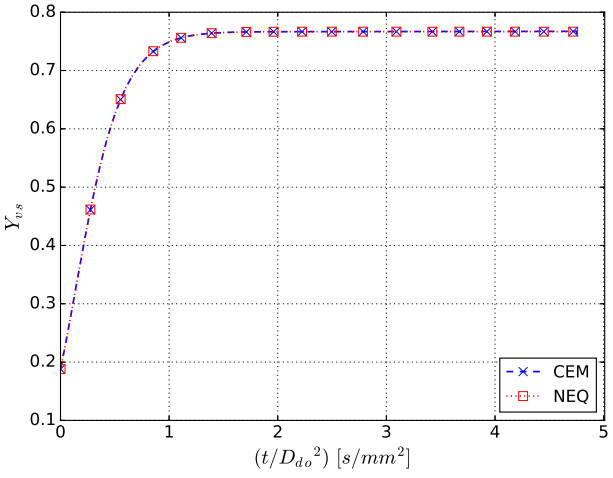

(d) $D_{do} = 10$ μm

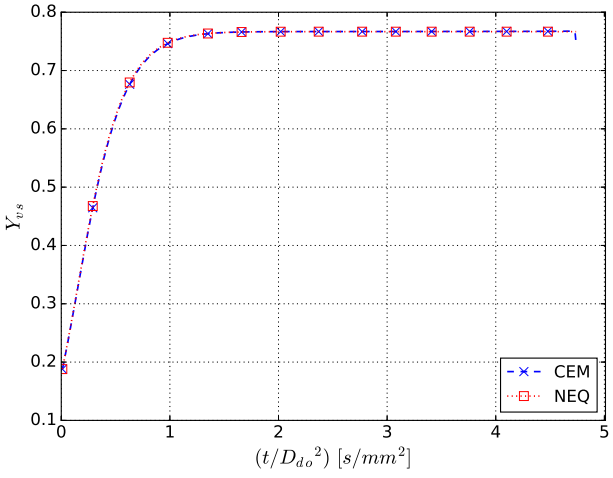

6.4 Natural convection effects

Droplet evaporation under normal gravity condition is affected by natural convection. This phenomenon enhances energy and mass transfers between the evaporating droplet and the sur-

rounding gas. Hence, depending on the ambient conditions, incorporating these effects might become essential to correctly predict droplet evaporation rate.

Some experimental investigations have already been done to study the role of natural convection on droplet evaporation, such as Nomura *et al.* (1992) and Verwey and Birouk (2018). Kitano *et al.* (2014) have shown the need of considering natural convection effects even if the evaporation occurs under microgravity conditions. However, none of those studies have analyzed the effect of introducing the Grashof number in the expressions of the Sherwood and Nusselt numbers by means of empirical correlations, which is the procedure usually used in numerical simulations. Hence, it is necessary to investigate if this method can accurately represent the natural convection contribution.

Since the experiment presented in Chauveau *et al.* (2008) was performed under normal gravity condition, the Grashof number was incorporated in Nusselt and Sherwood calculation to take into account this effect. The evaluation of such non-dimensional numbers is given by Yuge (1960):

$$Nu = 2 + 0.6\left[max\left({Gr_d}^{1/2}, Re_d\right)\right]^{1/2} {Pr_m}^{1/3}, \tag{6.1}$$

$$Sh = 2 + 0.6\left[max\left({Gr_d}^{1/2}, Re_d\right)\right]^{1/2} {Sc_m}^{1/3}, \tag{6.2}$$

in which the droplet Grashof number, Gr_d, which is defined by Ebrahimian, Nicolle and Habchi (2012) as:

$$Gr_d = \frac{g{\rho_g}^2 \left(T_g - T_d\right) {D_d}^3}{T_g {\mu_m}^2}. \tag{6.3}$$

In Figure 6.12, the authors present the squared non-dimensional diameter temporal evolution for numerical simulations performed with the Abramzon-Sirignano model without accounting for natural convection effects (ASM) and incorporating them (ASM*). As follows from comparing ASM and ASM* predictions, for all the tested ambient temperatures, incorporation of natural convection effects reduced the droplet lifetime, as expected. However, ASM* showed shorter

droplet lifetime than the one measured in the experiment.

Figure 6.12: Variations of normalized squared droplet diameter with the time divided by squared initial droplet diameter, with and without taking natural convection effects into account for n-heptane.

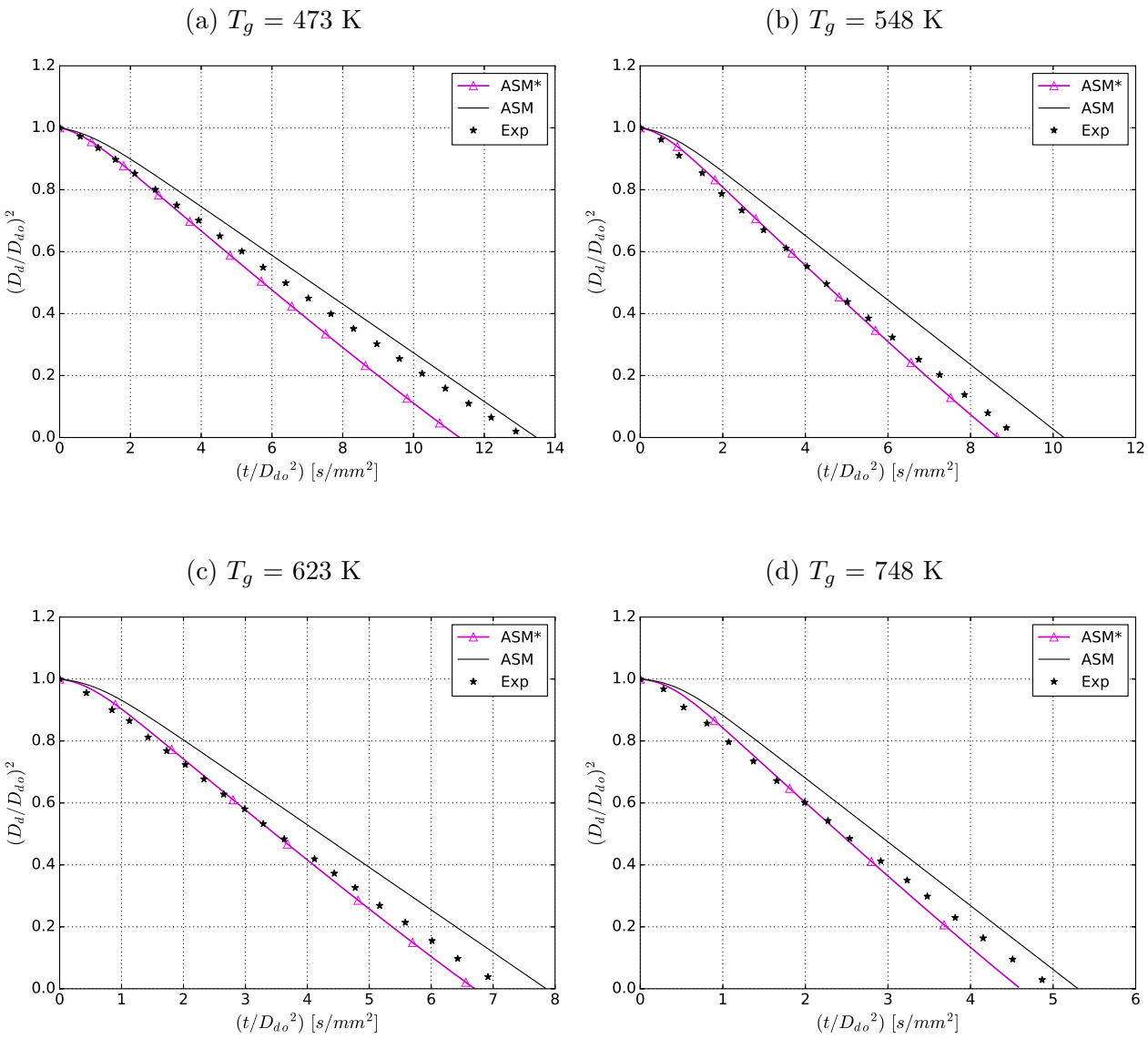

It can be verified from Fig. 6.13 and Eq. 6.3 that the droplet Grashof number decreases as the ambient temperature increases and it also decreases as the droplet diameter reduces. Figure 6.12 suggests that as the droplet diameter decreases, the validity of the empirical law to represent the natural convection effects may fail, since for all the tested cases ASM* predictions presented a noticeable agreement with experimental data in the beginning and then they diverge. It can be noticed that the ASM* predictions for intermediate ambient temperatures, 548 and 623 K, presented better agreement with experimental data, indicating that there might exist a droplet

Grashof number range in which the empirical correlation used in the present research fits better.

Figure 6.13: Temporal evolutions of droplet Grashof number for the ASM* predictions presented in Fig. 6.12 for n-heptane.

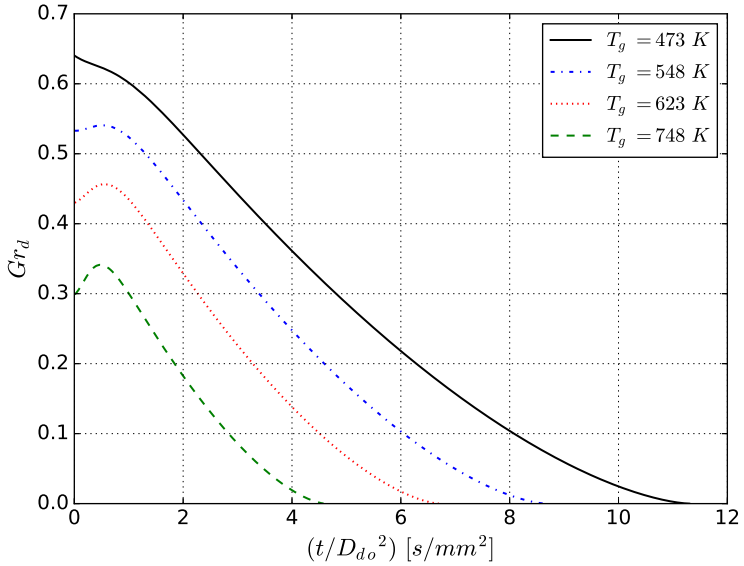

The area evaporation rate calculated from the data presented in Fig. 6.12 is displayed in Fig. 6.14. As it can be observed from Fig. 6.14, introducing natural convection effects by means of the empirical correlations presented in Eqs. 6.1 and 6.2 overestimates the evaporation rate obtained by the numerical simulations in comparison to the one measured experimentally for all the temperatures tested.

Figure 6.14: Comparison of the area evaporation rate, according to the ambient temperature, with and without taking natural convection effects into account for n-heptane.

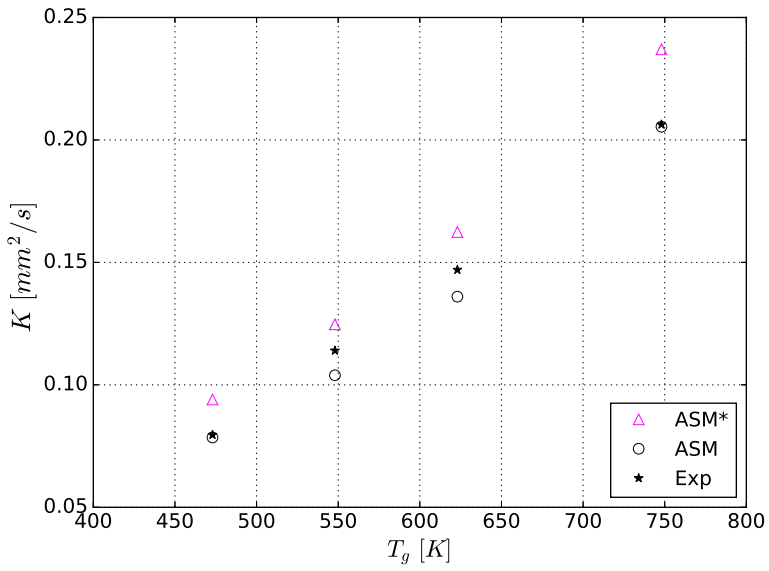

It is important to highlight that there might have several effects that could increase the

experimental evaporation rate, as the ones already cited, but it is hardly arguable to find any external influence that could diminish it. Therefore, introducing natural convection effects in numerical simulations by Eqs. 6.1 and 6.2 might not correctly represent what really happens physically, at least not for the conditions evaluated in Fig. 6.12.

6.5 Forced convection effects

In this section, the previously described three models, CEM, ASM and NEQ, are evaluated for a case with forced convection. Wong and Lin (1992) present experimental data for a test case of n-decane droplet with initial diameter $D_{do} = 1.961$ mm and temperature $T_{do} = 315$ K evaporating in air at $T_g = 1000$ K and $p_g = 0.1$ MPa. The stationary droplet is in an air environment with $u_g = 1.0\ m/s$. In the experiment, the temperature of evaporating decane droplets was measured with a thermocouple.

In Figure 6.15, the authors show the normalized squared droplet diameter temporal evolution measured by Wong and Lin (1992) and predicted by each evaporation model. In Figure 6.16, the authors present the associated droplet temperature temporal evolution with the wet-bulb temperature for the case, $T_{wb} = 420$ K, which was taken from Wong and Lin (1992). As it can be noticed by those figures, the droplet equilibrium temperature reached in the experiment is higher than the ones simulated, resulting in an experimental droplet lifetime smaller than the ones simulated.

Figure 6.15: Temporal variation of normalized squared droplet diameter for n-decane.

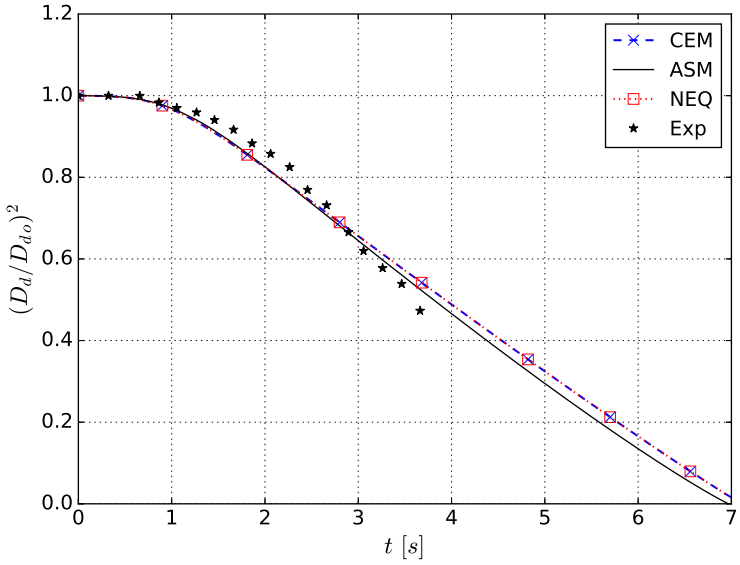

Figure 6.16: Temporal variation of droplet temperature for n-decane.

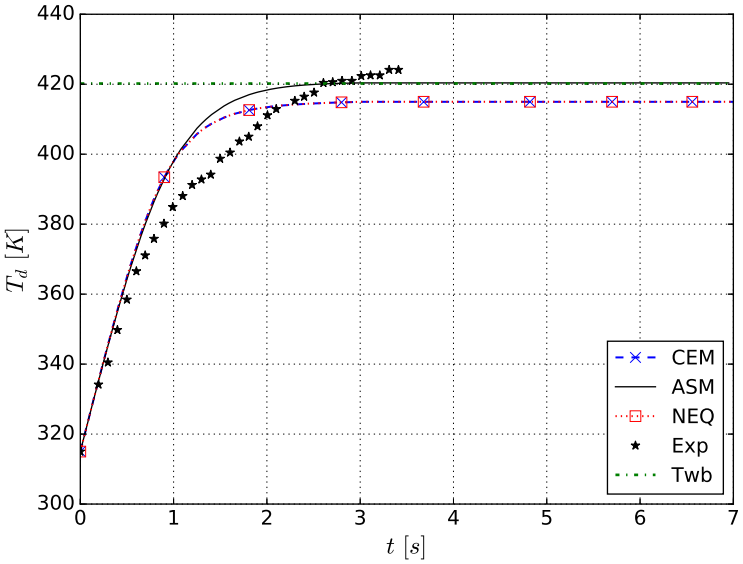

Since Wong and Lin (1992) experiment was performed using the classical single fiber technique, their results may have been influenced by the extra energy transfer from the fiber to the droplet through conduction. This extra energy transfer would increase the droplet equilibrium temperature and, as a consequence, decrease the droplet lifetime. With this extra energy transfer present, the droplet temperature would gradually increase instead of remaining at the wet-bulb temperature, as explained by Wong and Lin (1992).

In addition, comparing the results achieved by each one of the three evaporation models, it can be observed that ASM predicts a droplet lifetime slightly lower than the others and its droplet equilibrium temperature tends better to the wet-bulb temperature. Also, CEM and NEQ predictions do not present any difference. This observations imply that even when forced convection effects are accounted, the tendency found in Subsection 6.2.2 is maintained.

6.6 Ambient conditions effects on ethanol evaporation

Hallett and Beauchamp-Kiss (2010) presented experimental results for denatured alcohol droplet and asserted that pure ethanol results were almost identical. Their experiments were performed at atmospheric pressure, with gas temperature varying from 688 to 1023 K, and the classical single fiber technique was used. However, this technique actually increases the droplet evaporation rate significantly, since there is a energy transfer from the fiber to the droplet through conduction, as explained in Section 1.2.

Saharin *et al.* (2012), on the other hand, presented experimental results for anhydrous ethanol droplet using the cross-fiber technique. Their experiments were performed at atmospheric pressure, with gas temperature varying from 373 to 623 K, and the cross-fiber technique was used in order to avoid conduction effects.

Despite the fact that Hallett and Beauchamp-Kiss (2010) and Saharin *et al.* (2012) have studied the evaporation of an ethanol droplet, their results are limited to atmospheric pressure and low ambient temperature.

Therefore, the purpose of this section is to investigate the evaporation characteristics of a pure ethanol droplet at a wide range of ambient conditions used in certain practical situations by means of numerical simulations. The predictions of the evaporation model proposed by Abramzon and Sirignano were validated by comparison with experimental measurements obtained using the cross-fiber technique. Then, the ambient pressure and temperature were varied in the ranges of 0.1-2.0 MPa and 473-1973 K, respectively, to investigate the effects of ambient conditions on the droplet evaporation. Since ethanol critical temperature and pressure are 514 K and 6.14 MPa (GREEN; PERRY, 2007), all the simulations conditions are sub-critical.

6.6.1 Validation

The ASM predictions are compared with the experimental measurements of Saharin *et al.* (2012) for anhydrous ethanol droplets. The experiments were performed in a furnace with nitrogen as the ambient gas to prevent oxidation or ignition. The fuel droplets with initial diameter between 430 and 609 μm were supported in a cross-fiber system. In all experiments the ambient pressure was kept atmospheric and under normal gravity condition, while the temperature varied from 473 to 673 K.

In Figure 6.17, the authors show comparisons of the normalized squared droplet diameter temporal evolution obtained with the numerical simulations and the experimental data. This figure does not exhibit the droplet heat-up period for any ambient temperature due to limitations of the experimental procedure. Moreover, it is already known that after the initial heat-up period, the well-known D^2 law is obeyed, which means that the droplet surface area varies linearly with time. As a consequence, an average area evaporation rate, also known as an evaporation constant, K, can be estimated as the slope of the variation of the squared droplet diameter in the quasi-steady

evaporation period.

Figure 6.17: Variations of normalized squared droplet diameter with the time divided by squared initial droplet diameter.

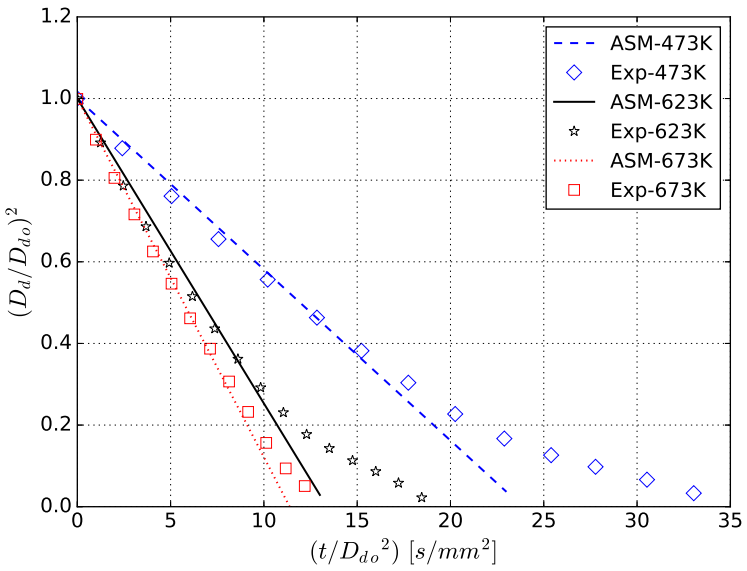

Experimental data presented in Fig. 6.17 exhibits a deviation from the linear D^2 as the droplet diameter decreases due to the interference of water vapor from the ambient in the anhydrous ethanol droplet evaporation, which is caused by the hygroscopic nature of this short carbon chain alcohol (SAHARIN *et al.*, 2012). In other words, as the droplet evaporates, the anhydrous ethanol is contaminated by water. However, this effect gradually decreases as the ambient temperature is increased. Therefore, considering only the initial curve slope that actually represents pure ethanol evaporation, it can be concluded that the numerical results are in good agreement with the measurements for the whole range of temperature studied.

In Figure 6.18, the authors present the average area evaporation rate from the experimental measurements, calculated from the data presented in Fig. 6.17, and two theoretical evaporation rates, $Th1$ and $Th2$, which are based on the binary diffusion coefficient, D_v, and on thermodynamic properties of the mixture, respectively. For 473 K, ASM evaporation rate is 2.29% lower than the experimental one. For higher temperatures, this relative percentage difference increases. While for 623 K the ASM evaporation rate is 5.50% lower than the experimental, for 673 K it is actually 7.28% higher. However, the ASM evaporation rates for the higher temperatures are placed between the theoretical values.

The deviation between the ASM predictions and the experimental results might be justified

Figure 6.18: Experimental, numerical and theoretical average area evaporation rates at various ambient temperatures.

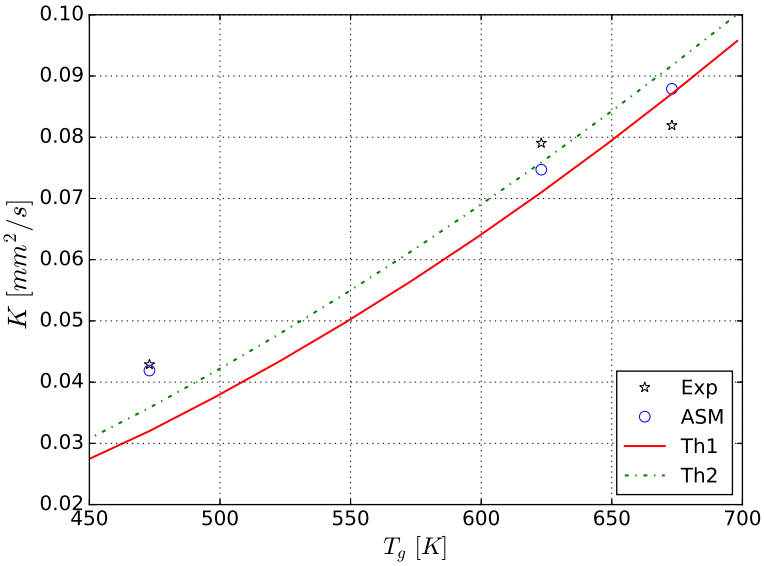

by the simplifications assumed in the mathematical model and uncertain factors associated to the experimental data, as the calculation error in determining the droplet diameter by analyzing images, which is of the order of $\pm$ 3%; the droplet initial temperature is not clear stated in Saharin *et al.* (2012); and, although the extra energy transfer is significantly minimized by the use of the cross-fiber technique, it might still have some extra energy transfer occurring by radiation from the furnace wall and by conduction from the fibers.

6.6.2 Effects of ambient pressure and temperature

It is already known from experimental and numerical investigations that the ambient temperature affects the way the evaporation rate of pure fuel droplets varies with ambient pressure (NOMURA *et al.*, 1996; KIM; SUNG, 2003). These two parameters, temperature and pressure, should be analyzed together in order to determine the evaporation characteristics of a certain fuel droplet.

The temporal variation of normalized squared droplet diameter at several ambient pressures for low and high temperature are shown in Figs. 6.19 and 6.20, respectively; while the associated temporal variation of droplet temperature are shown in Figs. 6.21 and 6.22. The results reveal that for both, low and high ambient temperatures, the increase of the ambient pressure causes an augmentation in the ratio between the initial heat-up time and the total droplet evaporation

Figure 6.19: Variations of normalized squared droplet diameter with the time divided by squared initial droplet diameter at low temperature and various ambient pressures.

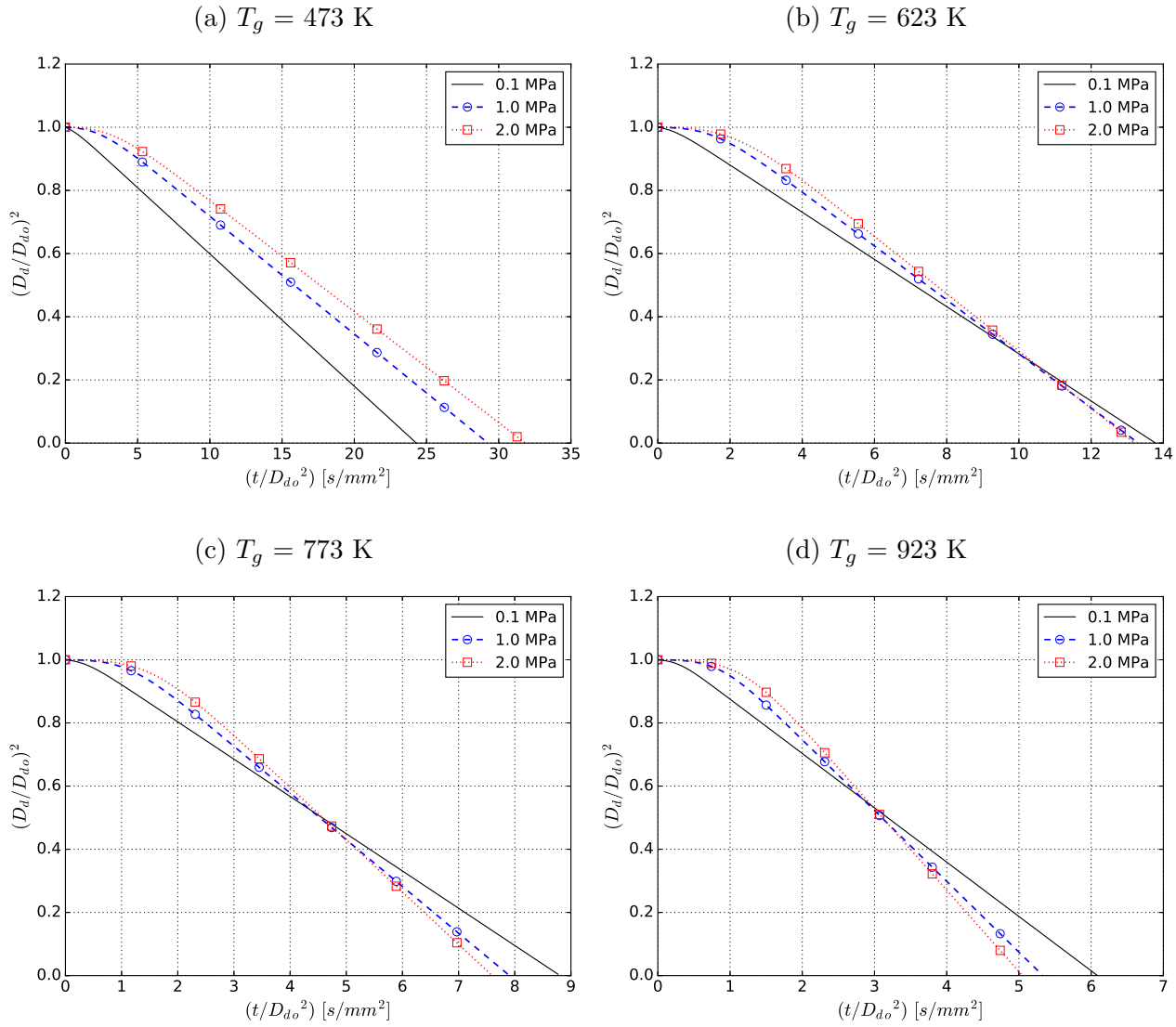

lifetime, which enhances the unsteady effects of the droplet evaporation. Additionally, this same time ratio is almost independent of gas temperature at low ambient pressure; however, as ambient pressure is increased, its tendency to enhance with gas temperature becomes remarkable. This longer heat-up period is a consequence of the higher ambient pressure increasing the boiling temperature of the liquid substance, which implies that the droplet needs to be heated up to a high temperature to evaporate.

Investigations based on the results presented in Figs. 6.19 and 6.23a have also shown that there is a threshold ambient temperature that determines whether the evaporation rate will increase or decrease as the ambient pressure is enhanced. This behavior can be explained by

Figure 6.20: Variations of normalized squared droplet diameter with the time divided by squared initial droplet diameter at high temperature and various ambient pressures.

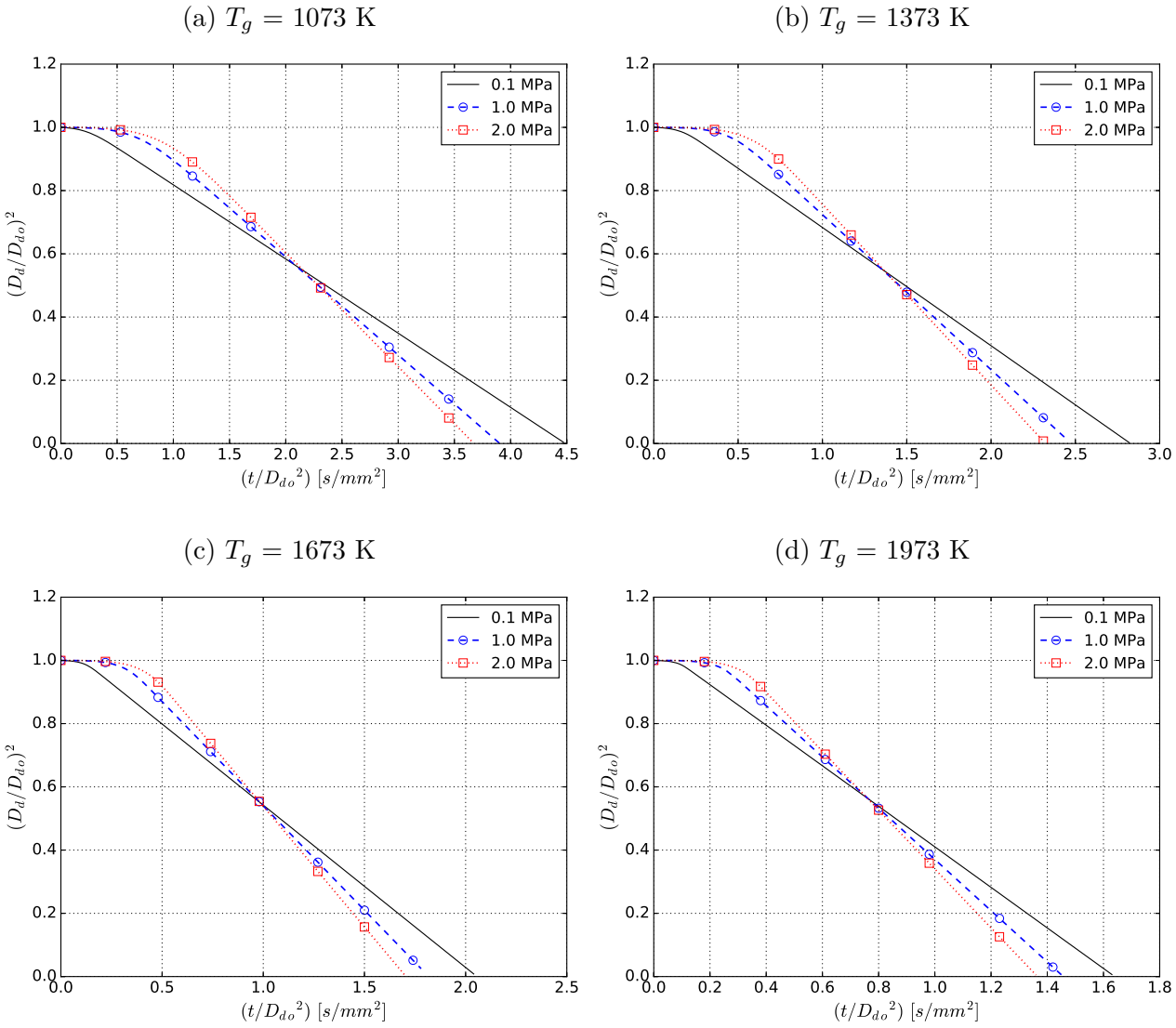

the existence of two competing factors that influence the evaporation rate. First, increasing the ambient pressure enhances the boiling temperature, decreasing the Spalding mass transfer number and, consequently, the evaporation rate is reduced. Second, increasing the ambient pressure also enhances the droplet temperature independent of the ambient temperature (see Figs. 6.21, 6.22 and 6.24), which reduces the latent heat of evaporation and, as a result, the evaporation rate is augmented. Hence, the way the evaporation rate of pure fuel droplets is influenced by the ambient pressure is determined by the net result of those two factors (LONG *et al.*, 2015). For ambient temperatures below the threshold temperature, the first factor predominates. However, when the ambient temperature is higher than the threshold temperature, the second factor has a stronger

Figure 6.21: Variations of droplet temperature with the time divided by squared initial droplet diameter at low temperature and various ambient pressures.

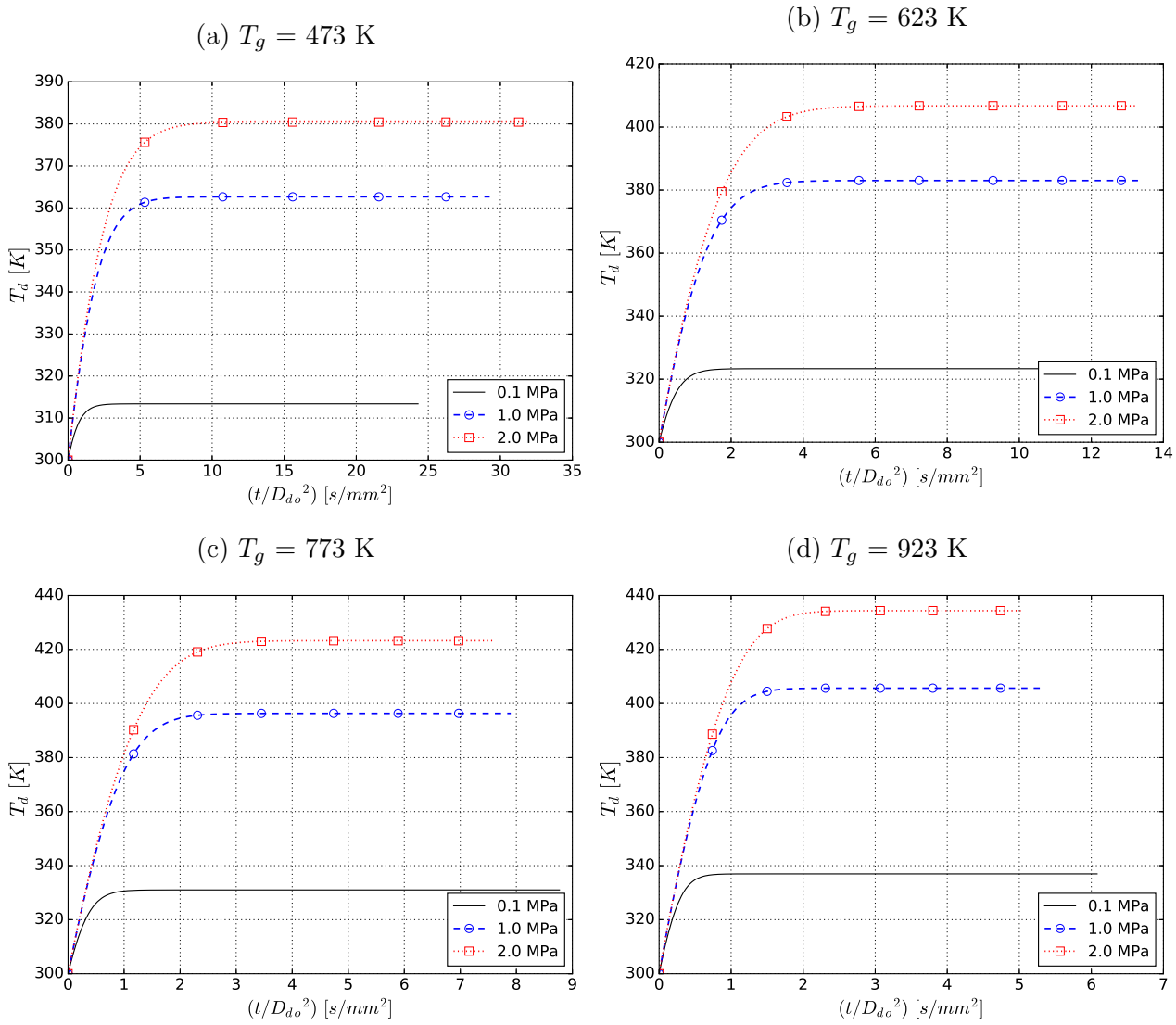

impact on the evaporation rate. As can be observed in Fig 6.23, the first factor predominates only for 473 K, since the threshold temperature for ethanol is approximately 573 K.

6.7 MFSim simulations

The simulations performed with the MFSim computational platform in order to verify if the evaporation models and their parallelization were correct implemented are presented in this section.

Figure 6.22: Variations of droplet temperature with the time divided by squared initial droplet diameter at high temperature and various ambient pressures.

(a) $T_g = 1073$ K

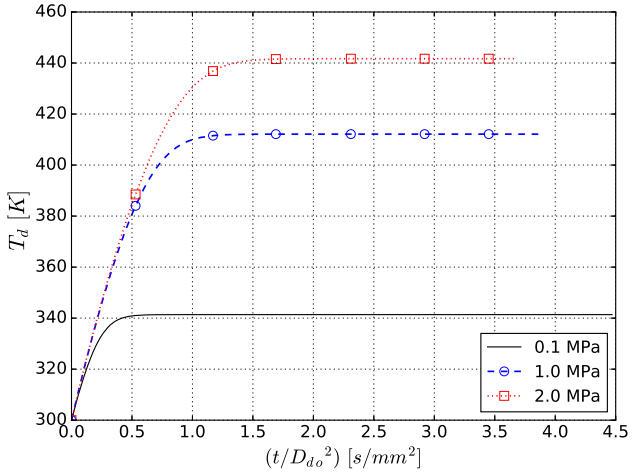

(b) $T_g = 1373$ K

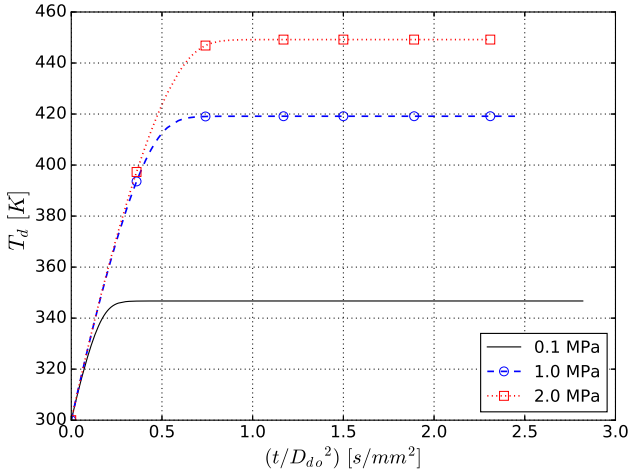

(c) $T_g = 1673$ K

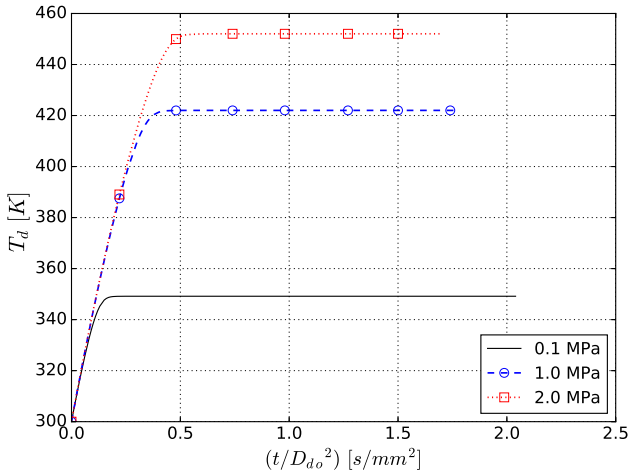

(d) $T_g = 1973$ K

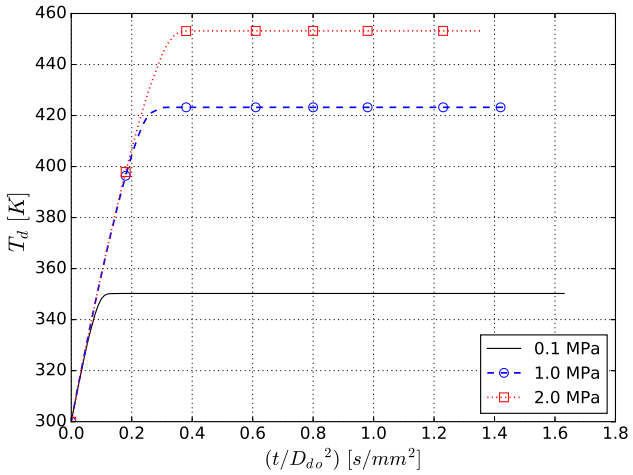

6.7.1 Python versus *MFSim: implementation verification*

One of the test cases proposed in Subsection 6.2.2 was chosen to compare Python routine and MFSim performances. This test case conditions are summarized in Table 6.2 and the computational domain is illustrated in Fig. 6.25.

In Figures 6.26, 6.27 and 6.28, the authors show each evaporation model droplet diameter and temperature predictions for Python and MFSim. For both droplet parameters, identical results were exhibited, as expected.

In Figure 6.29, the authors display the visualization for droplet evaporation computed in MFSim with CEM. The data was post-processed with ParaView. The droplet heat-up period is

Figure 6.23: Average area evaporation rates at various ambient pressures.

(a) Low temperatures

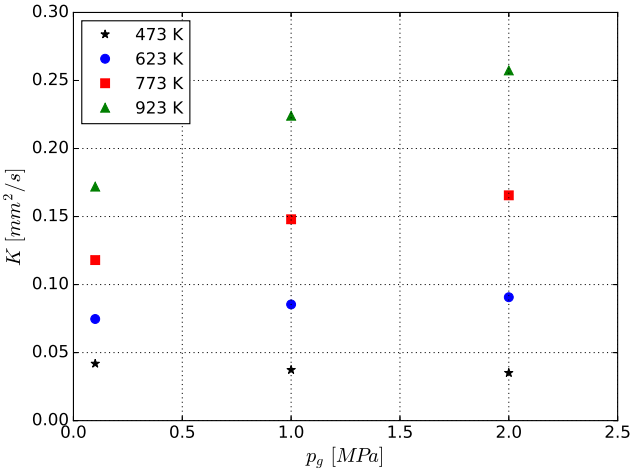

(b) High temperatures

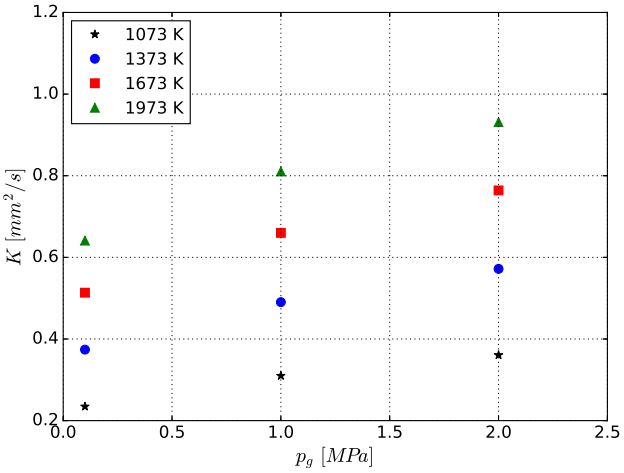

Figure 6.24: Droplet final equilibrium temperature at various ambient pressures.

(a) Low temperatures

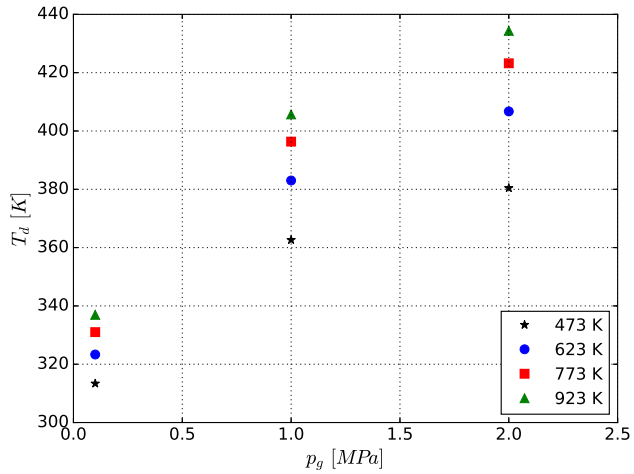

(b) High temperatures

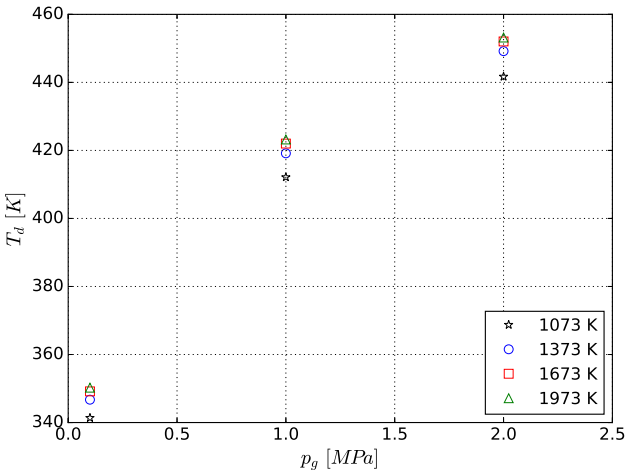

Table 6.2: Simulation conditions for evaporation models verification in MFSim

Droplet	N-heptane
Gas	Nitrogen
D_{do}	500 μm
T_{do}	300 K
p_g	0.1 MPa
T_g	748 K

depicted from t = 0 to t = 0.24 s; after that, the droplet diameter reduction becomes more noticeable.

Figure 6.25: Schematic representation of the computational domain for the evaporation of a single droplet.

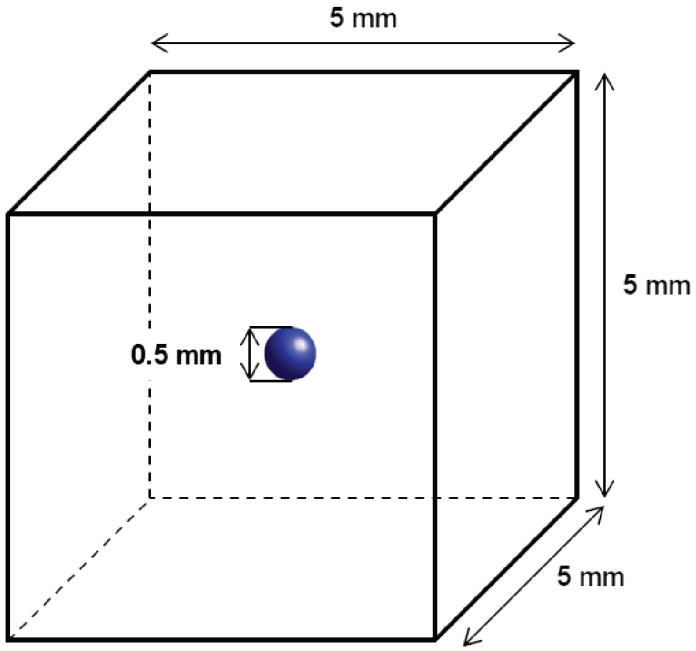

Figure 6.26: Temporal variation of (a) normalized squared droplet diameter and (b) temperature for CEM comparing Python and MFSim predictions.

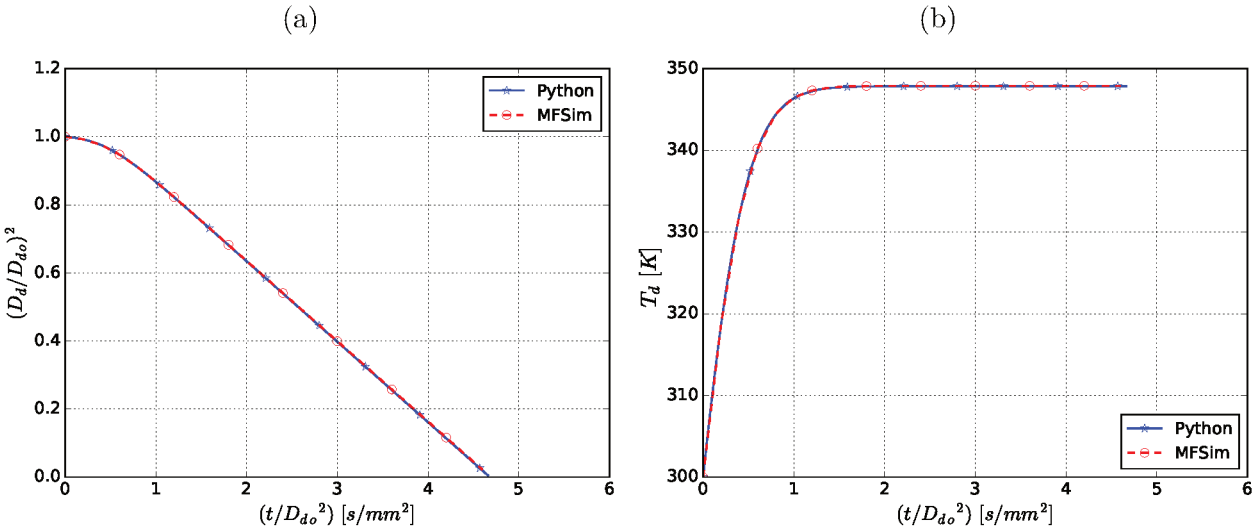

6.7.2 Vortex flow: parallelization verification

A last verification test employing a vortex flow has been performed to investigate the behavior of the parallelization routine when the evaporation models are considered. It is worth recalling that the Python routine is serial, while MFSim is essentially parallel. Moreover, for spray

Figure 6.27: Temporal variation of (a) normalized squared droplet diameter and (b) temperature for ASM comparing Python and MFSim predictions.

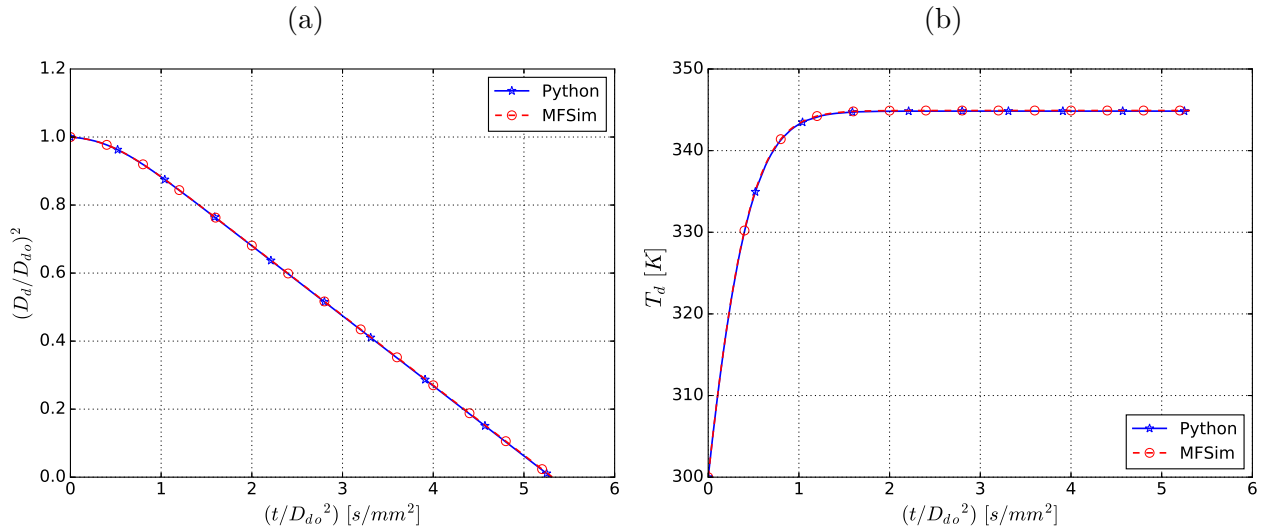

Figure 6.28: Temporal variation of (a) normalized squared droplet diameter and (b) temperature for NEQ comparing Python and MFSim predictions.

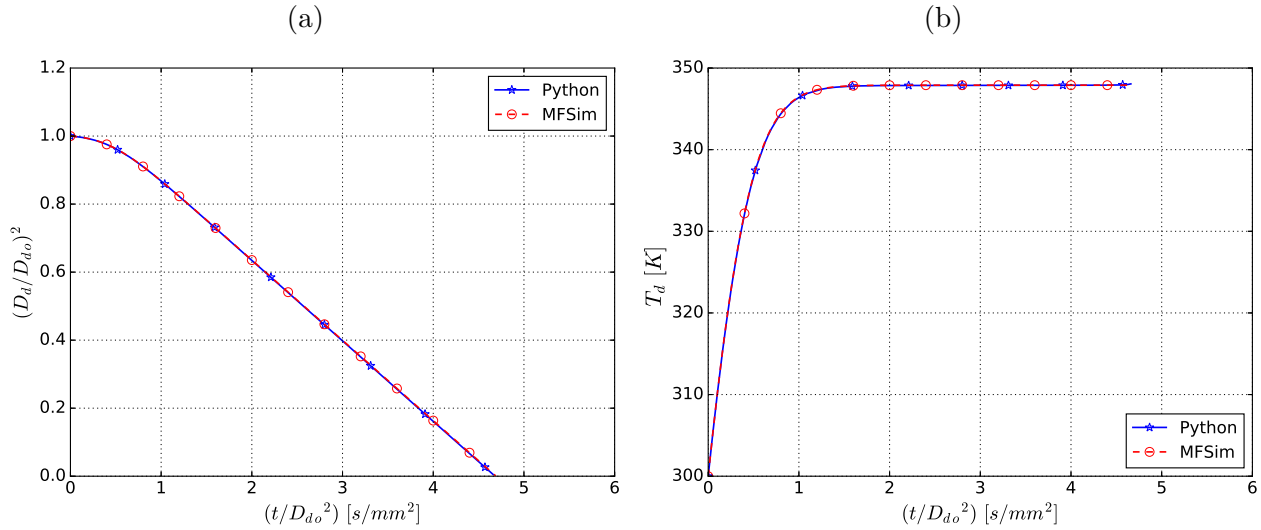

simulations, the resort to parallel processing is unavoidable. Hence, the evaporation computational routines must be assessed in a distributed processing environment.

The three-dimensional, time-dependent and periodic velocity field of the vortex flow is

given by (LEVEQUE, 1996):

$$\begin{aligned} u(x,y,z,t) &= 2sin^2(\pi x)sin(2\pi y)sin(2\pi z)cos(\pi t/T), \\ v(x,y,z,t) &= -sin(2\pi x)sin^2(\pi y)sin(2\pi z)cos(\pi t/T), \\ w(x,y,z,t) &= -sin(2\pi x)sin(2\pi y)sin^2(\pi z)cos(\pi t/T), \end{aligned} \tag{6.4}$$

where T is the time of one period. For the present investigation, the flow field is modulated in time with a period of $T = 3$. This vortex flow is applied to a group of 1000 droplets confined in a spherical region with 0.9 m diameter, distributed randomly, and with log-normal droplet diameter distribution, which is illustrated by Fig. 6.30.

Distribution functions are based on the random occurrence of a given droplet size and they are usually expressed in terms of a number distribution function $f(D_d)$ that gives the number of droplets of a given diameter D_d. The log-normal distribution is frequently used to represent the size of droplets. It derives from the normal or Gaussian distribution and is defined as (JOHNSON; KOTZ; BALAKRISHNAN, 1994):

$$f(D_d) = \frac{1}{\sqrt{2\pi}\sigma D_d} exp\left[-\frac{1}{2}\left(\frac{ln(D_d) - \mu}{\sigma}\right)^2\right], \tag{6.5}$$

where σ is the standard deviation and μ is the mean. For the present investigation, $\mu = 0.75$ mm and $\sigma = 0.25$ mm, resulting in the probability density function exhibited in Fig. 6.30(c).

The evaporation of this group of droplets, where the droplets are colored by their diameter, is displayed in Fig. 6.31. Then, one of the droplets from Fig. 6.31 was tracked in the domain during 2.5 s for both serial and parallel processing in order to compare their performances. For the parallel processing, the droplet has changed from one processor to another 3 times during the evaluated period. As it can be observed in Fig. 6.32, there is no peak or discontinuity when the droplet passes between processors. In fact, all the parameters evolution, i.e. droplet diameter, mass, temperature and velocity, are exactly equal for serial and parallel processing.

Figure 6.29: Droplet evaporation for CEM simulation, in which it is colored by temperature and its diameter reduces.

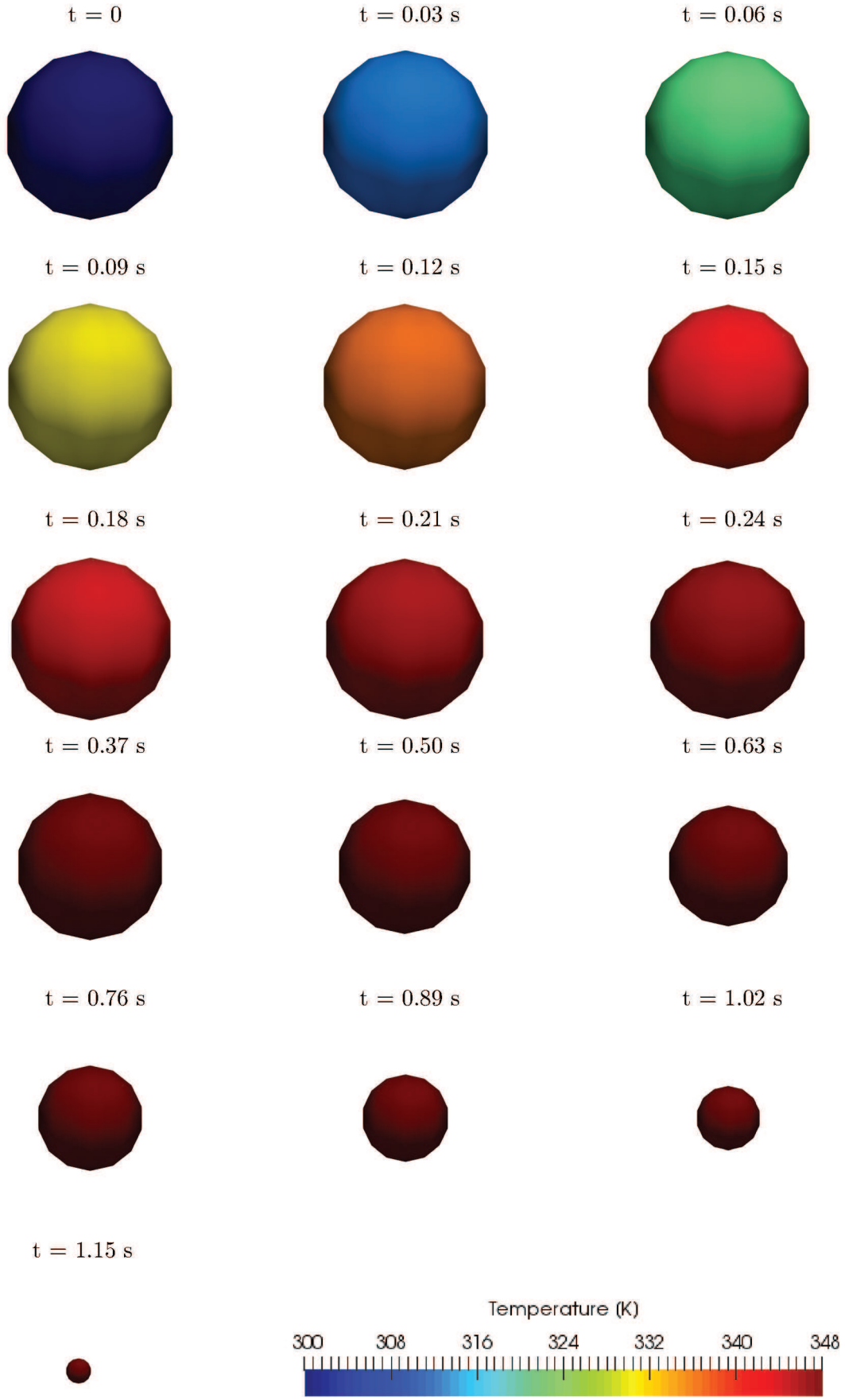

Figure 6.30: Computational domain and initial droplet diameter distribution.

(a) Schematic representation of the computational domain for a group of droplets

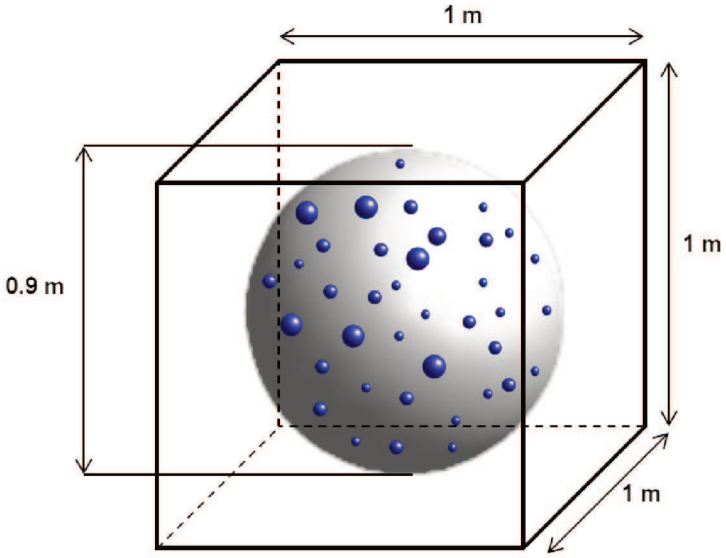

(b) Droplets random spatial distribution

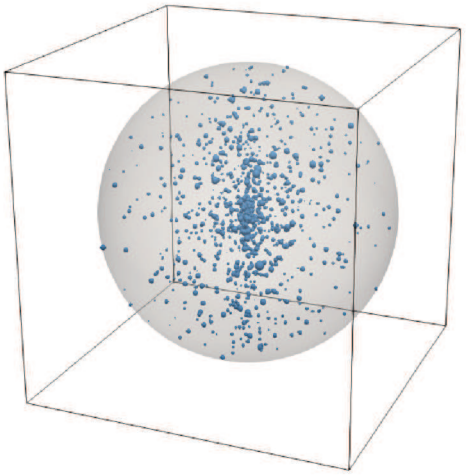

(c) Droplet diameter log-normal distribution

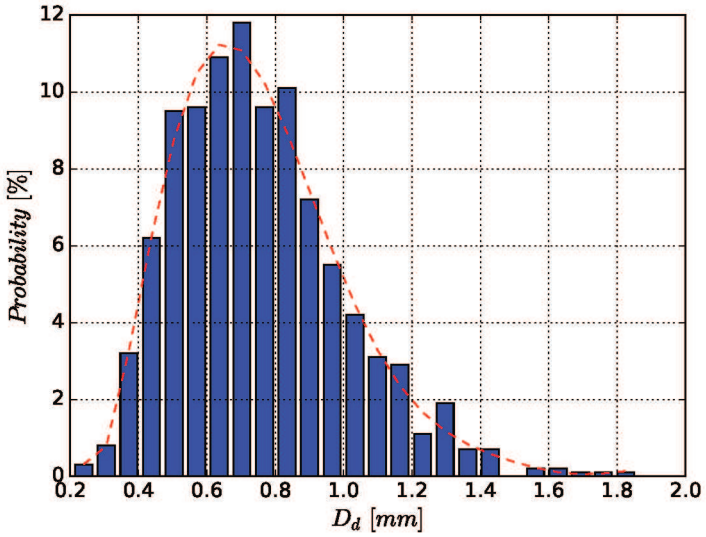

Figure 6.31: Vortex flow with droplet evaporation.

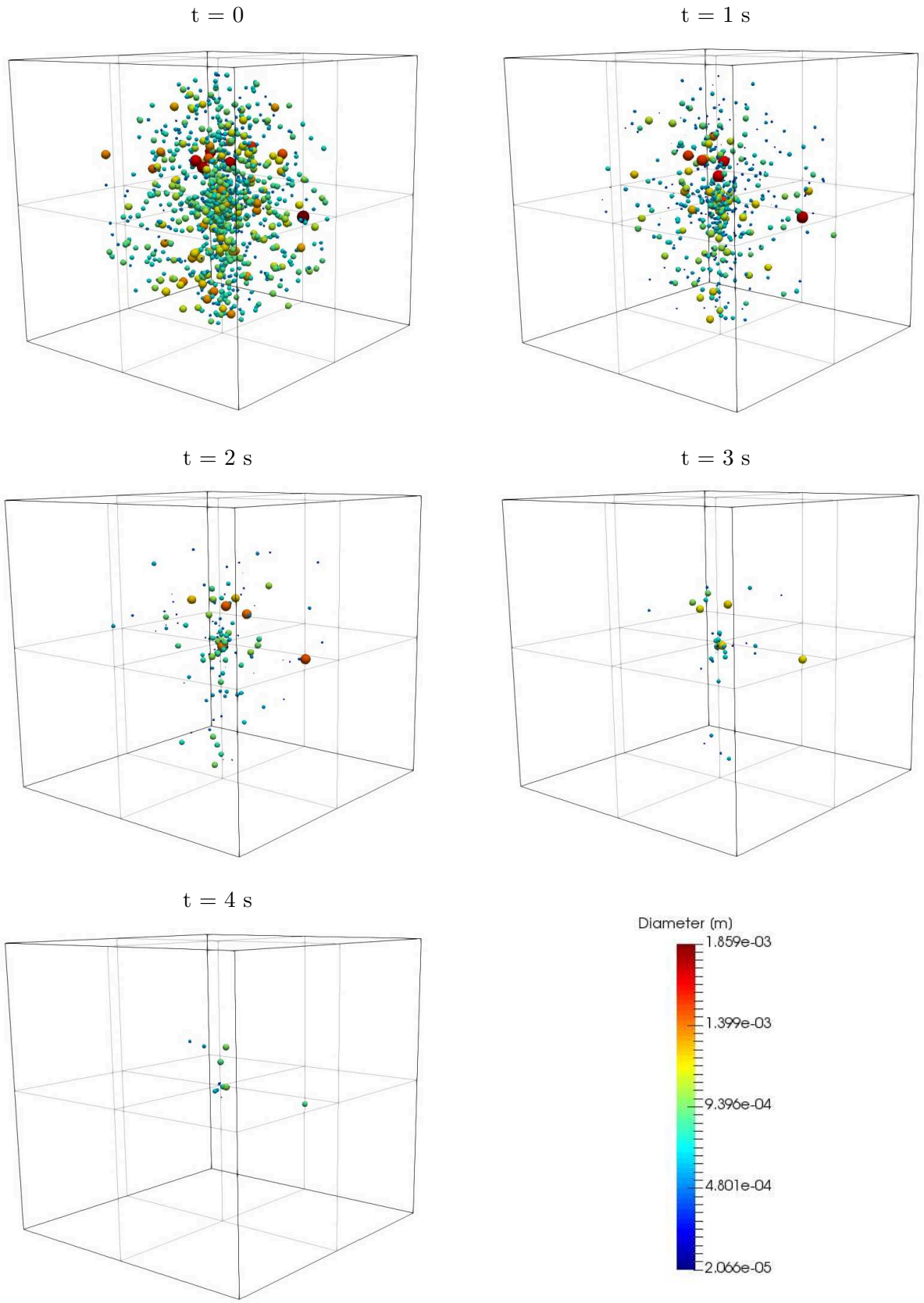

Figure 6.32: Serial *versus* parallel computation, where the vertical lines represent the droplet passing between processors.

(a) Droplet diameter

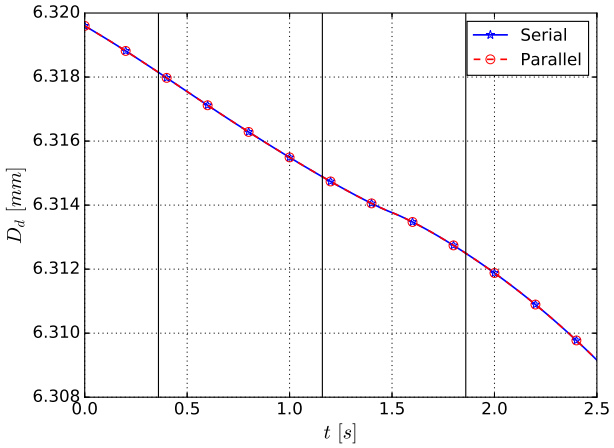

(b) Droplet mass

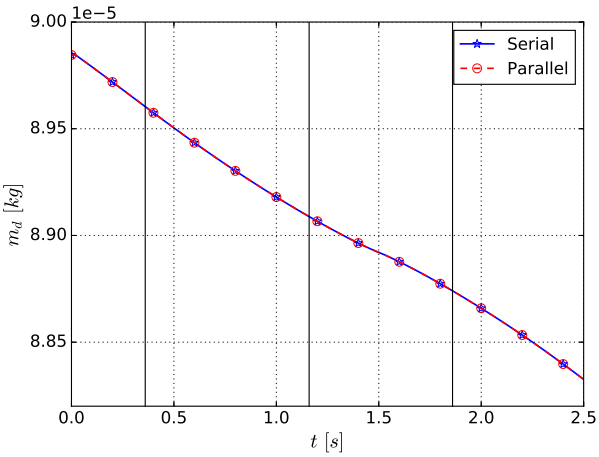

(c) Droplet temperature

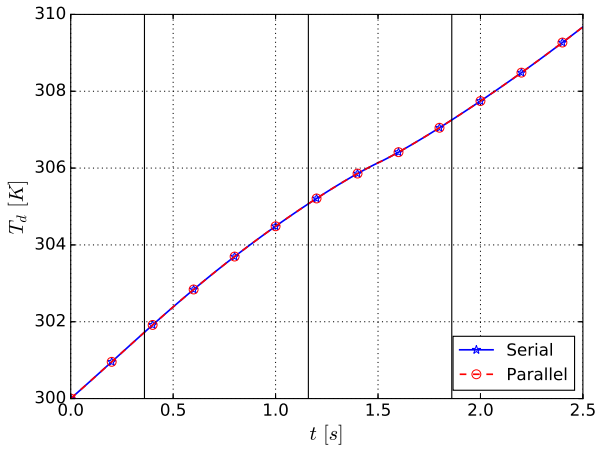

(d) Droplet velocity in the x direction

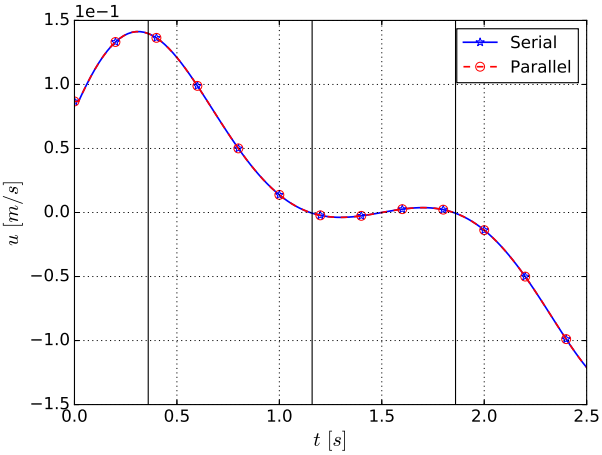

(e) Droplet velocity in the y direction

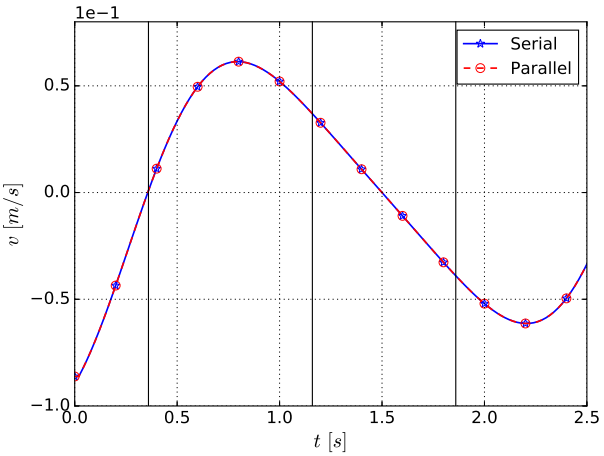

(f) Droplet velocity in the z direction

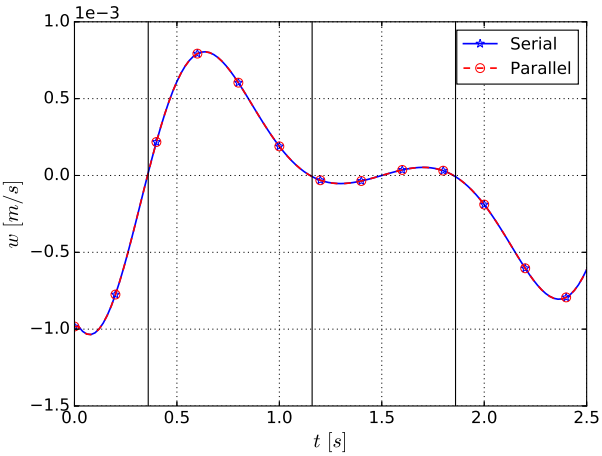

CHAPTER VII

CONCLUSIONS AND RECOMMENDATIONS

In this chapter, the studies conducted in the present dissertation are summarized, some main conclusions are discussed, and recommendations for future studies are provided.

7.1 Model development

The present dissertation is focused on the computational modeling of droplet evaporation following the Eulerian-Lagrangian approach with point droplet approximation. Three different evaporation models, i.e. CEM, ASM and NEQ, have been implemented and coupled with the open-source package Cantera for physical properties calculation. These models have been tested for several substances, e.g. water, n-heptane, n-decane and ethanol, under a wide range of ambient gas temperature and pressure conditions. First, the simulations have been performed using a Python routine and, once the models were validated, this evaporation module has been incorporated into the MFSim code. Besides the scientific conclusions, which are summarized in Section 7.3, the contributions of the present dissertation also include the implementation of Lagrangian droplet evaporation models into the in-house code MFSim with the C++ Cantera application, allowing the simulation of spray evaporation.

7.2 Validation and investigations

Careful validation of the computational results with available experimental data is crucial for the creation of a reliable modeling approach. In the present dissertation, the following five steps have been taken to develop, verify, validate and apply the evaporation modeling approach.

1. To establish a well-defined physical model and derive its mathematical and numerical models;

2. To verify ASM implementation and the computational procedure for Lagrangian droplet evaporation;

3. To test the performance of different evaporation models on selected cases in order to validate their predictions by comparison against experimental measurements;

4. To investigate the incorporation of natural and forced convection by means of the Ranz-Marshall empirical correlation;

5. To explore ambient condition influence on evaporation.

In Section 6.2, the evaporation models have been tested and compared against each other and against experimental data for cases of low and high evaporation rates. The validation results clearly demonstrated that the evaporation modeling approach is not only able to reproduce characteristic trends described in the literature, such as (i) a heat-up period followed by the linear D^2 law, and (ii) droplet equilibrium temperature tending to the wet-bulb temperature, but also correctly reproduced evaporation rates measured experimentally. Additionally, based on the validation results, further investigations were needed to determine the real contributions of considering de Langmuir-Knudsen law in NEQ and to explain why NEQ and CEM predictions were very similar for all the validation cases.

Ambient condition effects on ethanol evaporation have been explored in order to gain deeper insight on this alternative fuel evaporation features. Due to the limitation arising from not considering the solubility of the gas into the droplet and the real-gas effects on vapor-liquid equilibrium at the gaseous film surrounding the droplet, the effect of pressures higher than 2.0 MPa cannot be studied. In other words, the evaporation modeling approach here proposed and

followed is not valid for near-critical or supercritical conditions. Moreover, at high pressure, the droplet may also deform, making the spherical symmetry assumption no longer valid, due to a decrease in the surface tension. Lack of information is also an issue for model validation under high-pressure conditions, since there is no experimental data available nowadays for ambient pressure different from atmospheric using the cross-fiber technique, to the best knowledge of the authors.

Based on the confidence gained in the steps of verification and validation previously mentioned, and the understanding of the computational procedure, in terms of Lagrangian solver and Cantera functions use, it was easier to implement the evaporation models in MFSim. Introducing a Lagrangian evaporation module in MFSim increases the range of possibilities for test cases, considering the interaction between Lagrangian and Eulerian phases and the many functionalities already existing in the Lagrangian module, e.g. droplet injection and diameter distribution.

7.3 Main conclusions

Based on the modeling results obtained during validation and investigations steps, the main conclusions are summarized as follows.

Comparison between some theoretical model predictions and experimental measurements for several ambient gas temperatures shows that the ASM presents the most physically coherent results predicting the evaporation characteristics of n-heptane droplets under high-evaporation-rate conditions. It was the only model investigated in the present study that did not overestimate the area evaporation rate when compared with the experimental data for the ambient and initial conditions evaluated.

The addition of a deviation factor to consider non-equilibrium effects in NEQ does not cause any significant change in the evolution of droplet size and temperature history when compared with CEM results under all ambient conditions tested here. This behavior indicates that the advantages of using NEQ are actually due to the correction factor incorporated to express the existence of a thermal flux due to the vapor diffusion. Even though the non-equilibrium contribution seems to be remarkable for initial droplet size smaller than 50 μm, the vapor mass fraction predictions from NEQ and CEM continue to be exactly alike.

overestimate the evaporation rate when compared with experimental data for atmospheric pressure. Therefore, this approach to take natural convection into account should be used carefully in order to avoid wrong droplet lifetime prediction, since it is usually used as a design parameter in engineering applications.

When forced convection effects are incorporated with the traditional Ranz-Marshall empirical correlation, the behavior previously observed for n-heptane simulations is preserved in terms of the differences and similarities between the three evaporation models evaluated, i.e., ASM predicts a lower evaporation rate when compared to CEM and NEQ, and CEM and NEQ predictions are exactly alike.

Comparison between the predictions of ASM and experimental data for ethanol evaporation showed good agreement for all the conditions tested. Then, the effects of ambient conditions on ethanol evaporation characteristics were investigated for low and high pressure and temperature by means of numerical simulations. Under ambient temperatures higher than the threshold temperature, the evaporation rate augments with the increase of ambient pressure, contrary to what happens for cases when the ambient temperature is lower than the threshold temperature. It was also observed that increasing the ambient pressure enhances the initial heat-up period for all ambient temperatures.

The results achieved using the Python routine were also achieved by MFSim simulations. MFSim evaporation module parallelization was also verified by simulating a vortex flow test case, which imposes a velocity field variable in space and time. Droplets were still recognized even when they pass from one processor to another and comparison of serial and parallel computations shows no difference on droplet parameter predictions.

7.4 Recommendations

In the present research it was only possible to study the isolated evaporation process. Although the outcome was satisfying in view of the proposed objectives, some topics may be interesting for future research. These topics are listed below.

For the present research, only the one-way coupling methodology was applied, meaning that the presence of the droplets is not capable of affecting the Eulerian field around them.

Knowing that this assumption is a limiting factor, two-way coupling methodology development would increase the applicability of the Lagrangian droplet evaporation model. In two-way coupling methodology, source terms would be computed considering droplet velocity, mass and temperature temporal evolution and their values would be accounted in the Eulerian field computations.

For spray evaporation under dense and turbulent regime, droplet-droplet and droplet-wall interactions and droplet dispersion should also be carefully modeled. For simulation of high-pressure cases, non-ideal effects should be considered to determine the vapor-liquid equilibrium. For applications involving blend droplets, the evaporation models already implemented should be adapted to a multi-component approach.

BIBLIOGRAPHY

ABDELSAMIE, A.; THÉVENIN, D. Direct numerical simulation of spray evaporation and autoignition in a temporally-evolving jet. *Proceedings of the Combustion Institute*, v. 36, n. 2, p. 2493 – 2502, 2017. Available at: <http://dx.doi.org/10.1016/j.proci.2016.06.030>.

ABRAMZON, B.; SAZHIN, S. Droplet vaporization model in the presence of thermal radiation. *International Journal of Heat and Mass Transfer*, v. 48, n. 9, p. 1868 – 1873, 2005. Available at: <https://doi.org/10.1016/j.ijheatmasstransfer.2004.11.017>.

ABRAMZON, B.; SAZHIN, S. Convective vaporization of a fuel droplet with thermal radiation absorption. *Fuel*, v. 85, n. 1, p. 32 – 46, 2006. Available at: <https://doi.org/10.1016/j.fuel.2005.02.027>.

ABRAMZON, B.; SIRIGNANO, W. Droplet vaporization model for spray combustion calculations. *International Journal of Heat and Mass Transfer*, v. 32, n. 9, p. 1605 – 1618, 1989. Available at: <http://dx.doi.org/10.1016/0017-9310(89)90043-4>.

AGARWAL, A. K. Biofuels (alcohols and biodiesel) applications as fuels for internal combustion engines. *Progress in Energy and Combustion Science*, v. 33, n. 3, p. 233 – 271, 2007. Available at: <https://doi.org/10.1016/j.pecs.2006.08.003>.

ASHGRIZ, N. *Handbook of Atomization and Sprays: Theory and Applications*. 1. ed. Springer US, 2011. Available at: <http://dx.doi.org/10.1007/978-1-4419-7264-4>.

AZAMI, M. H.; SAVILL, M. Modelling of spray evaporation and penetration for alternative fuels. *Fuel*, v. 180, n. Supplement C, p. 514 – 520, 2016. Available at: <http://dx.doi.org/10.1016/j.fuel.2016.04.050>.

BADER, A.; KELLER, P.; HASSE, C. The influence of non-ideal vapor-liquid equilibrium on the evaporation of ethanol/iso-octane droplets. *International Journal of Heat and Mass Transfer*, v. 64, n. Supplement C, p. 547 – 558, 2013. Available at: <https://doi.org/10.1016/j.ijheatmasstransfer.2013.04.056>.

BARBI, F.; GASCHE, J. L.; SILVEIRA-NETO, A. da; VILLAR, M. M.; LIMA, R. S. de. Numerical simulation of the flow through a compressor-valve model using an immersed-boundary method. *Engineering Applications of Computational Fluid Mechanics*, Taylor & Francis, v. 10, n. 1, p. 255–271, 2016. Available at: <https://doi.org/10.1080/19942060.2016.1140076>.

BATCHELOR, G. K. *An Introduction to Fluid Dynamics*. Cambridge University Press, 2000. (Cambridge Mathematical Library). Available at: <http://dx.doi.org/10.1017/CBO9780511800955>.

BEISHUIZEN, N. *PDF modelling and particle-turbulence interaction of turbulent spray flames*. Phd Thesis — TU Delft, Delft University of Technology, 2008. Available at: <uuid:496e1cd3-2c8e-415f-bb57-08c98a576fe4>.

BELLAN, J. Supercritical (and subcritical) fluid behavior and modeling: drops, streams, shear and mixing layers, jets and sprays. *Progress in Energy and Combustion Science*, v. 26, n. 4, p. 329 – 366, 2000. Available at: <https://doi.org/10.1016/S0360-1285(00)00008-3>.

BELLAN, J.; SUMMERFIELD, M. Theoretical examination of assumptions commonly used for the gas phase surrounding a burning droplet. *Combustion and Flame*, v. 33, n. Supplement C, p. 107 – 122, 1978. Available at: <https://doi.org/10.1016/0010-2180(78)90054-8>.

BERGTHORSON, J. M.; THOMSON, M. J. A review of the combustion and emissions properties of advanced transportation biofuels and their impact on existing and future engines. *Renewable and Sustainable Energy Reviews*, v. 42, n. Supplement C, p. 1393 – 1417, 2015. Available at: <https://doi.org/10.1016/j.rser.2014.10.034>.

BIRD, R. B.; STEWART, W. E.; LIGHTFOOT, E. N. *Transport Phenomena*. 2. ed. [S.l.]: John Wiley & Sons, 2002.

BORODULIN, V.; LETUSHKO, V.; NIZOVTSEV, M.; STERLYAGOV, A. Determination of parameters of heat and mass transfer in evaporating drops. *International Journal of Heat and Mass Transfer*, v. 109, n. Supplement C, p. 609 – 618, 2017. Available at: <https://doi.org/10.1016/j.ijheatmasstransfer.2017.02.042>.

Chapter I - Quasi-stationary evaporation and growth of droplets motionless relative to the medium. In: BRADLEY, R.; FUCHS, N. (Ed.). *Evaporation and Droplet Growth in Gaseous Media*. Pergamon, 1959. p. 1 – 37. Available at: <https://doi.org/10.1016/B978-1-4832-0060-6.50005-3>.

CAI, L.; PITSCH, H.; MOHAMED, S. Y.; RAMAN, V.; BUGLER, J.; CURRAN, H.; SARATHY, S. M. Optimized reaction mechanism rate rules for ignition of normal alkanes. *Combustion and Flame*, v. 173, p. 468 – 482, 2016. Available at: <https://doi.org/10.1016/j.combustflame.2016.04.022>.

CAMPOS-FERNÁNDEZ, J.; ARNAL, J. M.; GÓMEZ, J.; DORADO, M. P. A comparison of performance of higher alcohols/diesel fuel blends in a diesel engine. *Applied Energy*, v. 95, n. Supplement C, p. 267 – 275, 2012. Available at: <https://doi.org/10.1016/j.apenergy.2012.02.051>.

CASTANET, G.; PERRIN, L.; CABALLINA, O.; LEMOINE, F. Evaporation of closely-spaced interacting droplets arranged in a single row. *International Journal of Heat and Mass Transfer*, v. 93, p. 788 – 802, 2016. Available at: <https://doi.org/10.1016/j.ijheatmasstransfer.2015.09.064>.

CENICEROS, H. D.; ROMA, A. M.; SILVEIRA-NETO, A.; VILLAR, M. M. A robust, fully adaptive hybrid level-set/front-tracking method for two-phase flows with an accurate surface tension computation. In: . [s.n.], 2009.

CHAUVEAU, C.; HALTER, F.; LALONDE, A.; GÖKALP, I. An experimental study on the droplet vaporization: effects of heat conduction through the support fiber. In: *Proc. of 22nd Annual Conference on Liquid Atomization and Spray Systems (Europe 2008)*. [S.l.: s.n.], 2008. v. 59, p. 61.

CHEN, Y.-C.; STÅRNER, S. H.; MASRI, A. R. A detailed experimental investigation of well-defined, turbulent evaporating spray jets of acetone. *International Journal of Multiphase Flow*, v. 32, n. 4, p. 389 – 412, 2006. Available at: <http://dx.doi.org/10.1016/j.ijmultiphaseflow.2005.09.002>.

CHRIGUI, M.; GOUNDER, J.; SADIKI, A.; MASRI, A. R.; JANICKA, J. Partially premixed reacting acetone spray using LES and FGM tabulated chemistry. *Combustion and Flame*, v. 159, n. 8, p. 2718 – 2741, 2012. Special Issue on Turbulent Combustion. Available at: <https://doi.org/10.1016/j.combustflame.2012.03.009>.

CLIFT, R.; GRACE, J. R.; WEBER, M. E. *Bubbles, Drops, and Particles*. [S.l.]: Academic Press, 1978.

CORSETTI, S.; MILES, R. E. H.; MCDONALD, C.; BELOTTI, Y.; REID, J. P.; KIEFER, J.; MCGLOIN, D. Probing the evaporation dynamics of ethanol/gasoline biofuel blends using single droplet manipulation techniques. *The Journal of Physical Chemistry A*, v. 119, n. 51, p. 12797–12804, 2015. Available at: <http://dx.doi.org/10.1021/acs.jpca.5b10098>.

DAMASCENO, M. M. R.; FREITAS SANTOS, J. G. de; VEDOVOTO, J. M. Simulation of turbulent reactive flows using a FDF methodology – Advances in particle density control for normalized variables. *Computers & Fluids*, v. 170, p. 128 – 140, 2018. Available at: <https://doi.org/10.1016/j.compfluid.2018.05.004>.

DAVIS, E. J.; SCHWEIGER, G. *The Airborne Microparticle: Its Physics, Chemistry, Optics, and Transport Phenomena*. 1. ed. Springer-Verlag Berlin Heidelberg, 2012. Available at: <http://dx.doi.org/10.1007/978-3-642-56152-8>.

DE, S.; LAKSHMISHA, K.; BILGER, R. W. Modeling of nonreacting and reacting turbulent spray jets using a fully stochastic separated flow approach. *Combustion and Flame*, v. 158, n. 10, p. 1992 – 2008, 2011. Available at: <http://dx.doi.org/10.1016/j.combustflame.2011.03.006>.

DEISING, D.; BOTHE, D.; MARSCHALL, H. Direct numerical simulation of mass transfer in bubbly flows. *Computers Fluids*, 2018. Available at: <https://doi.org/10.1016/j.compfluid.2018.03.041>.

DENNER, F.; HEUL, D. R. van der; OUD, G. T.; VILLAR, M. M.; SILVEIRA NETO, A. da; WACHEM, B. G. van. Comparative study of mass-conserving interface capturing frameworks for two-phase flows with surface tension. *International Journal of Multiphase Flow*, v. 61, n. Supplement C, p. 37 – 47, 2014. Available at: <https://doi.org/10.1016/j.ijmultiphaseflow.2013.12.011>.

DUARTE, B. A. d. F.; MELO, R. R. d. S.; VILLAR, M. M.; SERFATY, R.; NETO, A. d. S. An extension of oberbeck-boussinesq approximation for thermal convection problems. *Journal of the Brazilian Society of Mechanical Sciences and Engineering*, v. 40, n. 6, p. 317, 2018. Available at: <https://doi.org/10.1007/s40430-018-1181-x>.

EBRAHIMIAN, V.; NICOLLE, A.; HABCHI, C. Detailed modeling of the evaporation and thermal decomposition of urea-water solution in SCR systems. *AIChE Journal*, Wiley Online Library, v. 58, n. 7, p. 1998–2009, 2012. Available at: <https://doi.org/10.1002/aic.12736>.

FAETH, G. Evaporation and combustion of sprays. *Progress in Energy and Combustion Science*, v. 9, n. 1, p. 1 – 76, 1983. Available at: <http://dx.doi.org/10.1016/0360-1285(83)90005-9>.

FANG, J.; CAMBARERI, J. J.; BROWN, C. S.; FENG, J.; GOUWS, A.; LI, M.; BOLOTNOV, I. A. Direct numerical simulation of reactor two-phase flows enabled by high-performance computing. *Nuclear Engineering and Design*, v. 330, p. 409 – 419, 2018. Available at: <https://doi.org/10.1016/j.nucengdes.2018.02.024>.

FERREIRA, V. M. V. *A hybrid LES/Lagrangian FDF method on adaptive, block-structured mesh*. Master's Thesis — Universidade Federal de Uberlândia, 2015. Available at: <https://repositorio.ufu.br/bitstream/123456789/14982/1/HybridLesLagrangian.pdf>.

FRÖSSLING, N. Über die verdungtung fallender tropfen. *Gerland's Beiträge für Geophysik*, v. 52, p. 170–216, 1938.

GHASSEMI, H.; BAEK, S. W.; KHAN, Q. S. Experimental study on binary droplet evaporation at elevated pressures and temperatures. *Combustion Science and Technology*, Taylor & Francis, v. 178, n. 6, p. 1031–1053, 2006. Available at: <https://doi.org/10.1080/00102200500296697>.

GHATA, N.; SHAW, B. D. Computational modeling of the effects of support fibers on evaporation of fiber-supported droplets in reduced gravity. *International Journal of Heat and Mass Transfer*, v. 77, n. Supplement C, p. 22 – 36, 2014. Available at: <https://doi.org/10.1016/j.ijheatmasstransfer.2014.04.074>.

GIVLER, S. D.; ABRAHAM, J. Supercritical droplet vaporization and combustion studies. *Progress in Energy and Combustion Science*, v. 22, n. 1, p. 1 – 28, 1996. Available at: <https://doi.org/10.1016/0360-1285(95)00013-5>.

GODSAVE, G. Studies of the combustion of drops in a fuel spray-the burning of single drops of fuel. *Symposium (International) on Combustion*, v. 4, n. 1, p. 818 – 830, 1953. Fourth Symposium (International) on Combustion. Available at: <https://doi.org/10.1016/S0082-0784(53)80107-4>.

GOODWIN, D. G.; MOFFAT, H. K.; SPETH, R. L. *Cantera: An Object-oriented Software Toolkit for Chemical Kinetics, Thermodynamics, and Transport Processes*. 2016. <http://www.cantera.org>. Version 2.2.1.

GREEN, D. W.; PERRY, R. H. *Perry's Chemical Engineers' Handbook*. [S.l.]: McGraw-Hill, 2007.

HALLETT, W.; BEAUCHAMP-KISS, S. Evaporation of single droplets of ethanol-fuel oil mixtures. *Fuel*, v. 89, n. 9, p. 2496 – 2504, 2010. Available at: <https://doi.org/10.1016/j.fuel.2010.03.007>.

HAN, K.; YANG, B.; ZHAO, C.; FU, G.; MA, X.; SONG, G. Experimental study on evaporation characteristics of ethanol-diesel blend fuel droplet. *Experimental Thermal and Fluid Science*, v. 70, n. Supplement C, p. 381 – 388, 2016. Available at: <https://doi.org/10.1016/j.expthermflusci.2015.10.001>.

HANSON, T. D. *Uthash*. 2013. <https://github.com/troydhanson/uthash>. Version 1.9.6.

HARSTAD, K.; BELLAN, J. An all-pressure fluid drop model applied to a binary mixture: heptane in nitrogen. *International Journal of Multiphase Flow*, v. 26, n. 10, p. 1675 – 1706, 2000. Available at: <https://doi.org/10.1016/S0301-9322(99)00108-1>.

HASHIMOTO, N.; NOMURA, H.; SUZUKI, M.; MATSUMOTO, T.; NISHIDA, H.; OZAWA, Y. Evaporation characteristics of a palm methyl ester droplet at high ambient temperatures. *Fuel*, v. 143, n. Supplement C, p. 202 – 210, 2015. Available at: <https://doi.org/10.1016/j.fuel.2014.11.057>.

HILL, M. J. M. On a spherical vortex. *Philosophical Transactions of the Royal Society of London A: Mathematical, Physical and Engineering Sciences*, The Royal Society, v. 185, p. 213–245, 1894. Available at: <http://dx.doi.org/10.1098/rsta.1894.0006>.

HUBBARD, G.; DENNY, V.; MILLS, A. Droplet evaporation: Effects of transients and variable properties. *International Journal of Heat and Mass Transfer*, v. 18, n. 9, p. 1003 – 1008, 1975. Available at: <https://doi.org/10.1016/0017-9310(75)90217-3>.

IEA - International Energy Agency. *International Energy Outlook*. 2016. Available at: <https://www.eia.gov/outlooks/ieo/pdf/0484(2016).pdf>.

IRFAN, M.; MURADOGLU, M. A front tracking method for direct numerical simulation of evaporation process in a multiphase system. *Journal of Computational Physics*, v. 337, p. 132 – 153, 2017. Available at: <https://doi.org/10.1016/j.jcp.2017.02.036>.

JAEGLE, F. *Large eddy simulation of evaporating sprays in complex geometries using Eulerian and Lagrangian methods*. Phd Thesis — Institut National Polytechnique de Toulouse - INPT, 2009. Available at: <https://tel.archives-ouvertes.fr/tel-00452501>.

JENNY, P.; ROEKAERTS, D.; BEISHUIZEN, N. Modeling of turbulent dilute spray combustion. *Progress in Energy and Combustion Science*, v. 38, n. 6, p. 846 – 887, 2012. Available at: <http://dx.doi.org/10.1016/j.pecs.2012.07.001>.

JESUS, W. C. de; ROMA, A. M.; PIVELLO, M. R.; VILLAR, M. M.; SILVEIRA-NETO, A. da. A 3D front-tracking approach for simulation of a two-phase fluid with insoluble surfactant. *Journal of Computational Physics*, v. 281, n. Supplement C, p. 403 – 420, 2015. Available at: <https://doi.org/10.1016/j.jcp.2014.10.021>.

JOHNSON, N.; KOTZ, S.; BALAKRISHNAN, N. *Continuous Univariate Distributions*. 2. ed. [S.l.]: John Wiley & Sons, 1994.

JONES, W.; LYRA, S.; MARQUIS, A. Large eddy simulation of evaporating kerosene and acetone sprays. *International Journal of Heat and Mass Transfer*, v. 53, n. 11, p. 2491 – 2505, 2010. Available at: <http://dx.doi.org/10.1016/j.ijheatmasstransfer.2010.01.028>.

KIM, H.; SUNG, N. The effect of ambient pressure on the evaporation of a single droplet and a spray. *Combustion and Flame*, v. 135, n. 3, p. 261 – 270, 2003. Available at: <https://doi.org/10.1016/S0010-2180(03)00165-2>.

KITANO, T.; NISHIO, J.; KUROSE, R.; KOMORI, S. Effects of ambient pressure, gas temperature and combustion reaction on droplet evaporation. *Combustion and Flame*, v. 161, n. 2, p. 551 – 564, 2014. Available at: <https://doi.org/10.1016/j.combustflame.2013.09.009>.

KONTOGEORGIS, G. M.; FOLAS, G. K. *Thermodynamic Models for Industrial Applications: From Classical and Advanced Mixing Rules to Association Theories*. 1. ed. John Wiley & Sons, 2010. Available at: <https://doi.org/10.1002/9780470747537>.

KULMALA, M.; VESALA, T.; SCHWARZ, J.; SMOLIK, J. Mass transfer from a drop - II: Theoretical analysis of temperature dependent mass flux correlation. *International Journal of Heat and Mass Transfer*, v. 38, n. 9, p. 1705 – 1708, 1995. Available at: <https://doi.org/10.1016/0017-9310(94)00302-C>.

KUO, K. K.-Y. *Principles of Combustion*. 2. ed. [S.l.]: Wiley-Interscience, 2005.

KUSZEWSKI, H. Experimental investigation of the effect of ambient gas temperature on the autoignition properties of ethanol-diesel fuel blends. *Fuel*, v. 214, p. 26 – 38, 2018. Available at: <https://doi.org/10.1016/j.fuel.2017.10.123>.

LEE, M. S.; RIAZ, A.; AUTE, V. Direct numerical simulation of incompressible multiphase flow with phase change. *Journal of Computational Physics*, v. 344, p. 381 – 418, 2017. Available at: <https://doi.org/10.1016/j.jcp.2017.04.073>.

LEFEBVRE, A. H. *Gas Turbine Combustion: Alternative Fuels and Emissions*. 3. ed. [S.l.]: CRC press, 2010. Available at: <https://doi.org/10.1201/9781420086058>.

LEFEBVRE, A. H.; MCDONELL, V. G. *Atomization and Sprays*. 2. ed. [S.l.]: CRC Press, Taylor & Francis, 2017. (Combustion: An International Series).

LEVEQUE, R. High-resolution conservative algorithms for advection in incompressible flow. *SIAM Journal on Numerical Analysis*, v. 33, n. 2, p. 627–665, 1996. Available at: <https://doi.org/10.1137/0733033>.

LI, T.; NISHIDA, K.; HIROYASU, H. Droplet size distribution and evaporation characteristics of fuel spray by a swirl type atomizer. *Fuel*, v. 90, n. 7, p. 2367 – 2376, 2011. Available at: <http://dx.doi.org/10.1016/j.fuel.2011.03.011>.

LIU, H. *Science and Engineering of Droplets: Fundamentals and Applications*. [S.l.]: William Andrew, 1999.

LONG, W.; YI, P.; JIA, M.; FENG, L.; CUI, J. An enhanced multi-component vaporization model for high temperature and pressure conditions. *International Journal of Heat and Mass Transfer*, v. 90, p. 857 – 871, 2015. Available at: <https://doi.org/10.1016/j.ijheatmasstransfer.2015.07.038>.

LUO, K.; PITSCH, H.; PAI, M.; DESJARDINS, O. Direct numerical simulations and analysis of three-dimensional n-heptane spray flames in a model swirl combustor. *Proceedings of the Combustion Institute*, v. 33, n. 2, p. 2143 – 2152, 2011. Available at: <https://doi.org/10.1016/j.proci.2010.06.077>.

MA, L. *Computational Modeling of Turbulent Spray Combustion*. Phd Thesis — TU Delft, Delft University of Technology, 2016. Available at: <http://doi.org/10.4233/uuid:c1c27066-a205-45f4-a7b4-e36016bc313a>.

MA, L.; NAUD, B.; ROEKAERTS, D. Transported PDF modeling of ethanol spray in hot-diluted coflow flame. *Flow, Turbulence and Combustion*, v. 96, n. 2, p. 469–502, 2016. Available at: <https://doi.org/10.1007/s10494-015-9623-3>.

MA, X.; ZHANG, F.; HAN, K.; YANG, B.; SONG, G. Evaporation characteristics of acetone-butanol-ethanol and diesel blends droplets at high ambient temperatures. *Fuel*, v. 160, n. Supplement C, p. 43 – 49, 2015. Available at: <https://doi.org/10.1016/j.fuel.2015.07.079>.

MAXWELL, J. C. Diffusion. In: _____. *The Scientific Papers of James Clerk Maxwell*. Cambridge University Press, 2011. (Cambridge Library Collection - Physical Sciences, v. 2), p. 625 – 646. Available at: <http://dx.doi.org/10.1017/CBO9780511710377.064>.

MILLER, R.; HARSTAD, K.; BELLAN, J. Evaluation of equilibrium and non-equilibrium evaporation models for many-droplet gas-liquid flow simulations. *International Journal of Multiphase Flow*, v. 24, n. 6, p. 1025 – 1055, 1998. Available at: <http://dx.doi.org/10.1016/S0301-9322(98)00028-7>.

NOMURA, H.; KONO, M.; SATO, J.; MARKS, G.; IGLSEDER, H.; RATH, H. J. Effects of the natural convection on fuel droplet evaporation. In: RATH, H. J. (Ed.). *Microgravity Fluid Mechanics*. Berlin, Heidelberg: Springer Berlin Heidelberg, 1992. p. 245–252. Available at: <https://link.springer.com/chapter/10.1007/978-3-642-50091-6_27>.

NOMURA, H.; UJIIE, Y.; RATH, H. J.; SATO, J.; KONO, M. Experimental study on high-pressure droplet evaporation using microgravity conditions. *Symposium (International) on Combustion*, v. 26, n. 1, p. 1267 – 1273, 1996. Available at: <https://doi.org/10.1016/S0082-0784(96)80344-4>.

PANTON, R. L. *Incompressible Flow*. 4. ed. John Wiley & Sons, 2013. Available at: <http://dx.doi.org/10.1002/9781118713075>.

PERSSON, T. *Eulerian-Lagrangian modeling of multicomponent spray for aseptic treatment of carton bottles in the food process and packaging industry*. Master's Thesis — Chalmers University of Technology, 2013. Available at: <http://publications.lib.chalmers.se/records/fulltext/219507/219507.pdf>.

PITSCH, H. Large-eddy simulation of turbulent combustion. *Annual Review of Fluid Mechanics*, Annual Reviews, v. 38, n. 1, p. 453–482, 2006. Available at: <http://dx.doi.org/10.1146/annurev.fluid.38.050304.092133>.

PIVELLO, M.; VILLAR, M.; SERFATY, R.; ROMA, A.; SILVEIRA-NETO, A. A fully adaptive front tracking method for the simulation of two phase flows. *International Journal of Multiphase Flow*, v. 58, n. Supplement C, p. 72 – 82, 2014. Available at: <https://doi.org/10.1016/j.ijmultiphaseflow.2013.08.009>.

QUBEISSI, M. A.; SAZHIN, S.; ELWARDANY, A. Modelling of blended diesel and biodiesel fuel droplet heating and evaporation. *Fuel*, v. 187, n. Supplement C, p. 349 – 355, 2017. Available at: <https://doi.org/10.1016/j.fuel.2016.09.060>.

QUIROGA, L. C. R.; BALESTIERI, J. A. P.; ÁVILA, I. Thermal behavior and kinetics assessment of ethanol/gasoline blends during combustion by thermogravimetric analysis. *Applied Thermal Engineering*, v. 115, n. Supplement C, p. 99 – 110, 2017. Available at: <https://doi.org/10.1016/j.applthermaleng.2016.12.051>.

RANZ, W.; MARSHALL, W. Evaporation from drops: Part I. *Chemical Engineering Progress*, v. 48, n. 3, p. 141–146, 1952.

RANZ, W.; MARSHALL, W. Evaporation from drops: Part II. *Chemical Engineering Progress*, v. 48, n. 3, p. 173–180, 1952.

RENKSIZBULUT, M.; YUEN, M. Experimental study of droplet evaporation in a high-temperature air stream. *Journal of Heat Transfer*, ASME, v. 105, n. 2, p. 384–388, 1983. Available at: <http://dx.doi.org/10.1115/1.3245590>.

RFA - Renewable Fuels Association. *World fuel ethanol production*. 2017. Available at: <http://www.ethanolrfa.org/resources/industry/statistics/>.

SACOMANO-FILHO, F. L. *Novel approach toward the consistent simulation of turbulent spray flames using tabulated chemistry*. Phd Thesis — TU Darmstadt, 2017. Available at: <http://tubiblio.ulb.tu-darmstadt.de/88246/>.

SADIKI, A.; CHRIGUI, M.; DREIZLER, A. Thermodynamically consistent modelling of gas turbine combustion sprays. In: _____. *Flow and Combustion in Advanced Gas Turbine Combustors*. Springer Netherlands, 2013. (Fluid Mechanics and Its Applications, v. 102), p. 55–90. Available at: <http://dx.doi.org/10.1007/978-94-007-5320-4>.

SADIKI, A.; CHRIGUI, M.; JANICKA, J.; MANESHKARIMI, M. R. Modeling and simulation of effects of turbulence on vaporization, mixing and combustion of liquid-fuel sprays. *Flow, Turbulence and Combustion*, v. 75, n. 1, p. 105–130, 2005. Available at: <http://dx.doi.org/10.1007/s10494-005-8579-0>.

SAHARIN, S. B.; LEFORT, B.; MORIN, C.; CHAUVEAU, C.; MOYNE, L. L.; KAFAFY, R. Vaporization characteristics of ethanol and 1-propanol droplets at high temperatures. *Atomization and Sprays*, v. 22, n. 3, p. 207–226, 2012. Available at: <https://doi.org/10.1615/AtomizSpr.2012005061>.

SÁNCHEZ, P. S. *Modeling the dispersion and evaporation of sprays in aeronautical combustion chambers*. Phd Thesis — Institut National Polytechnique de Toulouse - INPT, 2012. Available at: <https://tel.archives-ouvertes.fr/tel-00452501>.

SANJOSÉ, M. *Evaluation de la méthode Euler-Euler pour la simulation aux grandes échelles des chambres à carburant liquide*. Phd Thesis — Institut National Polytechnique de Toulouse - INPT, 2009. Available at: <https://tel.archives-ouvertes.fr/tel-00451199/>.

SARATHY, S. M.; OSSWALD, P.; HANSEN, N.; KOHSE-HÖINGHAUS, K. Alcohol combustion chemistry. *Progress in Energy and Combustion Science*, v. 44, n. Supplement C, p. 40 – 102, 2014. Available at: <https://doi.org/10.1016/j.pecs.2014.04.003>.

SAZHIN, S.; ABDELGHAFFAR, W.; SAZHINA, E.; HEIKAL, M. Models for droplet transient heating: Effects on droplet evaporation, ignition, and break-up. *International Journal of Thermal Sciences*, v. 44, n. 7, p. 610 – 622, 2005. Available at: <https://doi.org/10.1016/j.ijthermalsci.2005.02.004>.

SAZHIN, S.; ELWARDANY, A.; KRUTITSKII, P.; CASTANET, G.; LEMOINE, F.; SAZHINA, E.; HEIKAL, M. A simplified model for bi-component droplet heating and evaporation. *International Journal of Heat and Mass Transfer*, v. 53, n. 21, p. 4495 – 4505, 2010. Available at: <https://doi.org/10.1016/j.ijheatmasstransfer.2010.06.044>.

SAZHIN, S. S. Advanced models of fuel droplet heating and evaporation. *Progress in Energy and Combustion Science*, v. 32, n. 2, p. 162 – 214, 2006. Available at: <http://dx.doi.org/10.1016/j.pecs.2005.11.001>.

SAZHIN, S. S. Modelling of fuel droplet heating and evaporation: Recent results and unsolved problems. *Fuel*, v. 196, n. Supplement C, p. 69 – 101, 2017. Available at: <http://dx.doi.org/10.1016/j.fuel.2017.01.048>.

SCHERER, P. O. J. Interpolation. In: _____. *Computational Physics: Simulation of Classical and Quantum Systems*. Heidelberg: Springer International Publishing, 2013. p. 15–35. Available at: <https://doi.org/10.1007/978-3-319-00401-3_2>.

SCHLICHTING, H.; GERSTEN, K. *Boundary-Layer Theory*. 9. ed. Springer-Verlag Berlin Heidelberg, 2017. Available at: <http://dx.doi.org/10.1007/978-3-662-52919-5>.

SCHLOTTKE, J.; WEIGAND, B. Direct numerical simulation of evaporating droplets. *Journal of Computational Physics*, v. 227, n. 10, p. 5215 – 5237, 2008. Available at: <https://doi.org/10.1016/j.jcp.2008.01.042>.

SCHWARZKOPF, J. D.; SOMMERFELD, M.; CROWE, C. T.; TSUJI, Y. *Multiphase Flows with Droplets and Particles*. 2. ed. [S.l.]: CRC press, 2011.

SHIROLKAR, J.; COIMBRA, C.; MCQUAY, M. Q. Fundamental aspects of modeling turbulent particle dispersion in dilute flows. *Progress in Energy and Combustion Science*, v. 22, n. 4, p. 363 – 399, 1996. Available at: <https://doi.org/10.1016/S0360-1285(96)00006-8>.

SILVA, R. P. *Desenvolvimento, implementação e validação de uma estrutura de dados para transporte euleriano-lagrangeano e aplicações em escoamentos bifásicos usando refinamento adaptativo de malha*. Phd Thesis — Universidade Federal de Uberlândia, 2016.

SIRIGNANO, W. A. Fluid dynamics of sprays - 1992 Freeman scholar lecture. *Journal of Fluids Engineering*, ASME, v. 115, n. 3, p. 345 – 378, 1983. Available at: <http://dx.doi.org/10.1115/1.2910148>.

SIRIGNANO, W. A. *Fluid Dynamics and Transport of Droplets and Sprays*. 2. ed. Cambridge University Press, 2010. Available at: <http://dx.doi.org/10.1017/CBO9780511806728>.

SIRIGNANO, W. A.; LAW, C. K. Transient heating and liquid-phase mass diffusion in fuel droplet vaporization. In: _____. *Evaporation-Combustion of Fuels*. ACS Publications, 1978. chap. 1, p. 3–26. Available at: <https://doi.org/10.1021/ba-1978-0166.ch001>.

SOM, S. *Introduction to Heat Transfer*. [S.l.]: PHI Learning, 2008.

SOMMERFELD, M. Numerical methods for dispersed multiphase flows. In: _____. *Particles in Flows*. Cham: Springer International Publishing, 2017. p. 327–396. Available at: <http://dx.doi.org/10.1007/978-3-319-60282-0_6>.

SOMMERFELD, M.; QIU, H.-H. Experimental studies of spray evaporation in turbulent flow. *International Journal of Heat and Fluid Flow*, v. 19, n. 1, p. 10 – 22, 1998. Available at: <http://dx.doi.org/10.1016/S0142-727X(97)10002-9>.

SPALDING, D. The combustion of liquid fuels. *Symposium (International) on Combustion*, v. 4, n. 1, p. 847 – 864, 1953. Fourth Symposium (International) on Combustion. Available at: <https://doi.org/10.1016/S0082-0784(53)80110-4>.

STEFAN, J. Über die verdampfung aus einem kreisförmig oder elliptisch begrenzten becken. *Wien Ber*, v. 83, p. 943–954, 1881.

STEPHAN, P.; KABELAC, S.; KIND, M.; MARTIN, H.; MEWES, D.; SCHABER, K. *VDI Heat Atlas*. 2. ed. Springer-Verlag Berlin Heidelberg, 2010. Available at: <http://dx.doi.org/10.1007/978-3-540-77877-6>.

TESKE, M. E.; THISTLE, H. W.; LONDERGAN, R. J. Considerations of time step and evolving droplet size in the simulation of fine droplet motion using AGDISP. In: ASABE. *Proc. of 2009 ASABE Annual International Meeting*. [S.l.], 2009.

TURNS, S. *An Introduction to Combustion: Concepts and Applications*. 2. ed. [S.l.]: McGraw-Hill, 2000.

VERON, F. Ocean spray. *Annual Review of Fluid Mechanics*, Annual Reviews, v. 47, n. 1, p. 507–538, 2015. Available at: <http://dx.doi.org/10.1146/annurev-fluid-010814-014651>.

VERWEY, C.; BIROUK, M. Experimental investigation of the effect of droplet size on the vaporization process in ambient turbulence. *Combustion and Flame*, v. 182, n. Supplement C, p. 288 – 297, 2017. Available at: <https://doi.org/10.1016/j.combustflame.2017.04.027>.

VERWEY, C.; BIROUK, M. Experimental investigation of the effect of natural convection on the evaporation characteristics of small fuel droplets at moderately elevated temperature and pressure. *International Journal of Heat and Mass Transfer*, v. 118, p. 1046 – 1055, 2018. Available at: <https://doi.org/10.1016/j.ijheatmasstransfer.2017.11.038>.

VOLKOV, R.; KUZNETSOV, G.; STRIZHAK, P. Influence of droplet concentration on evaporation in a high-temperature gas. *International Journal of Heat and Mass Transfer*, v. 96, p. 20 – 28, 2016. Available at: <https://doi.org/10.1016/j.ijheatmasstransfer.2016.01.029>.

EL WAKIL, M.; UYEHARA, O.; MYERS, P. *A theoretical investigation of the heating-up period of injected fuel droplets vaporizing in air*. [S.l.], 1954.

WANG, H.; LUO, K.; FAN, J. Effects of turbulent intensity and droplet diameter on spray combustion using direct numerical simulation. *Fuel*, v. 121, p. 311 – 318, 2014. Available at: <https://doi.org/10.1016/j.fuel.2013.12.061>.

WESTBROOK, C. K. Biofuels combustion. *Annual Review of Physical Chemistry*, v. 64, n. 1, p. 201–219, 2013. Available at: <https://doi.org/10.1146/annurev-physchem-040412-110009>.

WILLIAMS, F. A. *Combustion Theory: The fundamental theory of chemically reacting flow systems*. 2. ed. [S.l.]: Benjamin-Cummings Publishing Company, 1985. (Combustion Science & Engineering).

WONG, S.-C.; LIN, A.-C. Internal temperature distributions of droplets vaporizing in high-temperature convective flows. *Journal of Fluid Mechanics*, Cambridge University Press, v. 237, p. 671–687, 1992. Available at: <https://doi.org/10.1017/S0022112092003574>.

XIA, J.; LUO, K. Direct numerical simulation of diluted combustion by evaporating droplets. *Proceedings of the Combustion Institute*, v. 32, n. 2, p. 2267 – 2274, 2009. Available at: <https://doi.org/10.1016/j.proci.2008.05.047>.

XIA, J.; ZHAO, H.; MEGARITIS, A.; LUO, K. H.; CAIRNS, A.; GANIPPA, L. C. Inert-droplet and combustion effects on turbulence in a diluted diffusion flame. *Combustion and Flame*, v. 160, n. 2, p. 366 – 383, 2013. Available at: <https://doi.org/10.1016/j.combustflame.2012.10.007>.

YANG, J.-R.; WONG, S.-C. On the discrepancies between theoretical and experimental results for microgravity droplet evaporation. *International Journal of Heat and Mass Transfer*, v. 44, n. 23, p. 4433 – 4443, 2001. Available at: <https://doi.org/10.1016/S0017-9310(01)00091-6>.

YANG, J.-R.; WONG, S.-C. An experimental and theoretical study of the effects of heat conduction through the support fiber on the evaporation of a droplet in a weakly convective flow. *International Journal of Heat and Mass Transfer*, v. 45, n. 23, p. 4589 – 4598, 2002. Available at: <https://doi.org/10.1016/S0017-9310(02)00164-3>.

YI, P.; JIA, M.; LONG, W.; QIAO, L.; YANG, T.; FENG, L. Evaporation of pure and blended droplets of diesel and alcohols (C2–C9) under diesel engine conditions. *Numerical Heat Transfer, Part A: Applications*, Taylor & Francis, v. 71, n. 3, p. 311–326, 2017. Available at: <https://doi.org/10.1080/10407782.2016.1264749>.

YUEN, M. C.; CHEN, L. W. On drag of evaporating liquid droplets. *Combustion Science and Technology*, Taylor & Francis, v. 14, n. 4-6, p. 147–154, 1976. Available at: <https://doi.org/10.1080/00102207608547524>.

YUGE, T. Experiments on heat transfer from spheres including combined natural and forced convection. *Journal of Heat Transfer*, ASME, v. 82, n. 3, p. 214–220, 1960. Available at: <https://doi.org/10.1115/1.3679912>.

APPENDIX A

Cantera: properties calculator

- props_calculator.h

```
#ifndef props_calculator_H
#define props_calculator_H

struct props_calculator;
typedef struct props_calculator props_calculator_t;

typedef struct props {
        double rho;
        double cp;
        double mu;
        double k;
}props_t;

/*! Creates a property calculator. */
props_calculator_t* props_calculator_create(char* cti_file, char* cant_mech);

/*! Destroys a property calculator. */
void props_calculator_destroy(props_calculator_t* pc);

/*! Returns the number of species in the cti file. */
int props_calculator_get_num_species(props_calculator_t* pc);

/*! Retrieves all the thermodynamic and transport properties. */
void props_calculator_get_mix (props_calculator_t* pc, double* comp, double
    p_amb, double Tm, props_t* return_props, double* diff_coeffs);

/*! Returns the molecular weight. */
double props_calculator_get_mol_weight (props_calculator_t* pc, double* comp);

#endif
```

- props_calculator.cpp

```cpp
#include <memory>
#include <string>
#include "cantera/thermo.h"
#include "cantera/transport.h"

extern "C"{
#include "props_calculator.h"
}


struct props_calculator {
    std::unique_ptr<Cantera::ThermoPhase> thermo;
    std::unique_ptr<Cantera::Transport> transp;
};

props_calculator_t* props_calculator_create(char* cti_file, char* cant_mech)
{
    auto* pc = new props_calculator;

    std::string full_cti_file = std::string("../input/mechanisms/")+cti_file;
    pc->thermo.reset(Cantera::newPhase(full_cti_file.c_str(),cant_mech));
    pc->transp.reset(Cantera::newDefaultTransportMgr(pc->thermo.get()));
    return pc;
}

void props_calculator_destroy(props_calculator_t* pc)
{
    delete pc;
}

int props_calculator_get_num_species(props_calculator_t* pc)
{
    return pc->thermo->nSpecies();
}
```

```
35
36 void props_calculator_get_mix (props_calculator_t* pc, double* comp, double
       p_amb, double Tm, props_t* return_props, double* diff_coeffs)
37 {
38     pc->thermo->setPressure(p_amb);
39     pc->thermo->setState_TPX(Tm, p_amb, comp);
40
41     return_props->rho = pc->thermo->density();
42     return_props->cp = pc->thermo->cp_mass();
43     return_props->mu = pc->transp->viscosity();
44     return_props->k = pc->transp->thermalConductivity();
45
46     if(diff_coeffs) {
47         pc->transp->getMixDiffCoeffs(diff_coeffs);
48     }
49 }
50
51 double props_calculator_get_mol_weight (props_calculator_t* pc, double* comp)
52 {
53     pc->thermo->setMoleFractions(comp);
54     return pc->thermo->meanMolecularWeight();
55 }
```